ATLAS+CMS DARK MATTER FORUM RECOMMENDATIONS

Author/contributor list to be added as document is finalized.

Contact editors: lhc-dmf-admin@cern.ch

May 25, 2015

Contents

1

Introduction

Many theories of physics beyond the Standard Model predict the existence of a stable, neutral, weakly-interacting and massive particle that is a putative dark matter candidate. In the following, we refer to such matter as dark matter, even though the observation of such matter at a collider could only establish that it is neutral, weakly-interactive, massive and stable on the distance-scales of 10's of meters. Dark matter has not yet been observed in particle physics experiments, and there is not yet any evidence for non-gravitational interactions between dark matter and Standard Model particles. If such interactions exist, dark matter particles could be produced at the LHC. Dark matter particles of themselves do not produce signals in the LHC detectors, so simple pair-production of dark matter particles, for example, would not be visible. However, there are different mechanisms by which a visible SM particle $X(=g, q, \gamma, Z, W,$ or $h)$ could be produced in association with dark matter. Such reactions, which are observed as particles or jets recoiling against an invisible state, are called "mono-X" or $\not{E}_T$+X reactions.

Early Run 1 searches for $\not{E}_T$+X signatures at ATLAS and CMS employed a basis of operators in effective field theories (EFTs) [GIR$^+$10] to calculate the possible signals. These particular EFTs assume that production of dark matter takes place through a contact interaction involving a quark-antiquark pair or two gluons and two dark matter particles. In this case, the missing energy distribution of the signal is determined by the mass of the dark matter particles and the Lorentz structure of the interaction. Only the overall production rate is a free parameter. Both experiments studied a variety of EFTs with different spin structures. Provided that the contact interaction approximation holds, these EFTs also provide a straightforward way to compare the results from different collider searches with non-collider searches for dark matter.

However, it has become clear [BFH10, Kop11, FHKT11, FHKT12, BDSMR14] that a contact interaction is often not the correct description for the signals to which the LHC is sensitive. Limits from the LHC on particles that are QCD singlets and do not decay to hard leptons are relatively weak. Such particles can mediate reactions that produce dark matter particles. If the mass of the mediator is

light, the kinematics of the pair-production reaction can differ substantially from that due to a contact interaction, modifying limits and possibly requiring new search strategies. While the EFT integrates out the degrees of freedom of the (heavy) intermediate particle, "simplified models" [AST09, A⁺12] with directly-accessible mediators describe this richer phenomenology. Appropriate simplified models can be used both to interpret mono-X searches and to guide the design of complementary searches for additional signatures.

Many proposals for such models began to emerge (see, for example Refs. [AJW12, AHW13, DNRT13, BDM14, BB13a, BB14, AWZ14a, A⁺14a, MMA⁺14, HKSW15, BFG15, HR15]). At the end of 2014, ATLAS and CMS organized a forum, the ATLAS-CMS Dark Matter Forum, to form a consensus with the participation of experts on theories of dark matter. This is the final report of that forum.

One of the guiding principles of this report is to channel the efforts of the ATLAS and CMS Collaboration towards a minimal set of dark matter models that should influence the design of the early Run-2 searches. At the same time, a thorough survey of realistic collider signals of dark matter is a crucial input to the overall design of the search program.

The goal of this report is such a survey, though confined within some broad assumptions and focused on benchmarks for kinematically-distinct signals which are most urgently needed. As far as time and resources have allowed, the assumptions have been carefully motivated by theoretical consensus and comparisons of simulations. But to achieve a true consensus with only a few months before Run 2 would begin, it was important to narrow the scope and timescale to the following:

1. The forum should propose a prioritized, small set of benchmark simplified models that should be agreed upon by both collaborations for Run-2 searches. The values for the scan on the parameters of the models for which experimental results are provided should be specified, to facilitate theory reinterpretation beyond the necessary model-independent limits that should be provided by all LHC Dark Matter searches.

2. The forum should standardize the event generator implementation of the simplified models and harmonize other common technical details as far as practical. It would be desirable to have a common choice of LO/NLO, ME-parton shower matching and merging, factorization and renormalization scales for each of the simplified models. This will also lead to a single set of theory uncertainties, which will be easier to deal with when comparing results from the two collaborations.

3. The forum could also discuss the conditions under which the EFT interpretation may still be desirable.

162 4. The forum should prepare a report summarizing these items,
163   suitable both as a reference for the internal ATLAS and CMS
164   audiences and as an explanation for theory and non-collider
165   readers. This report represents the views of the participants of
166   the forum.

1.1   Grounding Assumptions

We assume that interactions exist between Standard Model hadrons
and whatever it is that constitutes cosmological dark matter. If
this is not the case, then proton collisions will not produce dark
matter particles, and dark matter will not scatter off nuclei in direct
detection experiments.

The Dark Matter itself is assumed to be a single particle, a Dirac
fermion WIMP, stable on collider timescales and non-interacting
with the detector. The former assumption is reductionistic. The rich
particle content of the Standard Model is circumstantial evidence
that the dark matter sector, which constitutes five times as much of
the mass of the universe, may be more complex than a single parti-
cle or a single interaction. But, as was often the case in the discover-
ies of the SM, here only one mediator and one search channel might
play a dominant role in the opening stages of an LHC discovery.
The latter assumption focuses our work on early LHC searches,
where small kinematic differences between models will not mat-
ter in a discovery scenario, and with the imminent re-start of the
LHC our report relies heavily on a large body of existing theoretical
work which made this assumption. Different types of dark mat-
ter particles will typically give similar results. The choice of Dirac
fermions permits some processes forbidden for Majorana fermions.
Aside from this, the cases of Dirac or Majorana fermions or scalars
produces only minor changes in the kinematic distributions of the
visible particle, especially when considering cut-and-count analy-
sis. Thus the choice of Dirac fermion dark matter is deemed suffi-
cient for the benchmarks aiding the design of the upcoming Run-2
searches. Nevertheless, a more complete set of models will certainly
be required upon a discovery; see e.g. [CHLR13, HHR14, CHH15]
for some studies of observables that may distinguish amongst these
models.

The weakness of the dark matter–visible matter interactions is
explained by assuming a mediating force or particle that indirectly
connects the two. In the EFT approach, the mass scale of the me-
diator is assumed to be large compared to the typical momentum
involved in the production of dark matter. Simplified models al-
low the exploration of scenarios where the mediating scale is not
so large. One strength of collider experiments lies in the ability to
study the mediator, not the DM itself. A discovery of a $\not{E}_T$ signature
at the LHC would not uniquely imply discovery of dark matter,
while at the same time discovery of an anomalous and annually-
modulated signal in a direct-detection experiment would leave

unanswered many questions about the nature of the interaction. The these two approaches, and other types of non-collider searches, provide complementary ways to approach the problem, and it is in this spirit that our focus is on the mediator. We systematically explore the basic possibilities for tree-level exchange: s-channel or t-channel interactions, and mediators of various possible spins. All models are assumed to produce pairs of dark matter particles. Though more varied and interesting possibilities are added to the literature almost daily, these basic building blocks account for much of the physics studied at hadron colliders in the past three decades.

We also assume that Minimal Flavor Violation (MFV) [CG87, HR90, BGG+01, DGIS02] applies to the recommended models. By this, we mean that the flavor structure of the couplings between dark matter and ordinary particles follows the same structure as the Standard Model. This choice is simple, since no additional theory of flavor is required, beyond what is already present in the SM, and it provides a mechanism to ensure that the models do not violate flavor constraints. As a consequence, spin-0 resonances exchanged in the s-channel must have couplings to fermions proportional to the SM Higgs couplings. Flavor-safe models can still be constructed beyond the MFV assumption, for example [ABG14], and deserve further study.

In the parameter scan for the recommended models, we make the assumption of a minimal decay width for the particles mediating the interaction between SM and DM. By this, we mean that only decays strictly necessary for the self-consistency of the model (e.g. to DM and to quarks) are accounted for in the definition of the mediator width. We forbid any further decays to other invisible particles of the Dark Sector that may increase the width. Studies within the Forum show that, for cut and count analyses, the kinematic distributions of many models and therefore the sensitivity of the search do not depend significantly on the mediator width, as long as the width remains smaller than the mass of the particle.

The particle content of the models chosen as benchmarks is limited to one single kind of DM whose self-interactions are not relevant for LHC phenomenology, and to one type of SM/DM interaction at a time. These assumptions only add a limited number of new particles to the SM. These simplified models, independently sought by different experimental analyses, can be used as starting points to build more complete theories. Even though this factorized picture does not always lead to full theories and leaves out details that are necessary for the self-consistency of single models (e.g. the mass generation for mediator particles), it is a starting point to prepare a set of distinct but yet complementary collider searches for Dark Matter, as it leads to benchmarks that are easily comparable across channels.

Contact interaction operators (EFTs) are also part of this report, to be considered whenever neither a simplified model completion nor other simplified models yielding similar kinematic distributions

are available. This is the case for dimension 5-7 operators with direct Dark Matter-electroweak boson couplings. Model-independent results should be emphasized in the signal regions that are unique to these models, and results should be considered with the necessary caution due to EFT validity issues covered in the last chapter in this report. Results from these models may nevertheless help validate the contact interaction limit of new simplified models developed to complete these specific operators.

The first chapter of the report is dedicated to simplified models with radiation of a hard object either from the initial state or from the mediator. These models produce primarily monojet signatures, but are recommended for all $\not{E}_T$+X searches. Details of the implementation of these models in Monte Carlo generators are provided in Appendix A. Chapter 3 contains the benchmark model recommendations and choices for final states specifically containing an electroweak boson ($W/Z/\gamma/H$). In this case, both simplified models leading to mono-boson signatures and contact interaction operators wherever simplified models are not available are considered. The final chapter is devoted to the treatment of the validity of benchmark models from contact interaction operators. The technical implementation and further models that can be studied beyond early searches are in appendix B. Appendix C contains the necessary elements that should be included in the results of experimental searches to allow for further reinterpretation.

2

Recommended models for all $\not{E}_T$ +X analyses

In this Chapter we review recommendations for final states of $\not{E}_T$ recoiling against a particle extracted from initial state radiation, be it a gluon or an electroweak boson ($W/Z/\gamma/H$). Whist the recommendations are general, the discussions in this Chapter are made generally based on the monojet final state. Details on final states with EW boson radiation and with heavy flavor quarks from diagrams arising within these models are also discussed in this Chapter. These studies and studies in subsequent sections are based on simulation of the models with the generators implementation recommended in each section and provided in a companion CERN SVN repository. Further details on the implementation of these models can be found in Appendix A.

2.1 Vector and axial vector mediator, s-channel exchange

A simple extension of the Standard Model (SM) is an additional $U(1)$ gauge symmetry, where a dark matter (DM) candidate particle has charges only under this new group. Assuming that some SM particles are also charged under this group, then a new gauge boson can mediate interactions between the SM and DM.

We consider the case of a DM particle χ of mass $m_{\rm DM}$ that is a Dirac fermion and where the production proceeds via the exchange of a spin-1 mediator of mass $M_{\rm med}$ in the s-channel, illustrated in Fig. 2.1.
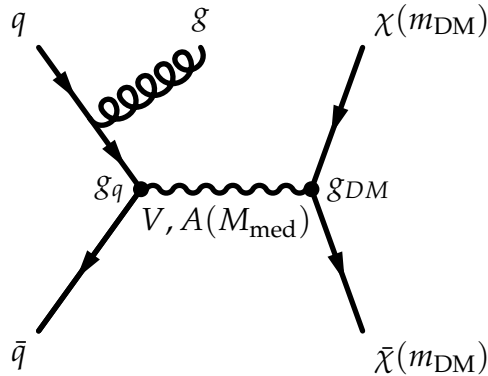
Figure 2.1: Representative Feynman diagram showing the pair production of dark matter particles in association with a parton from the initial state via a vector or axial-vector mediator. The cross section and kinematics depend upon the mediator and dark matter masses, and the mediator couplings to dark matter and quarks respectively: ($M_{\rm med}$, $m_{\rm DM}$, $g_{\rm DM}$, $g_{\rm q}$).

We consider two models with vector and axial-vector couplings between the spin-1 mediator and SM and DM fields, with the corresponding interaction Lagrangians:

$$\mathcal{L}_{\text{vector}} = g_{\text{q}} \sum_{q=u,d,s,c,b,t} Z'_\mu \bar{q} \gamma^\mu q + g_{\text{DM}} Z'_\mu \bar{\chi} \gamma^\mu \chi \qquad (2.1)$$

$$\mathcal{L}_{\text{axial-vector}} = g_{\text{q}} \sum_{q=u,d,s,c,b,t} Z'_\mu \bar{q} \gamma^\mu \gamma^5 q + g_{\text{DM}} Z'_\mu \bar{\chi} \gamma^\mu \gamma^5 \chi. \qquad (2.2)$$

The coupling g_{q} is assumed to be universal to all quarks. It is also possible to consider other models in which mixed vector and axial-vector couplings are considered, for instance the couplings to the quarks are axial-vector whereas those to DM are vector. We recommend the models with pure vector couplings or pure axial-vector couplings. As mentioned in the Introduction, when no additional visible or invisible decays contribute to the width of the mediator, the minimal width is fixed by the choices of couplings g_{q} and g_{DM}. The effect of larger widths is discussed on page 40. For the vector and axial-vector models, the minimal width is

$$\Gamma^{V/A}_{\text{min}} = \Gamma^{V/A}_{\bar{\chi}\chi} + \sum_q \Gamma^{V/A}_{\bar{q}q}. \qquad (2.3)$$

The leading order expressions for the partial widths are:

$$\Gamma^V_{\bar{\chi}\chi} = \frac{g^2_{\text{DM}} M_{\text{med}}}{12\pi} \left(1 + \frac{2m^2_{\text{DM}}}{M^2_{\text{med}}}\right) \beta_{DM} \theta(M_{\text{med}} - 2m_{\text{DM}}) \qquad (2.4)$$

$$\Gamma^V_{\bar{q}q} = \frac{3g^2_{\text{q}} M_{\text{med}}}{12\pi} \left(1 + \frac{2m^2_q}{M^2_{\text{med}}}\right) \beta_q \theta(M_{\text{med}} - 2m_q) \qquad (2.5)$$

$$\Gamma^A_{\bar{\chi}\chi} = \frac{g^2_{\text{DM}} M_{\text{med}}}{12\pi} \beta^{3/2}_{DM} \theta(M_{\text{med}} - 2m_{\text{DM}}) \qquad (2.6)$$

$$\Gamma^A_{\bar{q}q} = \frac{3g^2_{\text{q}} M_{\text{med}}}{12\pi} \beta^{3/2}_q \theta(M_{\text{med}} - 2m_q), \qquad (2.7)$$

$\theta(x)$ denotes the Heaviside step function, and $\beta_f = \sqrt{1 - \frac{4m^2_f}{M^2_{\text{med}}}}$ is the velocity of the fermion f in the mediator rest frame. Note the color factor 3 in the quark terms. Figure 2.2 shows the minimal width as a function of mediator mass for both vector and axial-vector mediators assuming $g_{\text{q}} = g_{\text{DM}} = 1$. With this choice of the couplings, the dominant contribution to the minimal width comes from the quarks, due to the combined quark number and color factor enhancement.

Therefore, the minimal set of parameters under consideration for these two models is

$$\{m_{\text{DM}}, M_{\text{med}}, g_{\text{q}}, g_{\text{DM}}\}. \qquad (2.8)$$

See [BDMM15] for a thorough discussion.

2.1.1 Parameter scan

In order to determine an optimal choice of the parameter grid for the simulation of early Run-2 benchmark models, dependencies of

To do **Studies have been performed to see if the case of a mixed coupling can be simply extracted from the other models by some reweighting procedure to take account of the difference in cross section. This would assume that the difference between the pure and mixed couplings case does not affect the kinematics of the event. Note, though, that in the mediator rest frame, the angular distribution of the DM relative to the mediator direction of motion has the form:** $1 + z^2 + 2 * C * z$ **(**$z = \cos\theta$**), with the second term only present in the mixed case. This may lead to acceptance differences. (??)**
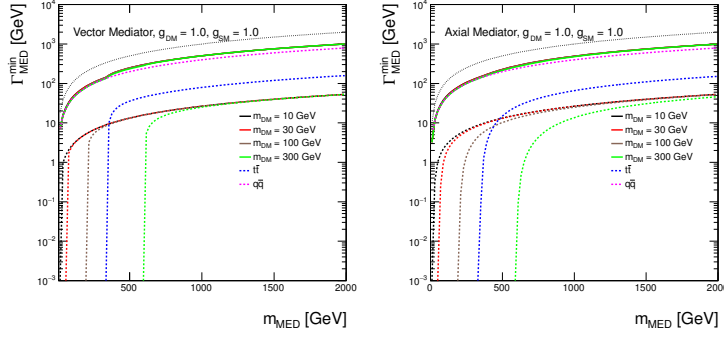
Figure 2.2: Minimal width as a function of mediator mass for vector and axial-vector mediator assuming couplings of 1. The total width is shown as solid lines for Dark Matter masses of 10 GeV, 30 GeV, 100 GeV and 300 GeV in black, red, brown and green, respectively. The individual contributions from Dark Matter are indicated by dotted lines with the same colors. The contribution from all quarks but top is shown as magenta dotted line and the contribution from top quarks only is illustrated by the dotted blue line. The dotted black line shows the extreme case $\Gamma_{\min} = M_{\mathrm{med}}$.

the kinematic quantities and cross sections on the model parameters have been studied. The following paragraphs list the main observations from the scans over the parameters that support the final proposal for the benchmark signal grid.

Scan over the couplings   Figure 2.3 In order to study the dependence on the coupling strength, samples were generated where a pair of m_{DM} =10 GeV Dark Matter particles are produced on-shell from the mediator of M_{med} =1 TeV. No differences in the shape of the $\not{E}_T$ distribution are observed for the different choices of the coupling strength. This is a generator-level prediction with no kinematic selections or detector simulation. Coupling values in the scan range 0.1–1.45, holding $g_{\mathrm{q}} = g_{\mathrm{DM}}$, correspond to a rough estimate of the lower sensitivity of mono-jet analyses and a maximum coupling value such that $\Gamma_{\min} < M_{\mathrm{med}}$. Based on similar findings for different choices of M_{med} and m_{DM}, we conclude that the shapes of kinematic distributions are not altered by coupling variations, either for the on-shell Dark Matter production where $M_{\mathrm{med}} > 2m_{\mathrm{DM}}$, or for the off-shell Dark Matter production where $M_{\mathrm{med}} < 2m_{\mathrm{DM}}$. Only the production cross sections change. Differences in kinematic distributions are expected only close to the transition region where both on-shell and off-shell decays occur.

Figure 2.3: Scan over couplings. The $\not{E}_T$ distribution is compared for the vector mediator models using the parameters as indicated. Ratios of the normalized distributions with respect to the first one are shown. A_{300} and A_{500} in the table denote the acceptance of the $\not{E}_T > 300$ GeV and $\not{E}_T > 500$ GeV cut, respectively.

One situation requiring a careful consideration is the case of extremely heavy and narrow mediators, which can arise for small coupling strengths. Upon close examination, it was determined that this case is not peculiar. However, the complete story is a cautionary tale about understanding the details of the generator tools.

Figure 2.4 suggests a change in the shape of the $\not{E}_T$ distribution for a M_{med} =5 TeV mediator once $\Gamma_{\min}/M_{\mathrm{med}}$ is of the order of a percent or lower. This, however, does not come from physics, but is a consequence of under-sampling phase space in the generator implementation, where a cutoff for the regions far away from the mediator mass is generally used. One must take care to correctly set the width of the Breit-Wigner used for the sampling. This is illustrated in Fig. 2.5 showing the invariant mass of the Dark Matter pair in the samples generated for a M_{med} =7 TeV mediator with different coupling strengths. In all cases, it is expected to observe a peak around the mediator mass with a tail extending to $m_{\bar{\chi}\chi} \to 0$, significantly enhanced by parton distribution functions at low Bjorken x. For coupling strength 1 and 3, the massive enhancement at $m_{\bar{\chi}\chi} \to 0$ implies that resonant production at $m_{\bar{\chi}\chi} = 7$ TeV is statistically suppressed such that barely any events are generated there. However, for narrower mediators with couplings below 1, the peak around 7 TeV is clearly visible in the generated sample and the dominant tail at $m_{\bar{\chi}\chi} \to 0$ is artificially cut off, leading to unphysical cross section predictions and kinematic shapes. This explains why the sample with the narrowest mediator in Fig. 2.4 is heavily suppressed in terms of production cross section and also gives different $\not{E}_T$ shape. In general, for such extreme parameter choices the EFT model should give the correct answer.
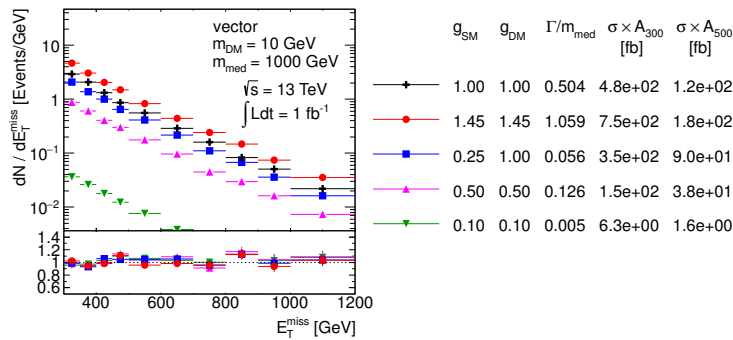

Figure 2.4: Scan over couplings. The $\not{E}_T$ distribution is compared for the vector mediator models using the parameters as indicated. Ratios of the normalized distributions with respect to the first one are shown. A_{300} and A_{500} in the table denote the acceptance of the $\not{E}_T > 300$ GeV and $\not{E}_T > 500$ GeV cut, respectively.
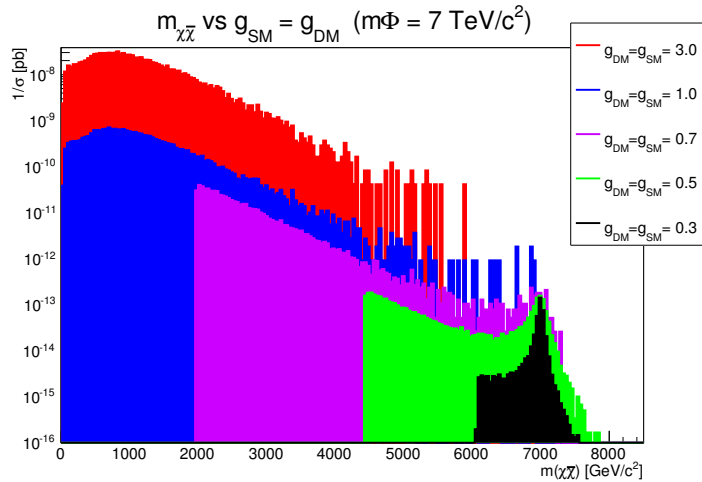
Figure 2.5: Invariant mass of the Dark Matter pair in the samples with $M_{\mathrm{med}} = 7$ TeV and different coupling strengths.

383   Since kinematic distributions are robust to changes in the specific
384 values of coupling, the choice of $g_q = g_{DM}$ is reasonable to reduce
385 the parameter space to be scanned. There are no complications
386 associated with small couplings, but, also, the early part of Run 2
387 will not be sensitive to them. The range of couplings we recom-
388 mend limit the calculated width of the mediator to be near or below
389 M_{med}.

390   For direct mediator searches, asymmetric couplings ($g_q \neq g_{DM}$)
391 might also be considered. A scan in g_{DM} vs g_q can then be per-
392 formed for a fixed mediator mass. Such searches, such as those for
393 dijet resonances, may restrict g_q to a greater degree than g_{DM}.

394 *Scan over the Dark Matter mass*   For a fixed mediator mass M_{med}
395 and couplings, both the cross section and the kinematic distribu-
396 tions remain similar for different Dark Matter masses as long as
397 $M_{med} > 2m_{DM}$. This simply reflects the fact that most mediators
398 are produced on-shell, and the details of the invisible decay are
399 unimportant. This is illustrated in Fig. 2.6 for an example of M_{med}
400 =1 TeV 10 GeV $< m_{DM} <$ 300 GeV. It is observed that the cross
401 section decreases as the m_{DM} approaches $M_{med}/2$. Once the Dark
402 Matter pair is produced off-shell, the cross section of the simplified
403 model is suppressed and the $\not{E}_T$ spectrum hardens, as demon-
404 strated with the choice of m_{DM} =1 TeV in the same plot. Figure 2.7
405 reveals the $\not{E}_T$ spectrum hardens further with increasing m_{DM}, ac-
406 companied by the gradual decrease of the cross section. From these
407 observations one can conclude:

408   • A coarse binning along m_{DM} is sufficient at $M_{med} \gg 2m_{DM}$.

409   • Finer binning is needed in order to capture the changes in the
410   cross section and kinematic quantities close to the production
411   threshold on both sides around $M_{med} = 2m_{DM}$.

412   • Due to the significant cross section suppression of the off-shell
413   Dark Matter pair production, it is not necessary to populate the
414   parameter space $M_{med} \ll 2m_{DM}$ since imminent LHC searches
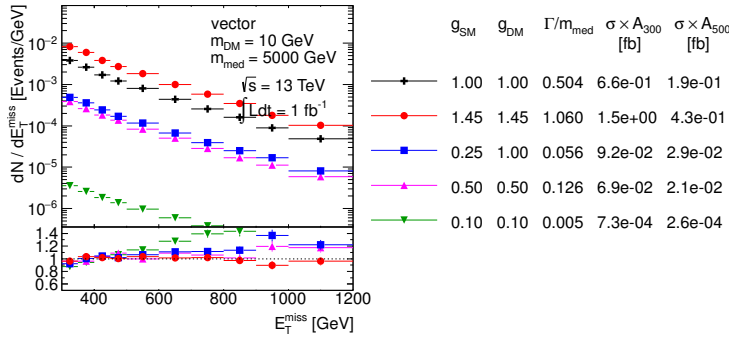415   are not expected to be sensitive to these signals.
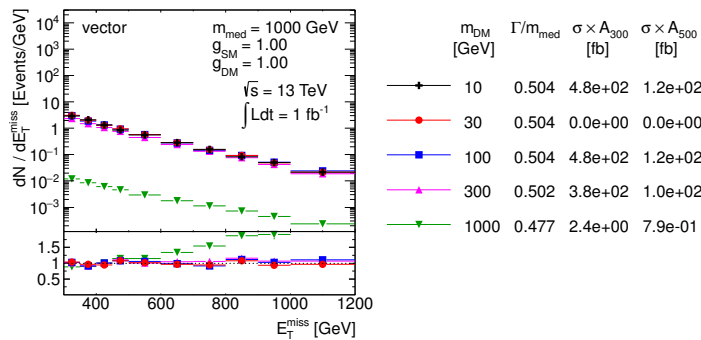
Figure 2.6: Scan over Dark Matter mass. The $\not{E}_T$ distribution is compared for the vector mediator models using the parameters as indicated. Ratios of the normalized distributions with respect to the first one are shown. A_{300} and A_{500} in the table denote the acceptance of the $\not{E}_T > 300$ GeV and $\not{E}_T > 500$ GeV cut, respectively.
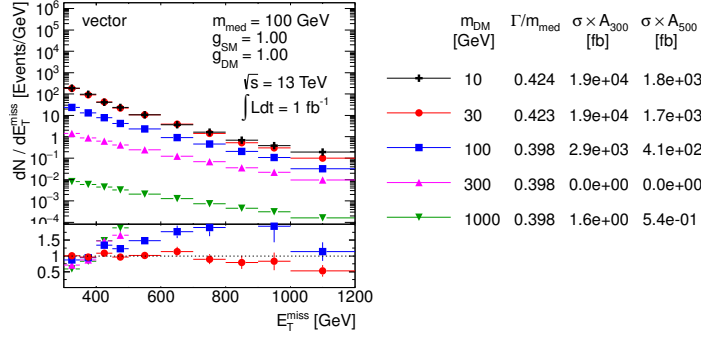
Figure 2.7: Scan over Dark Matter mass. The $\slashed{E}_T$ distribution is compared for the vector mediator models using the parameters as indicated. Ratios of the normalized distributions with respect to the first one are shown. A_{300} and A_{500} in the table denote the acceptance of the $\slashed{E}_T > 300$ GeV and $\slashed{E}_T > 500$ GeV cut, respectively.

Scan over the mediator mass   Changing the mediator mass for fixed Dark Matter mass and couplings leads to significant differences in cross section and shapes of the kinematic variables for $M_{\mathrm{med}} > 2m_{\mathrm{DM}}$ as shown in Fig. 2.8. As expected, higher mediator masses lead to harder $\slashed{E}_T$ spectra. On the other hand, the $\slashed{E}_T$ shapes are similar in the off-shell Dark Matter production regime. This is illustrated in Fig. 2.9. Therefore, a coarse binning in m_{DM} is sufficient at $M_{\mathrm{med}} \ll 2m_{\mathrm{DM}}$.
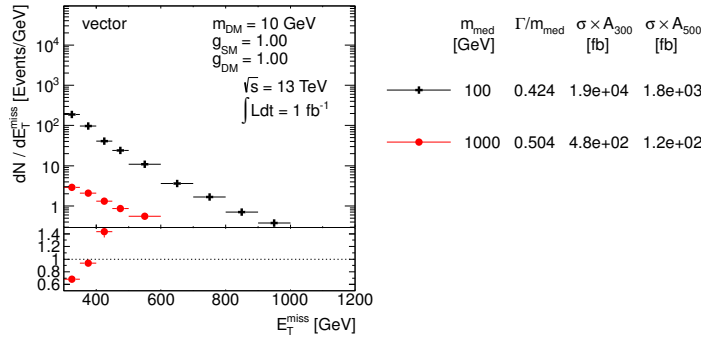
Figure 2.8: Scan over mediator mass. The $\slashed{E}_T$ distribution is compared for the vector mediator models using the parameters as indicated. Ratios of the normalized distributions with respect to the first one are shown. A_{300} and A_{500} in the table denote the acceptance of the $\slashed{E}_T > 300$ GeV and $\slashed{E}_T > 500$ GeV cut, respectively.
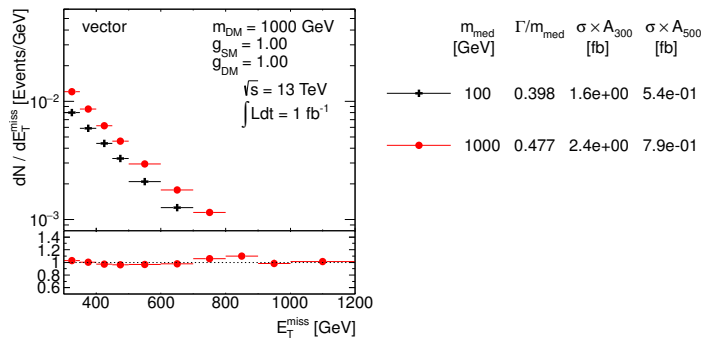
Figure 2.9: Scan over mediator mass. The $\slashed{E}_T$ distribution is compared for the vector mediator models using the parameters as indicated. Ratios of the normalized distributions with respect to the first one are shown. A_{300} and A_{500} in the table denote the acceptance of the $\slashed{E}_T > 300$ GeV and $\slashed{E}_T > 500$ GeV cut, respectively.

Proposed parameter grid   The final step in proposing a parameter grid is to evaluate the sensitivity of Run-2 LHC data with respect to rate and/or kinematics. Projected sensitivities for a 14 TeV mono-jet analysis are available from ATLAS [ATL14]. The expected upper limit at 95% confidence level on the product of cross section, acceptance and efficiency, $\sigma \times A \times \epsilon$, in the final Run-1 ATLAS

mono-jet analysis [A+15] is 51 fb and 7.2 fb for $\rlap{/}{E}_T > 300$ GeV and $\rlap{/}{E}_T > 500$ GeV, respectively. ATLAS estimates a factor of two increase in sensitivity with the 2015 data. Given that cross section for V+jets processes increases by roughly a factor 2 when going from $\sqrt{s} = 8$ TeV to 13 TeV, similar fiducial cross section limits can be expected with the first Run-2 data as from the final Run-1 analysis. The generator level cross section times the acceptance at $\rlap{/}{E}_T > 500$ GeV for the model with couplings $g_q = g_{DM} = 1$, a light Dark Matter particle of $m_{DM} = 10$ GeV and a $M_{med} = 1$ TeV vector mediator is at the order of 100 fb, i.e. the early Run-2 mono-jet analysis is going to be sensitive to heavier mediators than this. The value of $\sigma \times A$ at $\rlap{/}{E}_T > 500$ GeV for 5 TeV vector mediator is at the order of 0.1 fb, therefore this model probably lies beyond the reach of the LHC in the early Run 2.

Based on these arguments, the following M_{med} grid points are chosen, roughly equidistant in the logarithmic scale: 10 GeV, 20 GeV, 50 GeV, 100 GeV, 200 GeV, 300 GeV, 500 GeV, 1000 GeV and 2000 GeV. Given the fact that significant changes in cross section happen around the $M_{med} = 2m_{DM}$ threshold, the m_{DM} grid points are taken at approximately $M_{med}/2$, namely: 10 GeV, 50 GeV, 150 GeV, 500 GeV and 1000 GeV. Points on the on-shell diagonal are always chosen to be 5 GeV away from the threshold, to avoid numerical instabilities in the event generation. The detailed studies of the impact of the parameter changes on the cross section and kinematic distributions presented earlier in this section support removing some of the grid points and relying on interpolation. The optimized grids proposed for the vector and axial-vector mediators are given in Table. 2.1, containing 35 mass points each. One point at very high mediator mass (5 TeV) is added for each of the DM masses scanned, to aid the reinterpretation of results in terms of contact interaction operators (EFTs) as discussed in Section 4.4.

m_{DM} / GeV	M_{med} / GeV									
1	10	20	50	100	200	300	500	1000	2000	5000
10	10	15	50	100						5000
50	10		50	95	200	300				5000
150	10				200	295	500	1000		5000
500	10						500	995	2000	5000
1000	10							1000	1995	5000

Table 2.1: Simplified model benchmarks for $s-$channel simplified models (spin-1 mediators decaying to Dirac DM fermions in the V and A case, taking the minimum width for $g_q = g_{DM} = 1$)

The presentation of the results in the g_q–g_{DM} plane for fixed masses benefits from cross section scaling and is discussed in Section 2.5.

2.1.2 Additional considerations for $V + \rlap{/}{E}_T$ signatures

All models detailed in this Section are applicable to signatures states where a photon, a W boson, a Z boson or a Higgs boson are radiated instead of a gluon. The experimental signature is identified as $V + \rlap{/}{E}_T$.

Monojet searches are generally more sensitive with respect to final states including bosons, due to the much larger rates of signal events featuring quark or gluon radiation with respect to radiation of bosons [ZBW13], in combination with the low branching ratios if leptons from boson decays are required in the final state. The rates for the Higgs boson radiation is too low for these models to be considered a viable benchmark [CDM$^+$14]. However, the presence of photons, leptons from W and Z decays, and W or Z bosons decaying hadronically allow backgrounds to be rejected more effectively, making Z/gamma/W+$\not{E}_T$ searches still worth comparing with searches in the jet+$\not{E}_T$ final state.

In the case of a vector mediator exchanged in the s-channel, an example Feynman diagram for these processes can be constructed by taking Fig. 2.1 and replacing the gluon with γ, W or Z. The interest for searches with W bosons in the final state has been elevated by the increased cross section for certain choices of couplings for a spin-1 mediator [BT13]. Run-1 searches have considered three sample cases for the product of up and down quark couplings to the mediator, denoted as ξ:

$\xi = 0$: No couplings between mediator and either up or down quarks;

$\xi = 1$: Same coupling between mediator and each of the quark types;

$\xi = -1$: Coupling of opposite sign between mediator and each of the quark types.

The $\xi = -1$ case leads to a large increase in the cross-section of the process, and modifies the spectrum of missing transverse energy or transverse mass used for the searches. The sensitivity of the W+$\not{E}_T$ search for this benchmark in this case surpasses that of the jet+$\not{E}_T$ search. However, as shown in Ref. [BCD$^+$15], the cross-section increase is due to the production of longitudinally polarized W bosons, as a consequence of a violation of electroweak gauge symmetries. Unless further particles are introduced (in a fashion similar to the Higgs boson in the Standard Model), choosing a value of $\xi = -1$ for this simplified model will lead to a manifest violation of unitarity at LHC energies. The simplified model with a vector mediator exchanged in the s-channel model can still be considered as a benchmark for searches with a W boson if $\xi = 1$. We leave the study of further models with cross-section enhancements due to different couplings to up and down quarks for studies beyond the early LHC searches covered in this document. An example of such model is the case of both DM and SM Higgs charged under a new $U(1)'$, with a small mass mixing between the SM Z-boson and the new Z'-boson. This leads to different effective DM couplings to u_L and d_L, proportional to their coupling to the Z boson, detailed in Appendix B.

As in the case of the jet+$\not{E}_T$ models, the width does not have a significant impact on the kinematic distributions relevant for

those searches. An example of the particle-level analysis acceptance using the generator-level cuts from Ref. [Aad15] for the photon+$\not{E}_T$ analysis, but raising the photon p_T cut to 150 GeV is shown in Figure 2.2, comparing a width that is set to $\Gamma = M_{med}/3$ to the minimal width (the ratio between the two widths ranges from 1.05 to 1.5 with increasing mediator masses).

Acceptance ratio for $\Gamma = \Gamma_{\min}$ vs $\Gamma = M_{\mathrm{med}}/3$				
	$m_{\mathrm{DM}}/\mathrm{GeV}$			
$M_{\mathrm{med}}/\mathrm{GeV}$	10	50	200	400
50	0.96	0.99		0.95
100	0.97			
300	1.00	1.02		
600			0.96	
1000	1.01	1.02	1.03	
3000	1.02	1.03		1.01

Table 2.2: Analysis acceptance for the photon+$\not{E}_T$ analysis when varying the mediator width, in the case of a vector mediator exchanged in the $s-$channel

Examples of relevant kinematic distributions for selected benchmark points are shown in Fig. 2.10. leading-order cross-sections for the chosen benchmark points are shown in Appendix B.
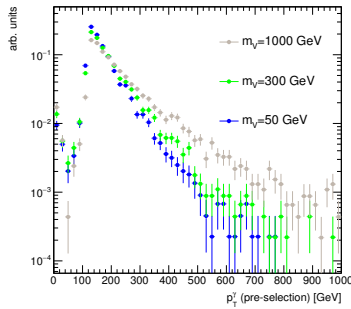
(a) Missing transverse momentum distribution for the photon+$\not{E}_T$ final state, for different mediator mass choices, for $m_{\mathrm{DM}} =$10 GeV.
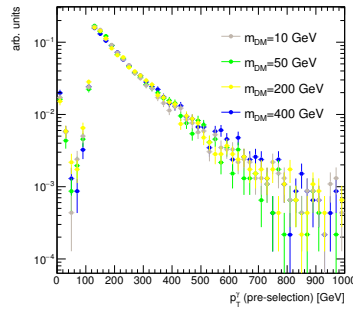
(b) Leading photon transverse momentum distribution for the photon+$\not{E}_T$ final state, for different DM mass choices, with $M_{\mathrm{med}} =$1 TeV.
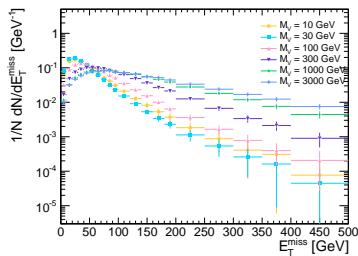
(c) Missing transverse momentum distribution for the leptonic Z+$\not{E}_T$ final state, for different mediator mass choices, for $m_{\mathrm{DM}} =$15 GeV
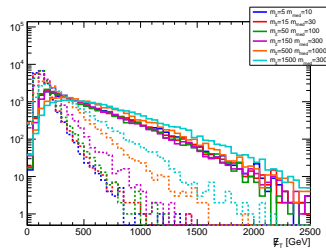
(d) Missing transverse momentum distribution for the hadronic W+$\not{E}_T$ final state.

Figure 2.10: Kinematic distributions relevant for searches with W, Z and photons in the final state, for the simplified model with a vector mediator exchanged in the $s-$channel.
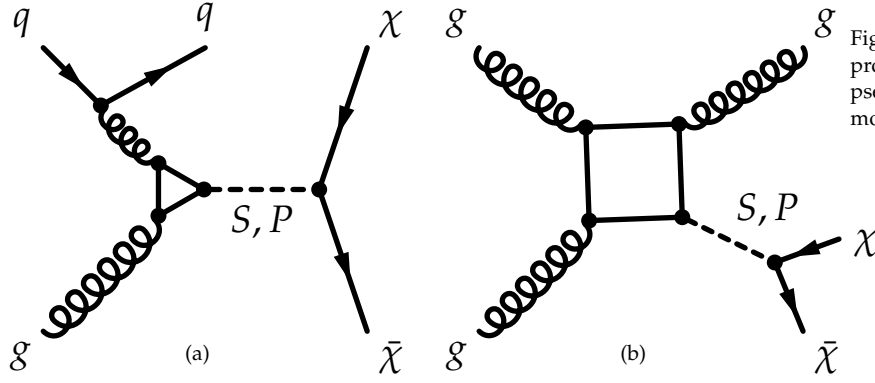
Figure 2.11: One-loop diagrams of processes exchanging a scalar (S) or pseudoscalar (P) mediator, leading to a mono-jet signature.

2.2 Scalar and pseudoscalar mediator, s-channel exchange

In this section, we consider a parallel situation to the DMV and DMA mediators in the previous sections: a real scalar or a pseudoscalar where the associated scalar is decoupled at higher energies[1]. This section is largely based on Refs. [BFG15, HKSW15] which contain a thorough discussion of these models.

Under MFV, spin-0 resonances look like an alternate-reality version of the SM Higgs. Relative to the DMV and DMA discussed above, these DMS and DMP models are distinguished by the special consequences of the MFV assumption, the very narrow width of the mediator and its extreme sensitivity to which decays are kinematically available, and the loop-induced coupling to gluons. The interaction Lagrangians are

$$
\mathcal{L}_\phi = g_{\mathrm{DM}}\phi\bar{\chi}\chi + \frac{\phi}{\sqrt{2}} \sum_i \left(g_u y_i^u \bar{u}_i u_i + g_d y_i^d \bar{d}_i d_i + g_\ell y_i^\ell \bar{\ell}_i \ell_i \right) \quad (2.9)
$$

$$
\mathcal{L}_a = i g_{\mathrm{DM}} a \bar{\chi}\gamma_5\chi + \frac{ia}{\sqrt{2}} \sum_i \Big(g_u y_i^u \bar{u}_i \gamma_5 u_i + g_d y_i^d \bar{d}_i \gamma_5 d_i +
$$

$$
g_\ell y_i^\ell \bar{\ell}_i \gamma_5 \ell_i \Big) . \quad (2.10)
$$

where the Yukawa couplings y_i^f are normalized to the Higgs vev as $y_i^f = \sqrt{2} m_i^f / v$.

The couplings to fermions are proportional to the SM Higgs couplings, yet one is still allowed to adjust an overall strength of the coupling to charged leptons and the relative couplings of u- and d-type quarks. As in the preceding sections, for the sake of simplicity and straightforward comparison, we reduce the couplings to the SM fermions to a single universal parameter $g_q \equiv g_u = g_d = g_\ell$.[2] The relative discovery and exclusion power of each search can be compared in this framework. However, we again emphasize the importance of searching the full set of allowed channels in case violations of these simplifying assumptions lead to significant modifications of the decay rates that unexpectedly favor different channels than the mix obtained under our assumptions. The coupling g_{DM} parameterizes the entire dependence on the structure between the mediator and the dark sector.

[1] This assumption does not hold in a UV-complete model where the two components of the complex scalar mediator would be approximately degenerate. The complex scalar case could be studied separately in the case of heavy flavor final states given the sufficiently different kinematics.

[2] The contribution from $\tau^+\tau^-$ decays plays no role for most of the parameter space considered.

555   Given these simplifications, the minimal set of parameters under
556 consideration is

$$\left\{ m_{\text{DM}},\ m_{\phi/a} = M_{\text{med}},\ g_{\text{DM}},\ g_{\text{q}} \right\}. \tag{2.11}$$

557 Fig. 2.11 shows the one-loop diagrams producing a jet+X signature.
558   The minimal mediator width is given by

$$\Gamma_{\phi,a} = \sum_f N_c \frac{y_f^2 g_q^2 m_{\phi,a}}{16\pi} \left(1 - \frac{4m_f^2}{m_{\phi,a}^2} \right)^{x/2} + \frac{g_{\text{DM}}^2 m_{\phi,a}}{8\pi} \left(1 - \frac{4m_{\text{DM}}^2}{m_{\phi,a}^2} \right)^{x/2}$$
$$+ \frac{\alpha_s^2 y_t^2 g_q^2 m_{\phi,a}^3}{32\pi^3 v^2} \left| f_{\phi,a} \left(\frac{4m_t^2}{m_{\phi,a}^2} \right) \right|^2 \tag{2.12}$$

559 where $x = 3$ for scalars and $x = 1$ for pseudoscalars. The loop
560 integrals are

$$f_\phi(\tau) = \tau \left[1 + (1 - \tau)\arctan^2 \left(\frac{1}{\sqrt{\tau - 1}} \right) \right], \tag{2.13}$$

$$f_a(\tau) = \tau \arctan^2 \left(\frac{1}{\sqrt{\tau - 1}} \right) \tag{2.14}$$

561 where $\tau = 4m_t^2/m_{\phi,a}^2$, and, for $\tau > 1$,

$$f_\phi(\tau) = \tau \left[1 + (1 - \tau) \left(-\frac{1}{4} \left(\log \frac{1 + \sqrt{1 - \tau}}{1 - \sqrt{1 - \tau}} + i\pi \right)^2 \right) \right], \tag{2.15}$$

$$f_a(\tau) = \tau \left(-\frac{1}{4} \left(\log \frac{1 + \sqrt{1 - \tau}}{1 - \sqrt{1 - \tau}} + i\pi \right)^2 \right). \tag{2.16}$$

562   The minimal widths for scalar and pseudo-scalar mediators with
563 $g_q = g_{\text{DM}} = 1$ are shown in Fig. 2.12, illustrating the effect of
564 choosing the SM Higgs-like Yukawa couplings for the SM fermions.
565 For the mediator mass above twice the top quark mass m_t, the
566 minimal width receives the dominant contribution from the top
567 quark. For lighter mediator masses, Dark Matter dominates as the
568 couplings to lighter quarks are Yukawa suppressed.
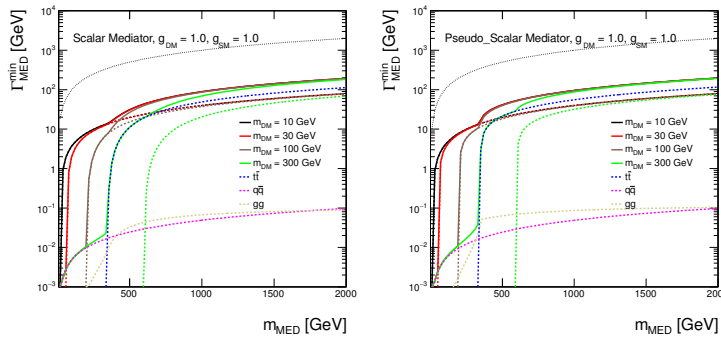
Figure 2.12: Minimal width as a function of mediator mass for scalar and pseudo-scalar mediator assuming couplings of 1. The total width is shown as solid lines for Dark Matter masses of m_{DM} =10 GeV, 30 GeV, 100 GeV and 300 GeV in black, red, brown and green, respectively. The individual contributions from Dark Matter are indicated by dotted lines with the same colors. The contribution from all quarks but top is shown as magenta dotted line and the contribution from top quarks only is illustrated by the dotted blue line. The dotted beige line shows the contribution from the coupling to gluons. The dotted black line shows the extreme case $\Gamma_{\min} = M_{\text{med}}$.

569   It can be seen in Fig. 2.13 that the kinematics for the scalar and
570 pseudoscalar models coincides when considering the diagrams

in Fig. 2.11. For this reason, we recommend to only generate only one of the two models, and report the cross-sections on HEPData for the other one. No preference is given between the two models as they have the same kinematics, although it is worth pointing out that the pseudo-scalar model has been used for a Dark Matter interpretation of the DAMA signal and of the galactic center excess [ADNP15].
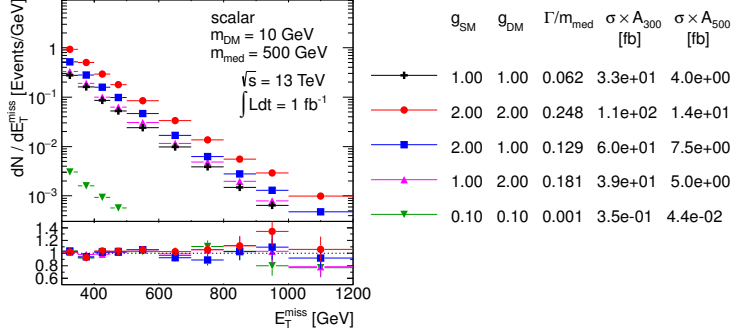
Figure 2.13: PLACEHOLDER: Comparison of the $\not{E}_T$ distributions for the scalar and pseudoscalar models for different DM and mediator masses. Ratios of the normalized distributions with respect to the first one are shown. A_{300} and A_{500} in the table denote the acceptance of the $\not{E}_T > 300$ GeV and $\not{E}_T > 500$ GeV cut, respectively.

2.2.1 Parameter scan

Similarly as in the case of the vector and axial-vector couplings of spin-1 mediators, scans in the parameter space are performed also for the scalar and pseudo-scalar couplings of the spin-0 mediators in order to decide on the optimized parameter grid for the presentation of Run-2 results. Figures 2.14- 2.18 show the scans over the couplings, Dark Matter mass and mediator mass and the same conclusions apply as in Section 2.1.

A scan over the mediator mass is shown in Fig. 2.18 where M_{med} = 300 GeV and 500 GeV are chosen to be below and above $2m_t$. The off-shell Dark Matter production regime is assumed by taking an extreme limit ($m_{\mathrm{DM}} = 1$ TeV) in order to study solely the effects of the couplings to quarks. No differences in the kinematic distributions are observed and also the cross sections remain similar in this case. No significant changes appear for mediator masses around the $2m_t$ threshold.

Figure 2.14: Scan over couplings. The $\not{E}_T$ distribution is compared for the scalar mediator models using the parameters as indicated. Ratios of the normalized distributions with respect to the first one are shown. A_{300} and A_{500} in the table denote the acceptance of the $\not{E}_T > 300$ GeV and $\not{E}_T > 500$ GeV cut, respectively.

The optimized parameter grid in the M_{med}–m_{DM} plane for scalar and pseudo-scalar mediators is motivated by similar arguments

Figure 2.15: Scan over Dark Matter mass. The $\not{E}_T$ distribution is compared for the scalar mediator models using the parameters as indicated. Ratios of the normalized distributions with respect to the first one are shown. A_{300} and A_{500} in the table denote the acceptance of the $\not{E}_T > 300$ GeV and $\not{E}_T > 500$ GeV cut, respectively.

Figure 2.16: Scan over Dark Matter mass. The $\not{E}_T$ distribution is compared for the scalar mediator models using the parameters as indicated. Ratios of the normalized distributions with respect to the first one are shown. A_{300} and A_{500} in the table denote the acceptance of the $\not{E}_T > 300$ GeV and $\not{E}_T > 500$ GeV cut, respectively.

Figure 2.17: Scan over mediator mass. The $\not{E}_T$ distribution is compared for the scalar mediator models using the parameters as indicated. Ratios of the normalized distributions with respect to the first one are shown. A_{300} and A_{500} in the table denote the acceptance of the $\not{E}_T > 300$ GeV and $\not{E}_T > 500$ GeV cut, respectively.
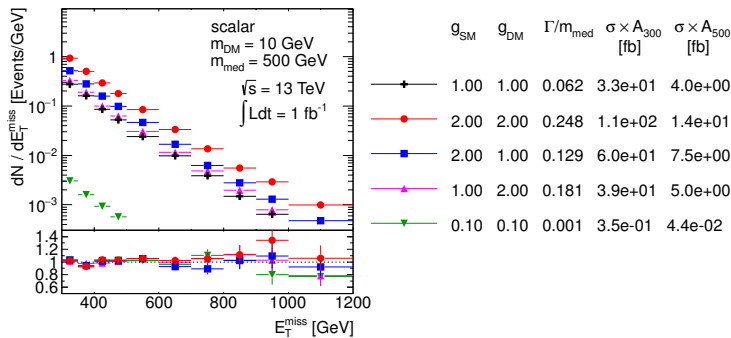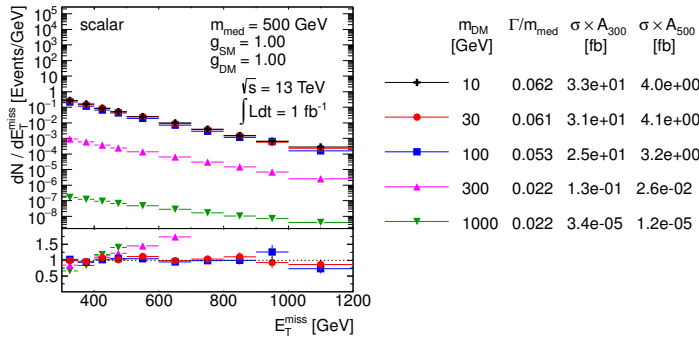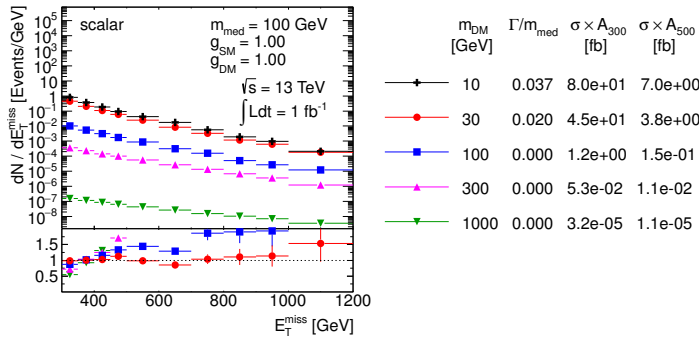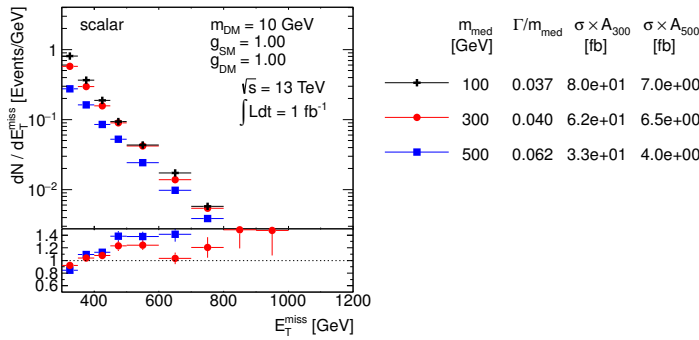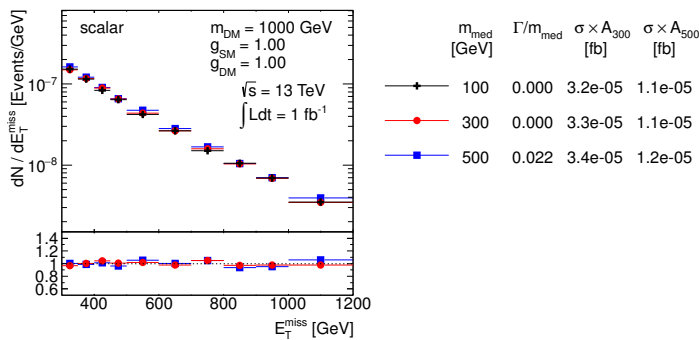

Figure 2.18: Scan over mediator mass. The $\not{E}_T$ distribution is compared for the scalar mediator models using the parameters as indicated. Ratios of the normalized distributions with respect to the first one are shown. A_{300} and A_{500} in the table denote the acceptance of the $\not{E}_T > 300$ GeV and $\not{E}_T > 500$ GeV cut, respectively.

as in the previous section. Therefore, a similar pattern is followed here, taking again $g_q = g_{DM} = 1$. Only the sensitivity to the highest mediator masses has to be re-evaluated. The generator level cross section times the acceptance at $\not{E}_T > 500$ GeV for the model with couplings $g_q = g_{DM} = 1$, light Dark Matter of $m_{DM} = 10$ GeV and a $M_{med} = 500$ GeV scalar mediator is at the order of 10 fb, i.e. just at the edge of the early Run-2 sensitivity. Increasing the mediator mass to 1 TeV pushes the product $\sigma \times A$ down to approximately 0.1 fb, below the LHC sensitivity. Therefore, we choose to remove the 2 TeV mediator mass from the grid and present the final grid with 32 mass points only, as shown in Tab. 2.3. One point at very high mediator mass (5 TeV) is added for each of the DM masses scanned, to aid the reinterpretation of results in terms of contact interaction operators (EFTs).

m_{DM} (GeV)	M_{med} (GeV)								
1	10	20	50	100	200	300	500	1000	5000
10	10	15	50	100					5000
50	10		50	95	200	300			5000
150	10				200	295	500		5000
500	10						500	995	5000
1000	10							1000	5000

Table 2.3: Simplified model benchmarks for $s-$channel simplified models (spin-0 mediators decaying to Dirac DM fermions in the scalar and pseudoscalar case, taking the minimum width for $g_q = g_{DM} = 1$)

2.2.2 Additional considerations for $V + \not{E}_T$ signatures

The parameters for the model with a scalar mediator exchanged in the $s-$ channel follow those in Section 2.

Even though the sensitivity of mono-boson searches to this model is low and it may not be in reach of early LHC searches, we recommend to generate this model for W, Z and photon searches in order to reproduce the kinematics of contact interaction operators that are further described in Section 3.2.1, for later reinterpretation.

2.2.3 Additional considerations for $t\bar{t}$ and $b\bar{b}$+MET signatures

With the MFV assumption, the top quark plays a primary role in the phenomenology: The model predicts not only the monojet process described in Section 2.2, but also production of dark matter in association with top pairs, as illustrated in Fig. 2.19. Dedicated searches including jets from heavy flavor quarks in the final state can be designed for this production mechanism. Another class of simplified models, which includes a Dark Matter interpretation among many others, and yields a single top quark in the final state, is detailed in Appendix B.1.

In some theoretically motivated scenario (e.g. for high $tan\beta$ in 2HDM in the pMSSM), spin-0 mediators might couple more strongly to down generation quarks. This assumption motivates the study of final states involving b-quarks as a complementary search to the $t\bar{t}$+DM models presented in the previous section, to directly
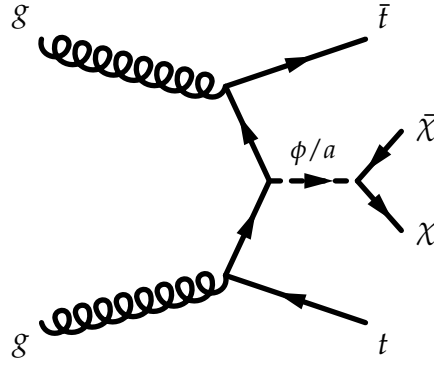
Figure 2.19: Representative Feynman diagram showing the pair production of dark matter particles in association with $t\bar{t}$.

probe the $b-$ quark coupling. An example of such a model can be found in Ref. [BFG15]

The parameter scan for the dedicated $t\bar{t}+\slashed{E}_T$ searches has been studied in detail to target the production mechanism of DM associated to heavy flavor quarks, still sharing many details of the scan for the scalar model with a gluon radiation The benchmark points scanning the model parameters have been selected to ensure that the kinematic features of the parameter space are sufficiently represented. Detailed studies were performed to identify points in the m_{DM}, $m_{\phi,a}$, g_{DM}, g_q (and $\Gamma_{\phi,a}$) parameter space that differ significantly from each other in terms of expected detector acceptance. Because missing transverse momentum is the key observable for searches, the mediator p_T spectra is taken to represent the main kinematics of a model. Another consideration in determining the set of benchmarks is to focus on the parameter space where we expect the searches to be sensitive during the 2015 LHC run. Based on a projected integrated luminosity of $30\,\mathrm{fb}^{-1}$ expected for 2015, we disregard model points with a cross section times branching ratio smaller than 0.1 fb, corresponding to a minimum of one expected event assuming a conservative 0.1% signal efficiency.

The kinematics is most dependent on the masses m_{DM} and $m_{\phi,a}$. Figure 2.20 and 2.21 show typical dependencies for scalar and pseudoscalar couplings respectively. Typically, the mediator p_T spectra broadens with larger $m_{\phi,a}$. The kinematics are also different between on-shell ($M_{\mathrm{med}} > 2m_{\mathrm{DM}}$) and off-shell ($M_{\mathrm{med}} < 2m_{\mathrm{DM}}$) mediators as in Section 2.2. Furthermore, the kinematic differences in $\slashed{E}_T$ spectrum between scalar and pseudoscalar are larger for light mediator masses with respect to heavier mediators. It is therefore important to benchmark points covering on-shell and off-shell mediators with sufficient granularity, including the transition region between on-shell and off-shell mediators.

Typically only weak dependencies on width or equivalently couplings are observed (see Fig 2.22), except for large mediator masses of $\sim 1.5\,\mathrm{TeV}$ or for very small couplings of $\sim 10^{-2}$. These regimes where width effects are significant have production cross sections that are too small to be relevant for $30\,\mathrm{fb}^{-1}$ and are not considered here. However, with the full Run-2 dataset, such models may be within reach. The weak dependence on the typical width values can be understood as the parton distribution function are the dominant effect on mediator production. As shown in Section 2.1.1,
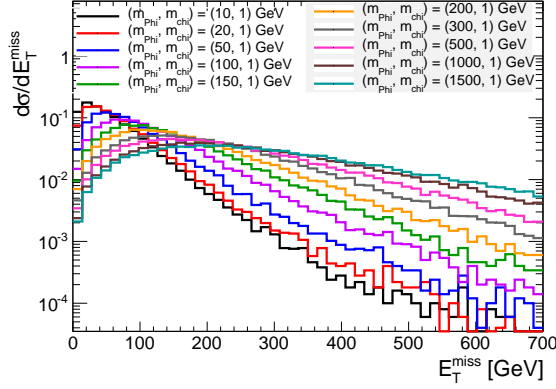
Figure 2.20: Example of the dependence of the kinematics on the scalar mediator mass. The Dark Matter mass is fixed to be $m_{\text{DM}} = 1\text{GeV}$.
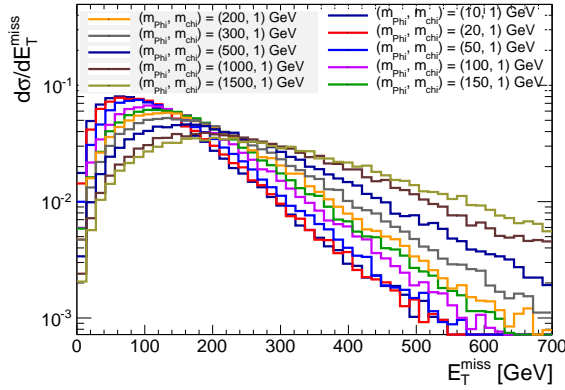
Figure 2.21: Example of the dependence of the kinematics on the pseudoscalar mediator mass. The Dark Matter mass is fixed to be $m_{\text{DM}} = 1\text{GeV}$.

for couplings $\sim O(1)$ the width is large enough that the p_T of the mediator is determined mainly by the PDF.
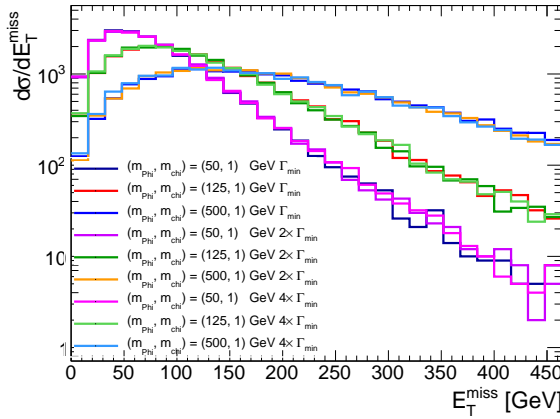
Figure 2.22: Study of the dependence of kinematics on the width of a scalar mediator. The width is increased up to four times the minimal width for each mediator and dark matter mass combination.

Another case where the width can impact the kinematics is when $m_{\phi,a}$ is slightly larger than $2m_\chi$. Here, the width determines the relative contribution between on-shell and off-shell mediators. An example is given in Fig. 2.23. As the minimal width choice pursued in this document is the most conservative one, this effect can be neglected in order to reduce the number of benchmark points to be generated.

The points for the parameter scan chosen for this model are
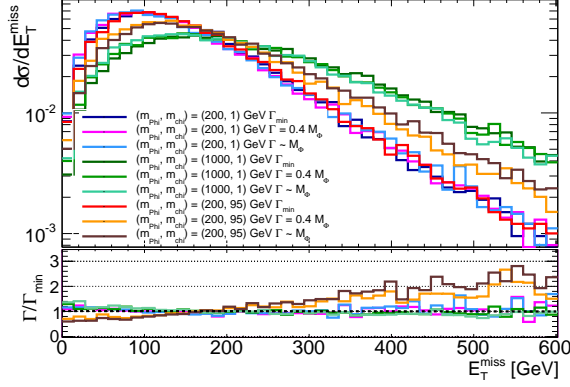
Figure 2.23: Dependence of the kinematics on the width of a scalar mediator. The width is increased up to the mediator mass. Choices of mediator and dark matter masses such that $m_{\phi,a}$ is slightly larger than $2m_\chi$ is the only case that shows a sizeable variation of the kinematics as a function of the width.

listed in Table 2.3, chosen to be harmonized with those for other analyses employing the same scalar model as benchmark. Based on the sensitivity considerations above, DM masses are only simulated up to 500 GeV (but the 5 TeV mediator point is retained) leading to a total of 24 benchmark points. However for these searches we recommend to generate scalar and pseudoscalar models separately, as the kinematics differs due to the different coupling of the mediator to the final state top quarks in the two cases, as shown in Figs. 2.20 and 2.21.

Similar studies were performed in the $b\bar{b}$ case. It was found that they show the same weak dependence of the kinematics of the event on the mediator width. The same benchmark parameters of the $t\bar{t}$ case could then be chosen.

2.3 Colored scalar mediator, t-channel exchange

The preceding sections address models with a Dirac fermion coupled to the SM through exchange of a neutral spin-0 or spin-1 in an s-channel process. A t-channel process may couple the SM and DM directly, leading to a different phenomenology. Here, we examine a model where χ is a Standard Model (SM) singlet, a Dirac fermion; the mediating particle, labeled ϕ, is charged and coloured; and the SM particle is a quark. Such models have been studied in Refs. [AWZ14b, PVZ14].

Following the example of Ref. [PVZ14], the interaction Lagrangian is written as

$$\mathcal{L}_{\text{int}} = g \sum_{i=1,2} (\phi_L^i \bar{Q}_L^i + \phi_{uR}^i \bar{u}_R^i + \phi_{dR}^i \bar{d}_R^i)\chi \qquad (2.17)$$

where Q_L^i, u_R^i and d_R^i are the SM quarks and ϕ_L^i, ϕ_{uR}^i and ϕ_{dR}^i are the corresponding mediators, which (unlike the s-channel mediators) must be heavier than χ. These mediators have SM gauge representations under $(SU(3), SU(2))_Y$ of $(3,2)_{-1/6}$, $(3,1)_{2/3}$ and $(3,1)_{-1/3}$ respectively. Variations of the model previously studied in the literature include coupling to the left-handed quarks only [CEHL14, BDSJ$^+$14], to the ϕ_{uR}^i [DNRT13] or ϕ_{dR}^i [PVZ14,

₇₁₄ A⁺14a], or some combination [BB13b, AWZ14a].

₇₁₅ As for the *s*-channel models, we assume Minimal Flavor Viola-
₇₁₆ tion (MFV), setting the mediator masses for each flavor equal; the
₇₁₇ same logic also applies to the couplings g. Coupling to the third
₇₁₈ generation breaks the MFV assumption and is thus forbidden. The
₇₁₉ free parameters are then

$$\{m_{\rm DM}, M_\phi, g\}. \tag{2.18}$$

₇₂₀ The minimal width of each mediator is expressed, using the
₇₂₁ example of decay to an up quark, as

$$\Gamma(\phi_i \to \bar{u}_i \chi) = \frac{g_i^2}{16\pi M_{\phi_i}^3}(M_{\phi_i}^2 - m_{u_i}^2 - m_{\rm DM}^2)$$
$$\times \sqrt{(M_{\phi_i}^2 - (m_{u_i} + m_{\rm DM})^2)(M_{\phi_i}^2 - (m_{u_i} - m_{\rm DM})^2)}, \tag{2.19}$$

₇₂₂ which reduces to

$$\frac{g_i^2 M_{\phi_i}}{16\pi}\left(1 - \frac{m_{\rm DM}^2}{M_{\phi_i}^2}\right)^2 \tag{2.20}$$

₇₂₃ in the limit $M_{\phi_i}, m_{\rm DM} \gg m_{u_i}$.

₇₂₄ We note that in SUSY models, the width is generally fixed by the
₇₂₅ couplings assumed in the model, while it could be wider in case of
₇₂₆ large $m_{\rm DM}$, leading to different kinematic distributions between the
₇₂₇ two kinds of benchmarks.
₇₂₈ The leading-order processes involved in MET+jet production are
₇₂₉ shown in Fig. 2.24. Note that the generation index for ϕ is linked
₇₃₀ to the incoming fermion(s). Thus, mono-jet production via ϕ_u^3 is
₇₃₁ not possible at this order, while production through ϕ_d^3 is sup-
₇₃₂ pressed by the *b* parton PDF. This model can also give a signal in
₇₃₃ the di-jet + MET channel when, for example, the χ is exchanged
₇₃₄ in the *t*-channel and the resulting ϕ pair each decay to a jet + χ.
₇₃₅ Fig. 2.25 shows the leading order diagrams. Except for the gg in-
₇₃₆ duced process, di-jet production through ϕ_u^3 is not possible, and
₇₃₇ production through ϕ_d^3 is again suppressed. The diagram involv-
₇₃₈ ing the *t*-channel exchange of χ is strongly dependent upon the
₇₃₉ Dirac fermion assumption. For a Majorana fermion, $q\bar{q}$, $\bar{q}\bar{q}$, and qq
₇₄₀ production would be possible with the latter having a pronounced
₇₄₁ enhancement at the LHC.
₇₄₂ This model is similar to the simplified model considered in SUSY
₇₄₃ searches, implemented as the MSSM with only light squarks and a
₇₄₄ neutralino, except for two distinct points: the χ is a Dirac fermion
₇₄₅ and the coupling g is not limited to be weak scale ($g \ll 1$). In the
₇₄₆ MSSM, most of these processes are sub-dominant, even if reso-
₇₄₇ nantly enhanced, because the production is proportional to weak

748 couplings. In the more general theories considered here, g is free
749 to take on large values of order 1 or more, and thus diagrams ne-
750 glected in MSSM simulation can occur at a much higher rate here.
751 While constraints from SUSY jets+MET analyses on MSSM mod-
752 els can be recast to apply to the specific model in this report, DM
753 searches should also directly test their sensitivity to the MSSM
754 benchmark models.
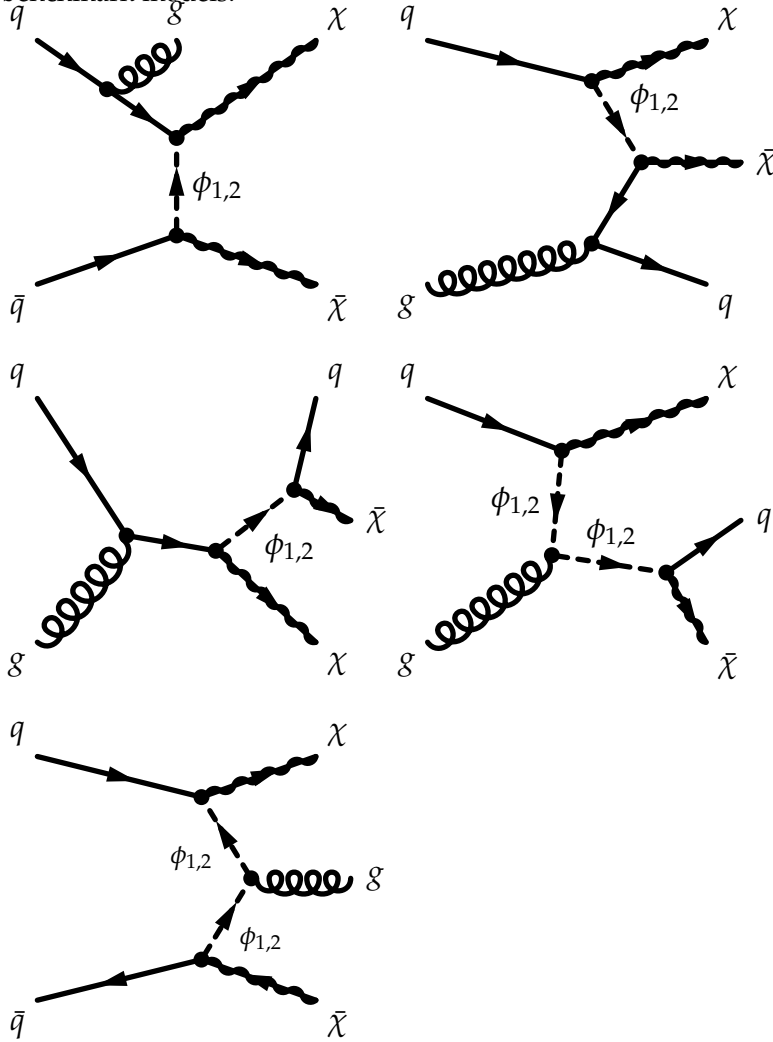
Figure 2.24: Leading order mono-jet t-channel processes, adapted from [PVZ14].

2.3.1 Parameter scan

756 Ref. [PVZ14] studies the parameter space and obtains bounds on
757 this model from LHC Run 1 mono-jet and dijets+MET data. The
758 Forum did not exhaustively compare the kinematic distributions
759 of this model as was done in the s-channel case. While this means
760 the recommendations below should be taken with more caution, the
761 model is plausible and distinctive, and it should be included in the
762 design of LHC searches.
763   As in the s-channel models, scans should be performed over
764 m_{DM} and M_ϕ. The viable ranges of both parameters nearly coin-
765 cide with the scan proposed for the s-channel; for simplicity we
766 recommend adopting the s-channel mono-jet grid.
767   The rates of the first three diagrams of Fig. 2.24 scale as one with
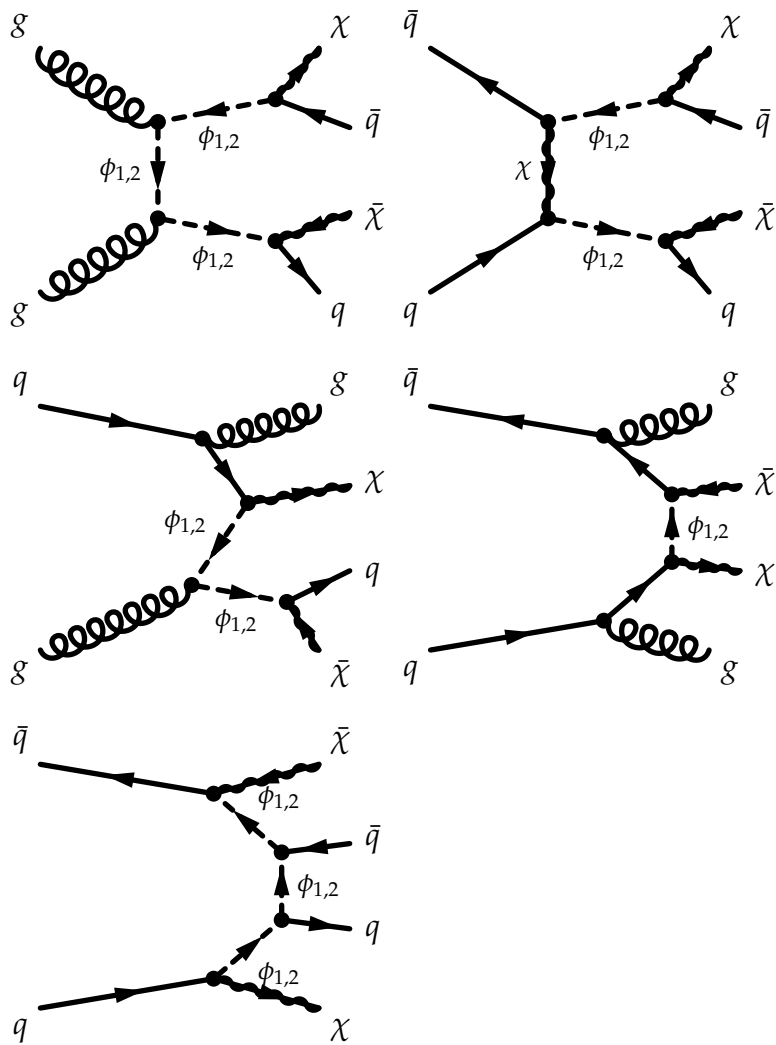
Figure 2.25: Leading order two-jet *t*-channel processes, adapted from [PVZ14].

the coupling g. In the heavy mediator limit, then, the kinematic distributions depend only indirectly on the coupling through the effect on the minimal mediator width. In contrast with the s-channel case, however, the bounds one obtains from X+MET searches depends strongly on the width of the mediator, as is visible in Figs. 5 and 6 of Ref. [PVZ14], except in the heavy mediator limit ($M_\phi \approx 2\,\text{TeV}$). A scan over the width was not available for this report; thus we recommend scanning a range of possible widths as discussed in a more-limited way for the s-channel mono-jet, spanning from the minimal width to a value approaching the particle limit (for example, $\Gamma \approx M_\phi/3$ in Ref. [PVZ14]).

2.3.2 Additional considerations for $V + \not{E}_T$ signatures

The model parameters with emission of an EW boson generally follow those in Section 2, even though fewer diagrams are involved. A representative Feynman diagram can be constructed by replacing a gluon in Fig. 2.24 with a γ, W, Z boson. See Ref. [BDG$^+$12] for a theoretical overview of this model with specific examples for the $Z+\not{E}_T$ final state.

Figure 2.26 shows the $\not{E}_T$ distribution for the hadronic $Z+\not{E}_T$ final state, with varying dark matter and mediator mass, before any selection. The acceptance for a series of simplified analysis cuts ($\not{E}_T$ >350 GeV, leading jet $p_T > 40$ GeV, minimum azimuthal angle between jet and $\not{E}_T > 0.4$) applied at the generator level is shown in Figure 2.27.
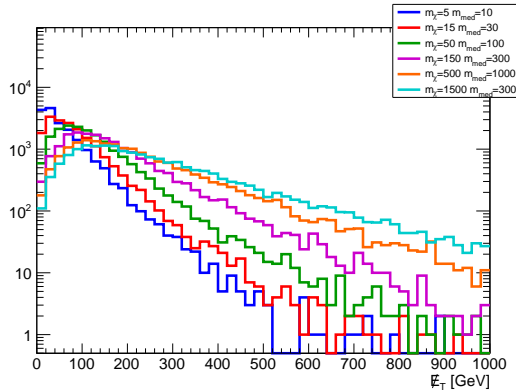
Figure 2.26: Missing transverse momentum distribution for the hadronic $Z+\not{E}_T$ final state, for the simplified model with a colored scalar mediator exchanged in the $t-$channel.

The parameter scan for the $t-$ channel model in the case of signatures including EW bosons follows that of the monojet case.

2.3.3 Additional considerations for signatures with a single $b-$quark + MET

Models of bottom-flavored Dark Matter that are closely related to the $t-$channel mediated model from this Section have been proposed in Refs. [LKW13, ABHL14]. Here, DM couples preferentially
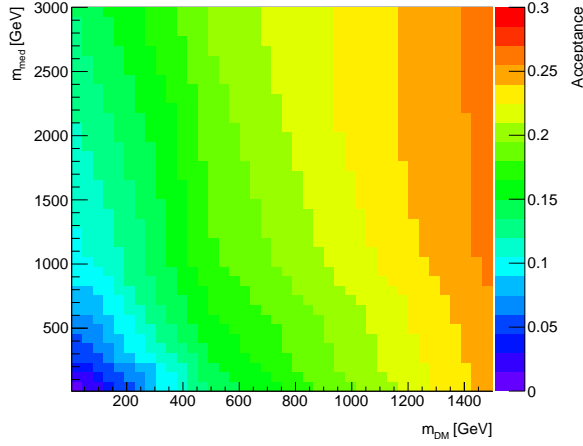
Figure 2.27: Acceptance for the hadronic $Z+\not{E}_T$ final state, for the simplified model with a colored scalar mediator exchanged in the $t-$channel.

to bottom quarks, with a decoupled third generation. We describe the b-FDM model of Ref. [ABHL14], created to explain the Galactic Center (GC) gamma-ray excess observed in data collected by the Fermi-LAT collaboration [DFH$^+$14].

   The interest in this model lies in producing an annihilation cross section consistent with the gamma-ray excess can be achieved for perturbative values of the couplings, while being consistent with LHC constraints on the colored mediator. For parameters capable of explaining the anomalous gamma-ray signal in terms of Dark Matter coupling preferentially to $b-$ quarks, the model predicts a direct detection cross section that is consistent with current constraints, but within the near future reach of Direct Detection experiments. The model will be decisively tested with data from the upcoming high-energy run at the LHC.

   The model contains a Dirac fermion transforming as a flavor triplet. The third component of the triplet χ_b comprises the cosmological DM. A flavor singlet, color triplet scalar field Φ mediates the interactions between the DM and the Standard Model quarks. The model is similar to the MSSM with a light bottom squark and neutralino, and is thus a flavor-specific example of a t-channel model.

   The Lagrangian considered is given by

$$-\mathcal{L} \supset g\Phi^*\chi_b b_R + \text{h.c.} \tag{2.21}$$

   Within the framework of minimal flavor violation, the other fermions in the flavor triplet can be made sufficiently heavy and weakly-coupled that they can be neglected in the analysis.

Parameter scan   The nature of the model doesn't allow to derive a simple scaling behavior which would allow us reduce the number of points to be simulated. This is because of the interference of diagrams with QCD production of the mediator (which scale as g_s^2) with diagrams that are proportional to the coupling g in the $b+\not{E}_T$ and $b\bar{b}+\not{E}_T$ final states. Fixing the couplings also fixes the mediator width, when adopting the minimal width assumption.

829   A full study of the parameter scan for this model was not avail-
830   able for this report; thus we recommend scanning a range of pos-
831   sible widths as discussed in a more-limited way for the *s*-channel
832   mono-jet, spanning from the minimal width to a value approach-
833   ing the particle limit. A sizable, $O(1)$ coupling benchmark such
834   as $g = 1$ should be considered for each mass point since this
835   would be a distinctive feature of this benchmark from SUSY mod-
836   els with sbottom squarks (see Section 2.3 for further discussion):
837   Cross-sections for unit couplings can be found in Appendix **??**.
838   The coupling could also be chosen to fulfill constraints from the
839   relic density (see Appendix **??**, with corresponding cross sections in
840   Tables **??** onwards).
841   A scan of Dark Matter and mediator masses should be done in
842   the on-shell region $MPhi > m_{\mathrm{DM}} + m_b$, since the cross-sections
843   in the off-shell region are too small to be sensitive with early LHC
844   data, spanning from 10 to 500 GeV in m_{DM} and from 10 to 1300 GeV
845   in M_{med}.
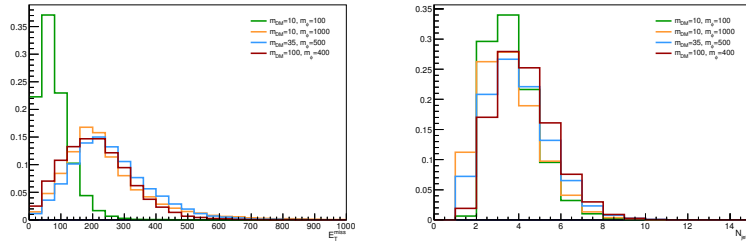
Figure 2.28: MET (left) and jet mul-
tiplicity (right) for various DM and
mediator masses and couplings nor-
malized to the relic density observed
in the early universe.
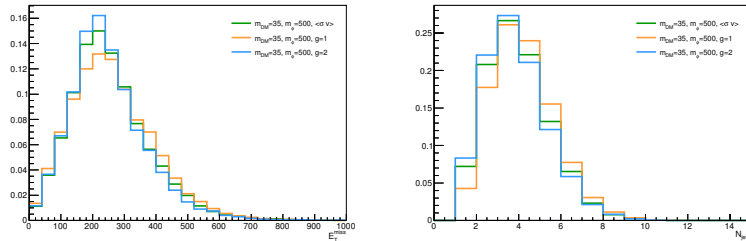
Figure 2.29: MET (left) and jet mul-
tiplicity (right) for $m_{\mathrm{DM}} = 35$ GeV
and $MPhi = 500$ GeV for couplings
corresponding to relic density weights
and also $g = 1, 2$

846   *2.4   Spin-2 mediator*

847   In models with extra dimensions, the Kaluza-Klein excitations of
848   the graviton could also serve as a mediator between the Standard
849   Model and dark sector physics. This kind of model was not studied
850   in the forum and is not included in the recommendations, but it
851   and models such as Ref. [LPS14] may warrant further study on a
852   longer timescale.

853   *2.5   Presentation of results for reinterpretation of s-channel me-*
854   *diator models*

855   The aim of the parameter grid optimization done for the *s*-channel
856   models in the previous Sections is to reduce the parameter space

for simulation using neighboring grid points to populate the missing parts. There are two possible choices:

- Interpolation is used in-between the grid points that are close enough such that finer granularity is not needed for the presentation purposes, or between the points where smooth or no changes of the results are expected. The latter argument is exactly the one that motivates the reduction of the grid points in the M_{med}–m_{DM} plane.

- Results can be recalculated when the dependencies with respect to the neighboring grid points are known.

The results of the scan over the couplings presented in the previous sections indicate there are no changes in kinematic distributions for different choices of the coupling strengths. This means that the acceptance remains the same in the whole g_{q}–g_{DM} plane and it is sufficient to perform the detector simulation only for one single choice of $g_{\mathrm{q}}, g_{\mathrm{DM}}$. The resulting truth-level selection acceptance and the detector reconstruction efficiency can then be applied to all remaining grid points in the g_{q}–g_{DM} plane where only the generator-level cross section needs to be known. This significantly reduces the computing time as the detector response is by far the most expensive part of the Monte Carlo sample production. However, the number of generated samples can be reduced even further if a parameterization of the cross section dependence from one grid point to another exists. The following section describes the details of a cross section scaling procedure that can be used to reinterpret results for a fixed coupling for s-channel mediator models.

The propagator for the s-channel exchange is written in a Breit-Wigner form as $\frac{1}{q^2 - M_{\mathrm{med}}^2 + iM_{\mathrm{med}}\Gamma}$, where q is the momentum transfer calculated from the two partons entering the hard process after the initial state radiation, which is equivalent to the invariant mass of the Dark Matter pair. The size of the momentum transfer with respect to the mediator mass allows to classify the production in the following way:

- off-shell production when $q^2 \gg M_{\mathrm{med}}$ leading to suppressed cross sections,

- on-shell production when $q^2 \sim M_{\mathrm{med}}$ leading to enhanced cross sections,

- effective field theory (EFT) limit when $q^2 \ll M_{\mathrm{med}}$.

All three categories can be distinguished in Fig. 4.1 showing the upper limit on the interaction scale $M^* \equiv M_{\mathrm{med}}/\sqrt{g_{\mathrm{q}}g_{\mathrm{DM}}}$ for vector mediator. In the case of the off-shell production and the EFT limit, the first and second term in the propagator dominate, respectively, which reduces the dependence on the mediator width. Therefore, in these cases one can approximate the cross section as

$$\sigma \propto g_{\mathrm{q}}^2 g_{\mathrm{DM}}^2. \tag{2.22}$$

901 The on-shell production regime is the most interesting one as it
902 gives the best chances for a discovery at the LHC given the cross
903 section enhancement. The propagator term with the width cannot
904 be neglected in this case and, in the narrow width approximation
905 which requires $\Gamma \ll M_{\text{med}}$ (this is not necessarily the case in the
906 benchmarks considered in the scans), one can integrate

$$\int \frac{ds}{(s - M_{\text{med}}^2)^2 + M_{\text{med}}^2 \Gamma^2} = \frac{\pi}{M_{\text{med}} \Gamma} \qquad (2.23)$$

907 which further implies the cross section scaling

$$\sigma \propto \frac{g_q^2 g_{\text{DM}}^2}{\Gamma}. \qquad (2.24)$$

908 The narrow with approximation is important here as it ensures
909 an integration over parton distribution functions (PDFs) can be
910 neglected. In other words, it is assumed the integrand in Eq. 2.23
911 is non-zero only for a small region of s, such that the PDFs can be
912 taken to be constant in this range. Since $\Gamma \sim g_q^2 + g_{\text{DM}}^2$, one can
913 simplify this rule in the extreme cases as follows

$$\sigma \quad \propto \quad \frac{g_q^2 g_{\text{DM}}^2}{g_q^2 + g_{\text{DM}}^2} \xrightarrow{g_q \ll g_{\text{DM}}} g_q^2 \qquad (2.25)$$

$$\sigma \quad \propto \quad \frac{g_q^2 g_{\text{DM}}^2}{g_q^2 + g_{\text{DM}}^2} \xrightarrow{g_q \gg g_{\text{DM}}} g_{\text{DM}}^2 . \qquad (2.26)$$

914 However, it is important to keep in mind that this formula omits
915 color and multiplicity factors as well as possible Yukawa suppres-
916 sion, and there is no simple scaling rule for how the cross section
917 changes with the Dark Matter mass and the mediator mass, or for
918 mediators with a large width, because PDFs matter in such cases as
919 well. Therefore, the scaling procedure outlined above is expected to
920 work only for fixed masses and fixed mediator width, assuming the
921 narrow width approximation applies.
922   Figures 2.30 and 2.31 show the minimal width in the g_q–g_{DM}
923 plane for all vector, axial-vector, scalar and pseudo-scalar mediators
924 for $M_{\text{med}} = 100$ GeV and 1000 GeV, respectively, taking $m_{\text{DM}} =$
925 10 GeV. The individual colors indicate the lines of constant width
926 along which the cross section scaling works. For vector and axial-
927 vector mediators, the minimal width is predominantly defined by
928 g_q due to the number of quark flavors and the color factor. On the
929 contrary, both the Standard Model and Dark Matter partial width
930 have comparable contributions in case of scalar and pseudo-scalar
931 mediators if the top quark channel is open ($M_{\text{med}} > 2m_t$). However,
932 mostly g_{DM} defines the minimal width for $M_{\text{med}} < 2m_t$ due to the
933 Yukawa-suppressed light quark couplings.

To do **Reduce plots to mMed<GammaMin region (??)**

934   The performance of the cross section scaling is demonstrated in
935 Fig. 2.32 where two mass points $M_{\text{med}} = 100$ GeV and 1 TeV with
936 $m_{\text{DM}} = 10$ GeV are chosen and rescaled from the starting point
937 $g_q = g_{\text{DM}} = 1$ according to Eq. 2.24 to populate the whole g_q–g_{DM}

Figure 2.30: Minimal width for vector, axial-vector, scalar and pseudo-scalar mediators as a function of the individual couplings g_q and g_{DM}, assuming $M_{med} = 100$ GeV and $m_{DM} = 10$ GeV. The limiting case $\Gamma_{min} = M_{med}$ is indicated by the black line.
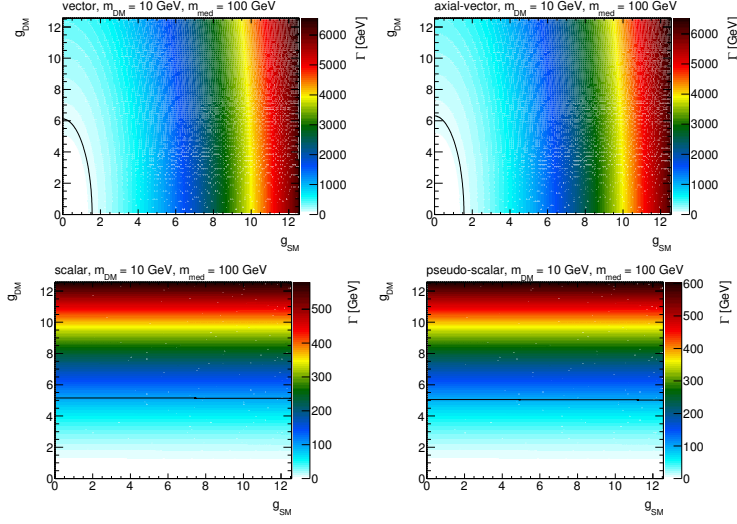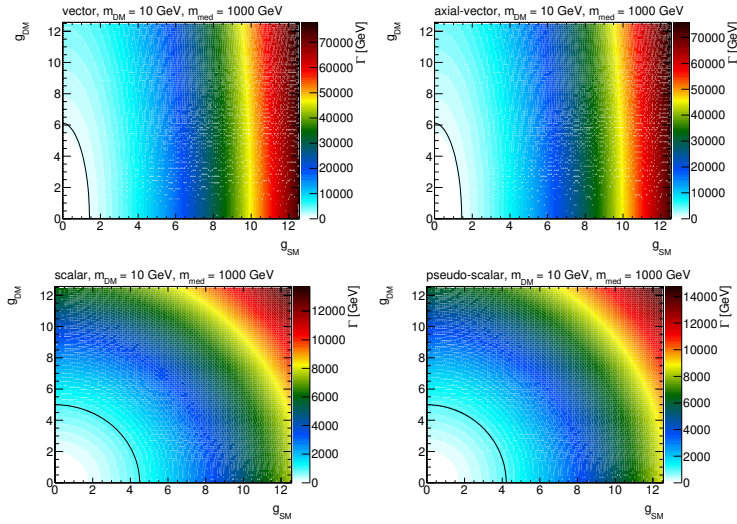

Figure 2.31: Minimal width for vector, axial-vector, scalar and pseudo-scalar mediators as a function of the individual couplings g_q and g_{DM}, assuming $M_{med} = 1$ TeV and $m_{DM} = 10$ GeV. The limiting case $\Gamma_{min} = M_{med}$ is indicated by the black line.

938 plane. This means the width is not kept constant in this test and
939 this is done in purpose in order to point out deviations from the
940 scaling when the width is altered. For each mass point, the rescaled
941 cross section is compared to the generator cross section and the
942 ratio of the two is plotted. For the given choice of the mass points,
943 the scaling seems to work approximately with the precision of
944 $\sim 20\%$ in the region where $\Gamma_{min} < M_{med}$. Constant colors indicate
945 the lines along which the cross section scaling works precisely and
946 there is a remarkable resemblance of the patterns shown in the
947 plots of the mediator width. To prove the scaling along the lines
948 of constant width works, one such line is chosen in Fig. 2.33 for a
949 scalar mediator, defined by $M_{med} = 300$ GeV, $m_{DM} = 100$ GeV,
950 $g_q = g_{DM} = 1$, and the rescaled and generated cross sections are
951 found to agree within 3%.
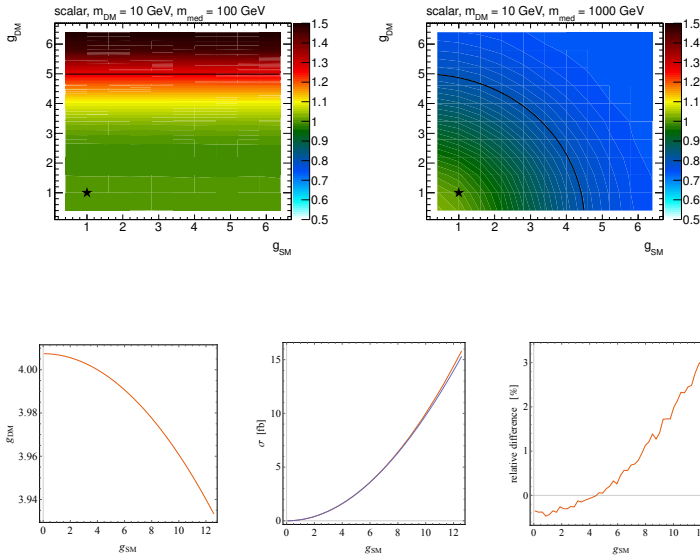
Figure 2.32: Ratio of the rescaled and generated cross sections in the g_q–g_{DM} plane. The point at $g_q = g_{DM} = 1$, taken as a reference for the rescaling, is denoted by a star symbol. Scalar model with $M_{med} = 100$ GeV (left) and 1 TeV (right) is plotted for $m_{DM} = 10$ GeV. The limiting case $\Gamma_{min} = M_{med}$ is shown as a black line.

Figure 2.33: Scaling along the lines of constant width. The line of constant width for $M_{med} = 300$ GeV and $m_{DM} = 100$ GeV, intercepting $g_q = g_{DM} = 4$ is shown on left. The generated and rescaled cross sections are compared in the middle, the corresponding ratio is shown on right.

952 *Proposed parameter grid for cross-section scaling*   We propose to de-
953 liver collider results in the g_q–g_{DM} plane using the following pre-
954 scription, to ease reinterpretation through cross-section scaling:

955 • Since the shapes of kinematic quantities do not change for differ-
956   ent couplings, use the acceptance and efficiency for the available
957    $m_{DM} = 50$ GeV, $M_{med} = 300$ GeV, $g_q = g_{DM} = 1$ grid point from
958   the M_{med}–m_{DM} plane for the scalar and pseudo-scalar mediator.
959   In case of the vector and axial-vector mediator, use the grid point
960    $m_{DM} = 50$ GeV, $M_{med} = 1$ TeV, $g_q = g_{DM} = 1$.

961 • Generate additional samples in order to get generator cross
962   sections only. For scalar and pseudo-scalar mediator, choose
963    $m_{DM} = 50$ GeV, $M_{med} = 300$ GeV with the following values
964   for $g_q = g_{DM}$: 0.1, 1, 2, 3. For vector and axial vector mediator,
965   choose $m_{DM} = 50$ GeV, $M_{med} = 1$ TeV with the following values
966   for $g_q = g_{DM}$: 0.1, 0.25, 0.5, 0.75, 1.25, 1.5. The upper values are
967   defined by the minimal width reaching the mediator mass.

To do **Waiting for scalar mediator calculation of perturbativity limit from J. Alcaraz.). (??)**

- Rescale the generator cross sections for on-shell resonance pro-
  duction along the lines of constant width in order to populate
  the whole g_q–g_{DM} plane.

Rescaling to different mediator width   In general it is also important
to consider a larger mediator width than Γ_{min} in order to accom-
modate additional interactions of the mediator with the visible and
hidden sector particles [BFG15, HKSW15]. If the narrow width ap-
proximation applies, the cross section scaling method described
above can be used to reinterpret the results presented for the mini-
mal width, since multiplying the width by factor n is equivalent to
changing the coupling strength by factor $\sqrt{n}$, i.e.

$$\sigma(g_q, g_{DM}, n\Gamma_{min}(g_q, g_{DM})) \propto \frac{g_q^2 g_{DM}^2}{\Gamma_{min}(\sqrt{n}g_q, \sqrt{n}g_{DM})} \ . \qquad (2.27)$$

The cross section for the sample with couplings g_q and g_{DM} and
modified mediator width $\Gamma = n\Gamma_{min}$ can therefore be rescaled from
a sample generated with the minimal width corresponding to the
couplings scaled by $\sqrt{n}$ as described in the following formula.

$$\sigma(g_q, g_{DM}, n\Gamma_{min}(g_q, g_{DM})) = \frac{1}{n^2}\sigma(\sqrt{n}g_q, \sqrt{n}g_{DM}, \Gamma_{min}(\sqrt{n}g_q, \sqrt{n}g_{DM})) \qquad (2.28)$$

The advantage of doing this is in the fact that no event selection
and detector response needs to be simulated since the changes in
couplings do not have an effect on the shapes of kinematic distribu-
tions.

It should be noted again that this procedure is only useful when
the narrow width approximation applies. Care must be taken to
ensure that is the case. For example, in the DMV and DMA case, one
quickly breaks this approximation even for small n.

2.5.1   *Additional considerations for $t\bar{t}$ and $b\bar{b}$+MET signatures*

The cross-section scaling considerations shown in 2.5 still apply
for this model. Here we detail the specific studies done for the $t\bar{t}$
model.

Given that the kinematics are similar for all couplings $g =\sim 1$,
we recommend to generate only samples with $g_{DM} = g_q = 1$. It
follows from this that these benchmark points should be a good
approximation for non-unity couplings and for $g_{DM} \neq g_q$, provided
that the sample is rescaled to the appropriate cross section times
branching ratio.

While the simple scaling function

$$\sigma' \times BR' = [\sigma \times BR] \times \frac{g_q'^2}{g_q} \times \frac{g_{DM}'^2}{g_{DM}} \times \frac{\Gamma}{\Gamma'} \qquad (2.29)$$

is sufficient for a limited range of coupling values (see Fig. 2.34
for example), this scaling is only approximate (up to 20%) and

1003 relies on the narrow width approximation, ignoring PDFs effects.
1004 We also choose to provide instead a table of cross section times
1005 branching ratio values over a large range of couplings to support
1006 interpretation of search results (see the Appendix **??**). The table lists
1007 couplings from $g = 0.1$ to $g = 3.5$, where the upper limit is chosen
1008 to be close to but lower than the perturbative limit.
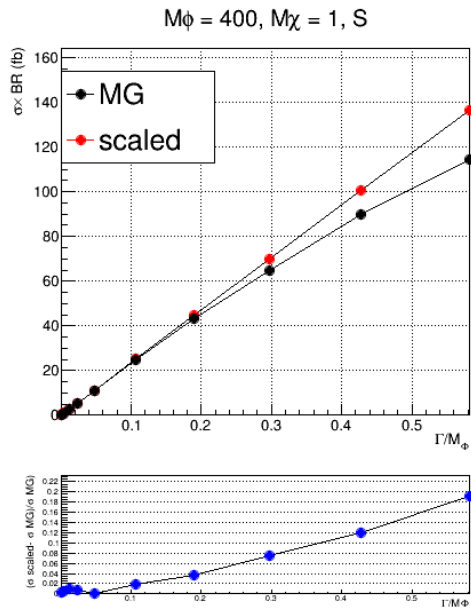
Figure 2.34: An example comparing a simple cross section scaling versus the computation from the generator, for a scalar model with $m_\phi = 400\,\mathrm{GeV}$, $m_{\mathrm{DM}} = 1\,\mathrm{GeV}$ and all couplings set to unity. In this example, the scaling relationship holds for Γ_ϕ/m_ϕ below 0.2, beyond which finite width effects become important and the simple scaling breaks down.

3

Specific models for signatures with EW bosons

In this Section, we consider specific models with a photon, a W boson, a Z boson or a Higgs boson in the final state ($V+\not{E}_T$ signature), accompanied by Dark Matter particles that either couple directly to the boson or are mediated by a new particle. The common feature of those models is that they provide different kinematic distributions with respect to the models described in Section 2.

The models considered in this Section can be divided into two categories:

V-specific simplified models These models postulate direct couplings of new mediators to bosons, e.g. they couple the Higgs boson to a new vector or to a new scalar [CDM$^+$14, BLW14].

Models including a contact operator, where the boson is directly coupled to DM Shown on the right-hand side of Figure 3.1, these models allow for a contact interaction vertex that directly couples the boson to Dark Matter [CHLR13, CNS$^+$13, CHH15, BLW14]. These models are included in this report devoted to simplified models since UV completions for most of these operators proceed through loops and are not available to date. These models provide a benchmark to motivate signal regions that are unique to searches with EW final states and would otherwise not be studied. However, we recommend to use these models as placeholders and emphasize model-independent results especially in signal regions tailored to these models. Wherever results are interpreted in terms of these operators, a truncation procedure to ensure the validity of the EFT should be employed, as detailed in the next Section (Sec. 4).

The following Sections describe the models within these categories, the parameters for each of the benchmark models chosen, the studies towards the choices of the parameters to be scanned.

3.1 *Specific simplified models including EW bosons, tailored to Higgs+MET searches*

Three benchmark simplified models [CDM$^+$14, BLW14] are recommended for Higgs+$\not{E}_T$ searches:

- A model where a leptophobic vector mediator (Z'_B) is exchanged in the $s-$channel, radiates a Higgs boson and decays into two DM particles (Fig. 3.2 (a));

- A model where a scalar mediator S couples to the SM only through the SM Higgs and decays to two DM particles (Fig. 3.3);

- A model where a vector Z' is produced resonantly and decays into a Higgs boson plus an intermediate heavy pseudoscalar particle A^0, in turn decaying into two DM particles (Fig. 3.2 (b)).
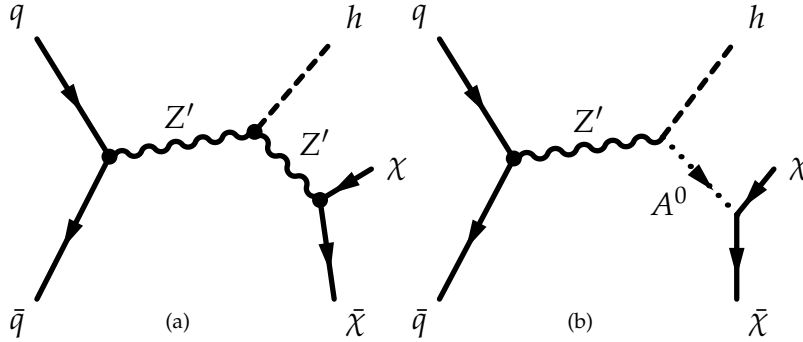
Figure 3.2: Feynman diagrams of leading order processes leading to Higgs+$\not{E}_T$ events: (a) a model with a vector mediator (Z') coupling with DM and with the Higgs boson h, and (b) a 2HDM model with a new invisibly decaying pseudoscalar A^0 from the decay of an on-shell resonance Z' giving rise to a Higgs+$\not{E}_T$ signature .

These models are kinematically distinct from one another, as shown in the comparison of the $\not{E}_T$ spectra in Fig. 3.4 for high and low masses of the pseudoscalar mediator. Figure 3.4 (a) shows the $\not{E}_T$ distribution for models with high mediator masses ($m_S = 1$ TeV, $m_{Z'} = 1$ TeV, $m_{A^0} = 1$ TeV) and DM mass of either 50 (Z'_B and A^0 models) or 65 GeV (scalar mediator model). Figure 3.4 (b) shows the $\not{E}_T$ distribution for models with low pseudoscalar mediator masses ($m_{Z'_B} = 100$ GeV, $m_{Z'} = 1$ TeV, $m_{A^0} = 100$ GeV) and DM mass of 1 TeV for all models.

3.1.1 $\not{E}_T$ +Higgs from a baryonic Z'

The model shown in Fig. 3.2 (a) postulates a new gauge boson Z' corresponding to a new $U(1)_B$ baryon number symmetry. The stable baryonic states included in this model are the DM candidate particles. The mass of the Z' boson is acquired through a baryonic Higgs h_B, which mixes with the SM Higgs boson. The interactions
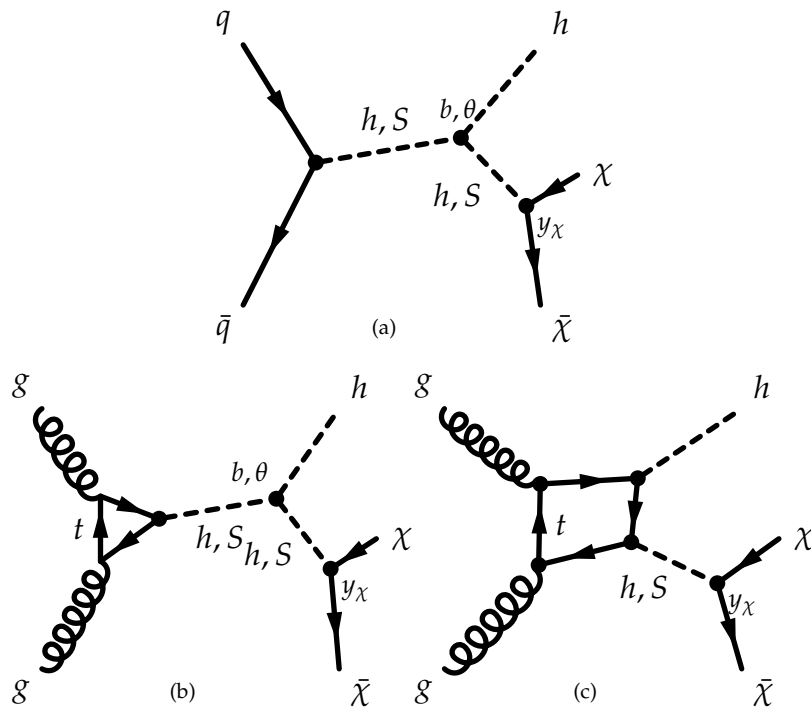
Figure 3.3: Feynman diagrams of leading order processes leading to Higgs+$\not{E}_T$ events for a model with a scalar mediator (S) coupling with DM and with the Higgs boson h.

(a) High mediator mass   (b) Low mediator mass
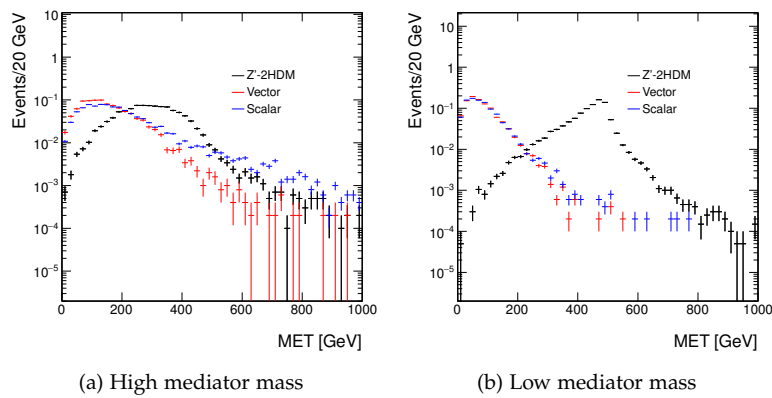
Figure 3.4: Comparison of the missing transverse momentum distributions at generator level in different simplified models leading to a Higgs+$\not{E}_T$ signature. The model parameter settings are detailed in the text.

between the Z', the quarks and the DM are described by the following Lagrangian:

$$L = g_q \bar{q} \gamma^\mu q Z'_\mu + g_{DM} \bar{\chi} \gamma^\mu \chi Z'_\mu. \tag{3.1}$$

The quark couplings g_q are fixed to be equal to one third of the gauge coupling g_B, while the DM coupling to the Z' are proportional to the baryon number and to the gauge coupling ($g_\chi = B g_B$). No leptonic couplings of the Z' are allowed, thus evading dilepton constraints. After incorporating the mixing of the baryonic and SM Higgs bosons, this model is is described by the following Lagrangian term at energies below $m_{Z'}$:

$$L_{eff} = -\frac{g_q g_{DM}}{m_{Z'}^2} \bar{q} \gamma^\mu q \bar{\chi} \gamma_\mu \chi \left(1 + \frac{g_{hZ'Z'}}{m_{Z'}^2} h\right), \tag{3.2}$$

The first term of this equation gives rise to a term that is equivalent to the radiation of a jet (or another EW gauge boson) in the initial state. The second term describes the interaction between the Z' and the SM Higgs boson, via the coupling $g_{hZ'Z'} = \frac{m_{Z'} 2 \sin\theta}{v_B}$, where $\sin\theta$ is the mixing angle between the SM Higgs and the baryonic Higgs h_B, and v_B is the Baryonic Higgs vacuum expectation value.

The predictions of the model depend upon the two additional parameters beyond an s-channel simplified model, namely the mixing angle between baryonic Higgs h_B and the SM-like Higgs boson $\sin\theta$ and the coupling of the mediator to SM-like Higgs boson, $g_{hZ'Z'}$. Thus, a full model is specified by: (M_{med}, m_{DM}, g_{DM}, g_q, $\sin\theta$, $g_{hZ'Z'}$).

3.1.1.1 Parameter scan

The width of the Z' mediator is calculated using all possible decays to SM particles (quarks) and to pairs of DM particles if kinematically allowed.

The dependence of the missing transverse momentum ($\not{E}_T$) on the model parameters is studied by varying the parameters one at a time. The variation of parameters other than M_{med} and m_{DM} does not result in significant variations of the $\not{E}_T$ spectrum, as shown in Figures 3.5. Figure 3.6 shows that for an on-shell mediator, varying m_{DM} with the other parameters fixed does not affect the $\not{E}_T$ distribution, while the distribution broadens significantly in the case of an off-shell mediator. For this reason, the same grid in M_{med}, m_{DM} as for the vector mediator of the jet+$\not{E}_T$ search (Table 2.1) is chosen as a starting point. The coupling $g_{hZ'Z'}$, along with g_q and g_{DM}, are subject to perturbativity bounds:

$$g_q, g_{DM} < 4\pi$$

and

$$g_{hZ'Z'} < \sqrt{4\pi} m_{Z'} \sin\theta$$

The value $g_{hZ'Z'}/m_{Z'} = 1$ is chosen as a benchmark value for the generation of Monte Carlo samples since it maximizes the cross section (as shown in the following paragraph) without violating

1094 the bounds. The mediator-DM coupling g_{DM} is fixed to 1, and the
1095 mediator-quark g_q coupling is fixed to $1/3$. The kinematic distri-
1096 butions do not change as a function of these parameters, so results
1097 for other values of $g_{hZ'Z'}/m_{Z'}$, g_{DM} and g_q can be obtained through
1098 rescaling by the appropriate cross sections.

1099   Figs 3.7 and 3.8 show the kinematic distributions for the two
1100 leading jets in the $H \rightarrow \bar{b}b$ decay channel, for two values of the
1101 mediator mass and varying the DM mass.

1102   Analyses should perform further studies, beyond those studies
1103 performed for the forum, to estimate the reach of the analysis with
1104 respect to all points in the grid and therefore decide on a smaller
1105 set of grid points to be generated.
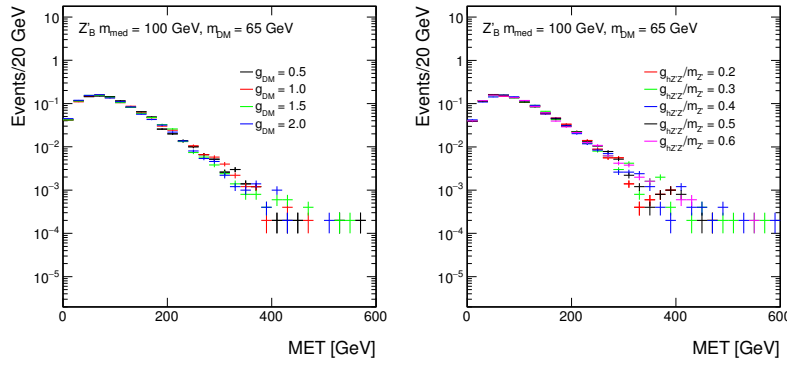
Figure 3.5: Missing transverse momentum distributions at generator level in the vector mediator scenario for different values of: the mediator-dark matter coupling g_{DM} (left), and the coupling between the mediator and the SM-like Higgs boson, scaled by the mediator mass, $g_{hZ'Z'}/m_{Z'}$ (right).
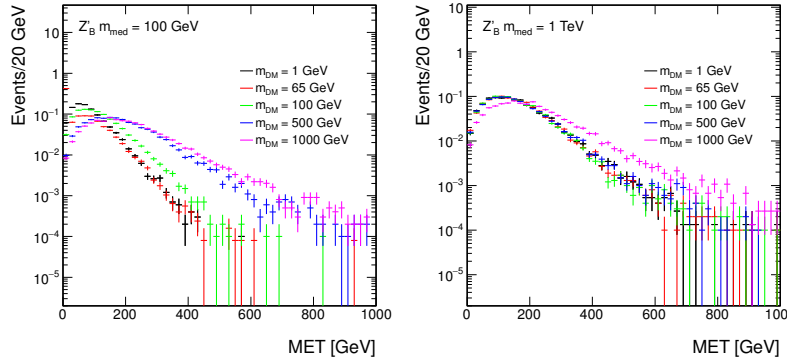
Figure 3.6: Missing transverse momentum distributions at generator level in the vector mediator scenario: for different values of the dark matter mass m_{DM} and a mediator mass of M_{med} = 100 GeV (left) and M_{med} = 1 TeV (right).

1106 ### 3.1.1.2   *Cross-section scaling*

The dependence of the cross section of the $pp \rightarrow H\chi\bar{\chi} + X$ process
on $g_{hZ'Z'}$ is shown in Figure 3.9. The curves have been fit to second-
order polynomials. For $m_{med} = 100$ GeV, the fit function is

$$y = -0.12 - 3.4 \times 10^{-3}x + 2.7 \times 10^{-4}x^2$$

. For $m_{med} = 1$ TeV, the fit function is is

$$y = 0.0012 - 2.4 \times 10^{-7}x + 1.5 \times 10^{-7}x^2$$

$$y = -0.12 - 3.4 \times 10^{-3}x + 2.7 \times 10^{-4}x^2. \tag{3.3}$$
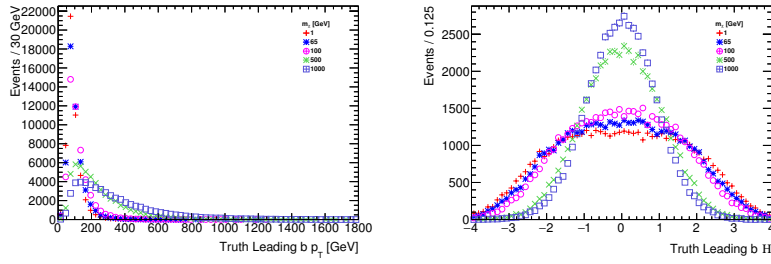
(a) Leading b−jet transverse momentum
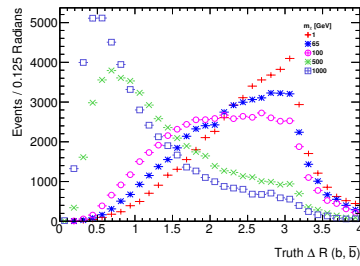
(b) Leading b−jet pseudorapidity

(c) Angular distance between the two leading b−jets

Figure 3.7: Comparison of the kinematic distributions for the two leading b−jets (from the Higgs decay) in the vector Z' simplified model, when fixing the Z' mass to 100 GeV and varying the DM mass.
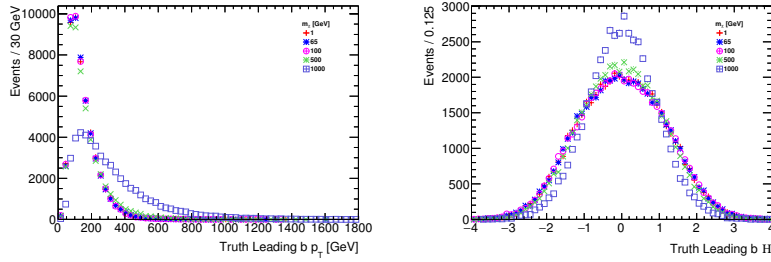
(a) Leading b−jet transverse momentum

(b) Leading b−jet pseudorapidity
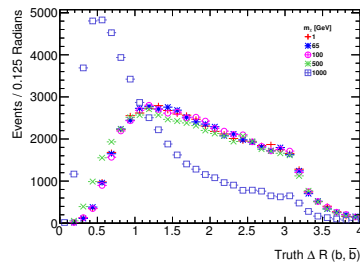
(c) Angular separation of the two leading b-jets

Figure 3.8: Comparison of the kinematic distributions for the two leading jets from the Higgs decay in the vector Z' simplified model, when fixing the Z' mass to 1000 GeV and varying the DM mass.

1107   For $M_{\text{med}} = 1$ TeV, the fit function is is:

$$y = 0.0012 - 2.4 \times 10^{-7}x + 1.5 \times 10^{-7}x^2. \qquad (3.4)$$
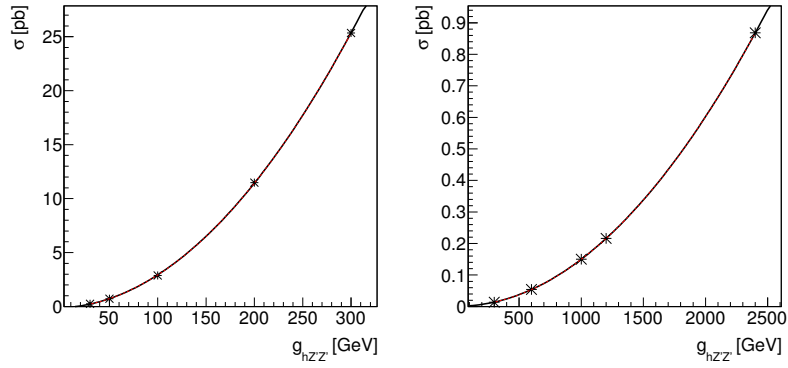
Figure 3.9: Cross section of the $pp \rightarrow H\chi\bar{\chi}$ process as a function of $g_{hZ'Z'}$ for $m_{Z'} = 100$ GeV (left) and $m_{Z'} = 1$ TeV (right). The fit functions are shown in the text.

3.1.2 $\not{E}_T$ +Higgs from a scalar mediator

A real scalar singlet *S* coupling to DM can be introduced as a portal between SM and the dark sector through the Higgs field. The new scalar mixes with the SM Higgs boson, and couples to DM through a Yukawa term y_χ. The relevant terms in the scalar potential are:

$$V \supset a|H|^2 S + b|H|^2 S^2 + \lambda_h |H|^4$$
$$\longrightarrow \tfrac{1}{2}a(h+v)^2 S + \tfrac{1}{2}b(h+v)^2 S^2 + \frac{\lambda_h}{4}(h+v)^4, \qquad (3.5)$$

where a, b are new physics couplings and λ_h is the Higgs quartic coupling.

The additional Lagrangian terms for this model are:

$$L \supset -y_\chi \bar{\chi}\chi(\cos\theta\, S - \sin\theta\, h) - \frac{m_q}{v}\bar{q}q(\cos\theta\, h + \sin\theta\, S) \qquad (3.6)$$

where θ is the mixing angle between the Higgs boson and the new scalar.

Mono-Higgs signals in this second model arise through processes shown in Fig. 3.3 (a,b), or through the radiation of a Higgs boson from the *t* quark in the production loop, in Fig. 3.3 (c). The first two processes depend on the $h^2 S$ and hS^2 cubic terms in Eq. (3.5). At leading order in $\sin\theta$, these terms are:

$$V_{\text{cubic}} \approx \frac{\sin\theta}{v}(2m_h^2 + m_S^2)h^2 S + b\, v\, h\, S^2 + ... \qquad (3.7)$$

with a and λ_h expressed in terms of $\sin\theta$ and m_h^2, respectively. At leading order of $\sin\theta$, the $h^2 S$ term is fixed once the mass eigenvalues m_h, m_S and mixing angle are specified. The $h S^2$ term is not fixed and remains a free parameter of the model, depending on the new physics coupling b.

3.1.2.1   *Parameter scan*

The model is described by five parameters:

1. the Yukawa coupling of heavy scalar to dark matter, g_{DM} (also referred to as y_χ)

2. the mixing angle between heavy scalar and SM-like Higgs boson, $\sin\theta$;

3. the new physics coupling, b;

4. mass of heavy scalar, m_S, also termed M_{med};

5. mass of dark matter, m_{DM};

The mixing angle is constrained from current Higgs data to satisfy $\cos\theta = 1$ within 10% and therefore $\sin\theta \lesssim 0.4$. This provides a

starting point for the parameter scan in this model: we recommend
to set $\sin\theta = 0.3$. Figure 3.11 shows that there is no dependence
of the kinematics from the value of this angle, and different values
can be obtained via rescaling the results for this mixing angle ac-
cording to the relevant cross-section. It can also be observed from
Figures 3.12 and 3.10 that the kinematics of this model follows that
of the equivalent jet+$\not{E}_T$ model: only small changes are observed in
the on-shell region, while the relevant distributions diverge when
the mediator is off-shell. For this reason, the same grid in M_{med},
m_{DM} as for the scalar mediator of the jet+$\not{E}_T$ search (Table 2.3) is
chosen as a starting point. The Yukawa coupling to DM y_{DM} is
set to 1, the new physics coupling between scalar and SM Higgs b
= 3. Results for other values can be obtained via a rescaling of the
results for these parameters.

To do **Estimate the sensitivity and possibly prune parameter scan. (??)**
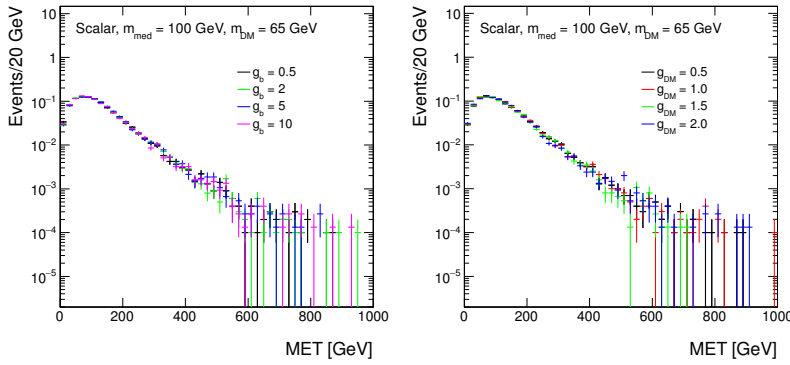
Figure 3.10: Missing transverse momentum distributions at generator level in the scalar mediator scenario, for different values of: the new physics coupling g_b (left), and the mediator-dark matter coupling g_{DM} (right).
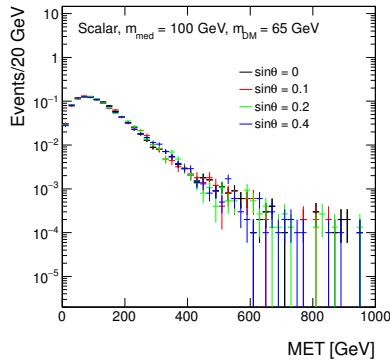
Figure 3.11: Missing transverse momentum distributions at generator level in the scalar mediator scenario: for different values of the mixing angle $\sin\theta$.

Figs. 3.13 and 3.14 show the kinematic distributions for the two
leading jets in the $H \to \bar{b}b$ decay channel, for two values of the
mediator mass and varying the DM mass.

3.1.3 Higgs+$\not{E}_T$ signal from 2HDM model with a Z' and a new pseudoscalar

In this simplified model [BLW14], a new Z' resonance decays to a
Higgs boson h plus a heavy pseudoscalar state A^0 in the 2HDM
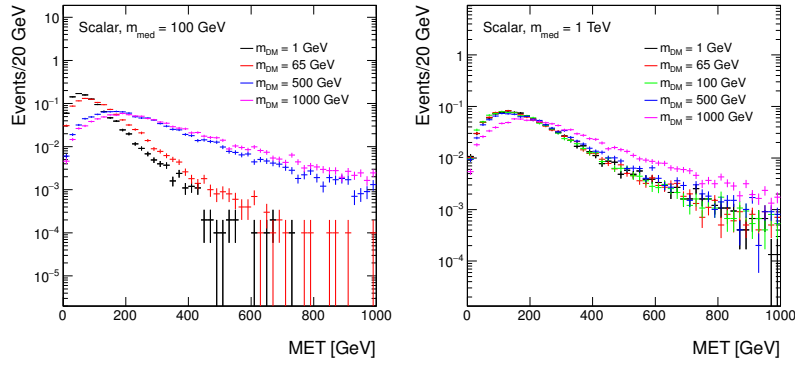
Figure 3.12: Missing transverse momentum distributions at generator level in the scalar mediator scenario: for different values of the dark matter mass m_{DM} and a mediator mass of $M_{med} = 100$ GeV (left) and $M_{med} = 1$ TeV (right).

(a) Leading $b-$jet transverse momentum

(b) Leading $b-$jet pseudorapidity

(c) Angular distance between the two leading $b-$jets
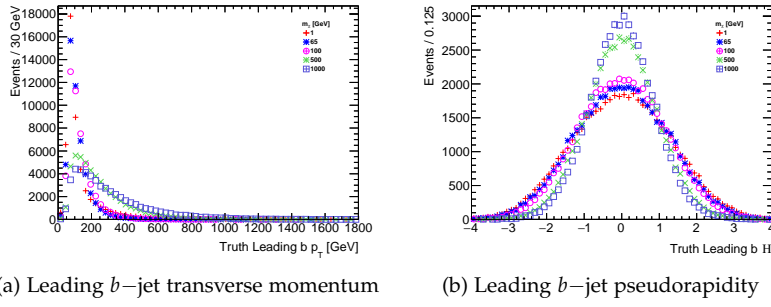
Figure 3.13: Comparison of the kinematic distributions for the two leading jets from the Higgs decay in the scalar simplified model, when fixing the new scalar mass to 100 GeV and varying the DM mass.
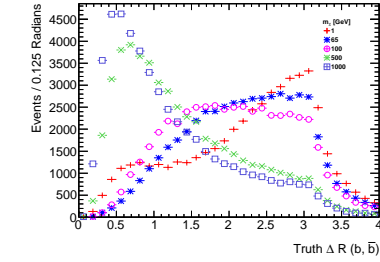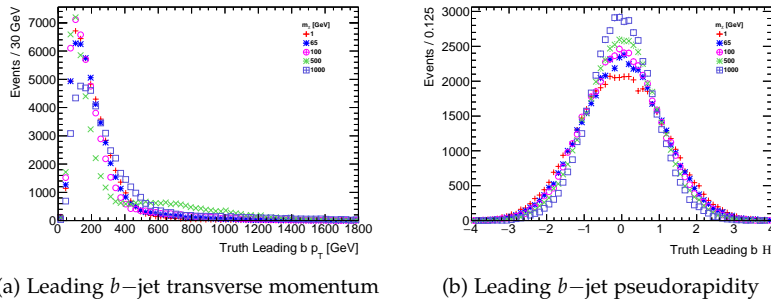
(a) Leading $b-$jet transverse momentum

(b) Leading $b-$jet pseudorapidity
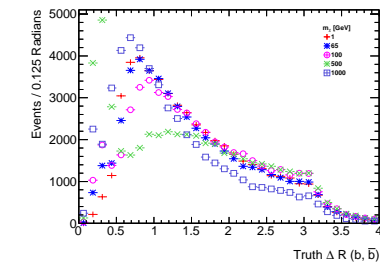
(c) Angular distance between the two leading $b-$jets

Figure 3.14: Comparison of the kinematic distributions for the two leading jets from the Higgs decay in the scalar simplified model, when fixing the new scalar mass to 1000 GeV and varying the DM mass.

framework, which in turn decays to a DM pair. This model is represented in the diagram in Fig. 3.2 (b).

The motivation for coupling the dark matter to the pseudoscalar is that dark matter coupling to a Higgs or Z' boson is generically constrained by other signal channels and direct detection. A reason to consider this model is that it has different kinematics due to the on-shell Z' production, where for heavy Z' masses the $\not{E}_T$ and p_T spectra are much harder. This model can satisfy electroweak precision tests and constraints from dijet resonance searches, and still give a potentially observable Higgs+$\not{E}_T$ signal.

This model comprises two doublets, where Φ_u couples to up-type quarks and Φ_d couples to down-type quarks and leptons:

$$-\mathcal{L} \supset y_u Q \tilde{\Phi}_u \bar{u} + y_d Q \Phi_d \bar{d} + y_e L \Phi_d \bar{e} + \text{h.c.} \tag{3.8}$$

After electroweak symmetry breaking, the Higgs doublets attain vacuum expectation values v_u and v_d, and in unitary gauge the doublets are parametrized as

$$\Phi_d = \frac{1}{\sqrt{2}} \begin{pmatrix} -\sin\beta \, H^+ \\ v_d - \sin\alpha \, h + \cos\alpha \, H - i\sin\beta \, A^0 \end{pmatrix} \, ,$$

$$\Phi_u = \frac{1}{\sqrt{2}} \begin{pmatrix} \cos\beta \, H^+ \\ v_u + \cos\alpha \, h + \sin\alpha \, H + i\cos\beta \, A^0 \end{pmatrix} \tag{3.9}$$

where h, H are neutral CP-even scalars and A^0 is a neutral CP-odd scalar. In this framework, $\tan\beta \equiv v_u/v_d$, and α is the mixing angle that diagonalizes the $h - H$ mass squared matrix. We take $\alpha = \beta - \pi/2$, in the limit where h has SM-like couplings to fermions and gauge bosons as per Ref. [CGT13], and $\tan\beta \geq 0.3$ as implied from the perturbativity of the top Yukawa coupling. The Higgs vacuum expectation values lead to $Z - Z'$ mass mixing, with a mixing parameter given by

$$\begin{aligned} \epsilon &\equiv \frac{1}{M_{Z'}^2 - M_Z^2} \frac{g g_z}{2\cos\theta_w} (z_d v_d^2 + z_u v_u^2) \\ &= \frac{(M_Z^0)^2}{M_{Z'}^2 - M_Z^2} \frac{2 g_z \cos\theta_w}{g} z_u \sin^2\beta. \end{aligned} \tag{3.10}$$

The production cross section for this model scales as $(g_z)^2$, as the decay width for this process to leading order in ϵ (Eq. 3.10) is

$$\Gamma_{Z' \to h A^0} = (g_z \cos\alpha \cos\beta)^2 \frac{|p|}{24\pi} \frac{|p|^2}{M_{Z'}^2}. \tag{3.11}$$

where the center of mass momentum for the decay products $|p| = \frac{1}{2M_{Z'}} \sqrt{(M_{Z'}^2 - (m_h + m_{A^0})^2)(M_{Z'}^2 - (m_h - m_{A^0})^2)}$.

3.1.3.1 Parameter scan

The model is described by five parameters:

- the pseudoscalar mass M_{A^0},

- the DM mass m_{DM},

- the Z' mass, $M_{Z'}$,

- $\tan\beta (\equiv v_u/v_d)$,

- the Z' coupling strength g_z.

To study the signal production and kinematic dependencies on these parameters, we produced signal samples varying each of the five parameters through MadGraph5_aMC@NLO for the matrix element, PYTHIA for the parton shower, and DELPHES[dF⁺14] for a parameterized detector-level simulation.

As seen in Fig. 3.15, variations of $\tan\beta$ does not lead to any kinematic difference and the production cross section simply scales as a function of $\tan\beta$. Hence we recommend to fix $\tan\beta$ to unity in the signal generation.
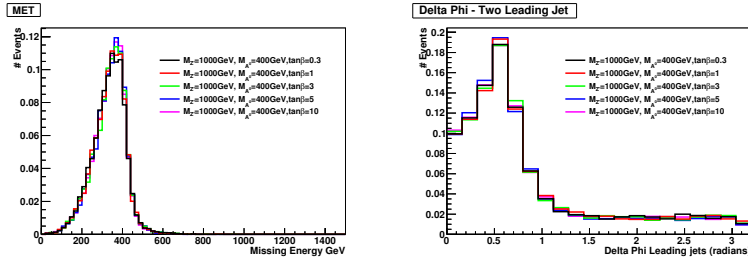
(a) $\not{E}_T$ distribution   (b) $\Delta\phi$ distance between the two $b-$ jets

Figure 3.15: Kinematic distributions of the signal process varying $\tan\beta$, in the case of a Higgs boson decaying into two b quarks, after parameterized detector simulation: no kinematic dependency is observed

Similarly, variations of g_z do not lead to any kinematic changes. The value of g_z for a given $M_{Z'}$ and $\tan\beta$ can be set according to the maximum value allowed by electroweak global fits and dijet constraints, as described in [BLW14]. Since this parameter does not influence the kinematics, we leave it up to individual analyses on whether they generate benchmark points only according to these external constraints.

Since the DM pair are produced as a result of the decay of A^0, there are minimal kinematic changes when varying m_{DM} as long as $m_{\mathrm{DM}} < M_{A^0}/2$ so that A^0 production is on-shell, as shown in Fig. 3.16 and 3.17 (before detector simulation).
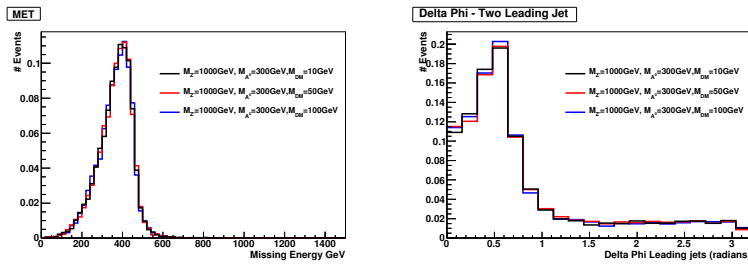
(a) $\not{E}_T$ distribution   (b) $\Delta\phi$ distance between the two $b-$ jets

Figure 3.16: Kinematic distributions of the signal process varying m_{DM}: minimal kinematic dependency on m_{DM} as expected when A^0 is produced on-shell. Plots shown for $M_{Z'} = 1000$ GeV, $M_{A^0} = 300$ GeV.

We recommend to produce signal events for a fixed $g_z = 0.8$, $\tan\beta = 1$ and $m_{\mathrm{DM}} = 100$ GeV. For these values, we scan the 2-D parameter space of $M_{Z'}, M_{A^0}$ with $M_{Z'} = 600, 800, 1000, 1200, 1400$ GeV, and $M_{A^0} = 300, 400, 500, 600, 700, 800$ GeV with $M_{A^0} < M_{Z'} - m_h$,
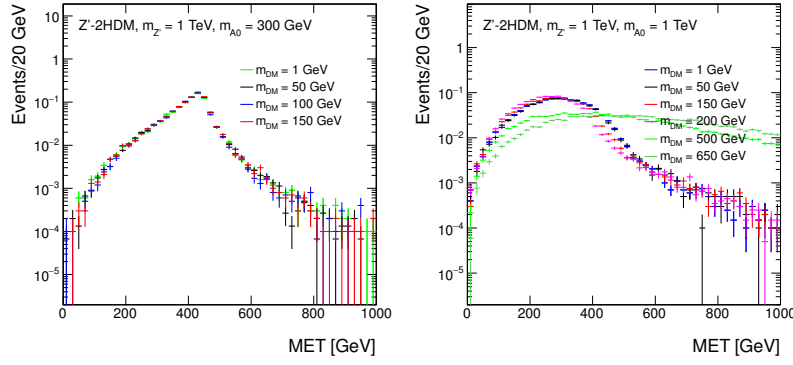
Figure 3.17: Missing transverse momentum distributions at generator level in the Z' +2HDM scenario for different values of the dark matter mass m_{DM}, with $m_{Z'} = 1$ TeV and $m_{A0} = 300$ GeV (left) and $m_{A0} = 1$ TeV (right).

for a total of 24 points. The choice of scan is justified by the sensitivity study in [BLW14]: the expected LHC sensitivity for Run-2 is up to $M_{Z'} \sim 1.5$ TeV. For the parameter scan, the DM mass is fixed to 100 GeV. For two $M_{Z'}$, M_{A^0} value sets, we vary the DM mass to obtain sample cross section for rescaling results. All LO cross sections for the various parameter scan points are reported in Appendix B. The parameter scan excludes the off-shell region, as the cross-sections are suppressed and the LHC would not have any sensitivity to these benchmark points in early data.

The kinematic distributions with varying $M_{Z'}$ for fixed M_{A^0} are shown in Fig. 3.18, while the dependency on M_{A^0} is shown in Fig. 3.19.

(a) $\not{E}_T$ distribution

(b) Leading $b-$jet p_T distribution

(c) $\Delta\phi$ distance between the two $b-$ jets

(d) Dijet invariant mass
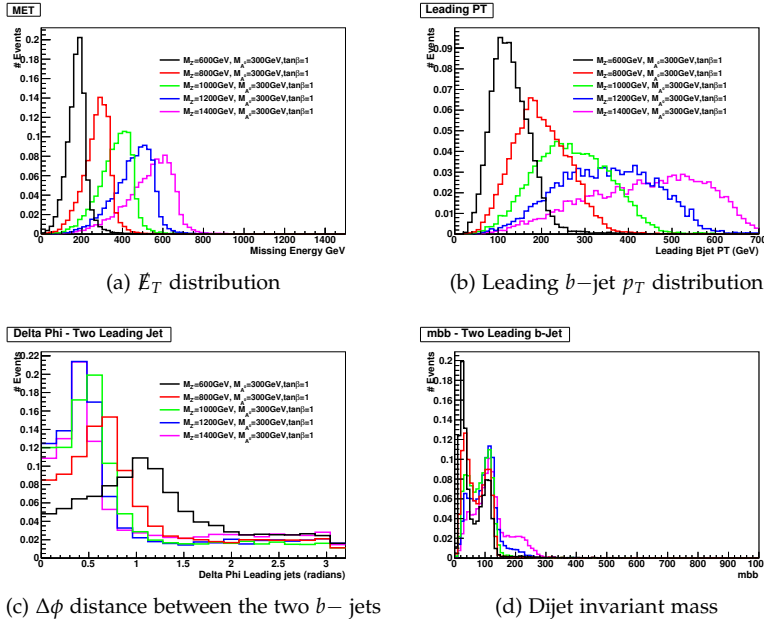
Figure 3.18: Kinematic distributions of the signal process varying $M_{Z'}$, for $m_{DM} = 100$ GeV, $M_{A^0} = 300$ GeV.

This model also allows for an additional source of Higgs plus $\not{E}_T$ signal with a similar kinematics (Fig. 3.20, shown with detector simulation samples) to the signal process from the decay of $Z' \rightarrow hZ$, where the Z decays invisibly. The partial decay width for the Z'

(a) $\not{E}_T$ distribution

(b) Leading $b-$jet p_T distribution

(c) $\Delta\phi$ distance between the two $b-$ jets

(d) Dijet invariant mass
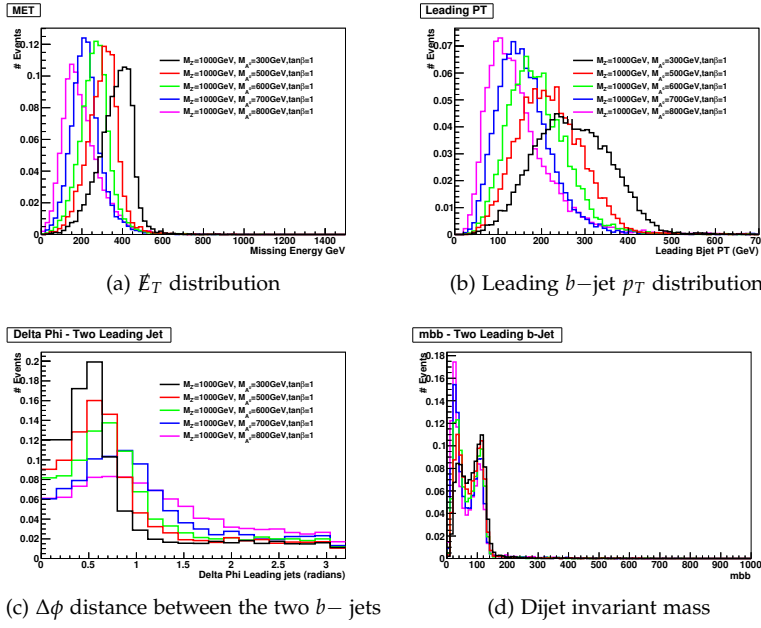
Figure 3.19: Kinematic distributions of the signal process varying M_{A^0}, for $m_{DM} = 100$ GeV, $M_{Z'} = 1000$ GeV.

is:

$$\Gamma_{Z'\to hZ} = (g_z \cos\alpha \sin\beta)^2 \frac{|p|}{24\pi} \left(\frac{|p|^2}{M_{Z'}^2} + 3\frac{M_Z^2}{M_{Z'}^2} \right), \qquad (3.12)$$

The values for the Z' masses scanned for those samples should follow those of the previous samples, namely values of $M_{Z'} = 600, 800, 1000, 1200, 1400$ GeV. This signal process has no M_A dependence.

(a) $\not{E}_T$ distribution

(b) Leading $b-$jet p_T distribution

(c) $\Delta\phi$ distance between the two $b-$ jets

(d) Dijet invariant mass
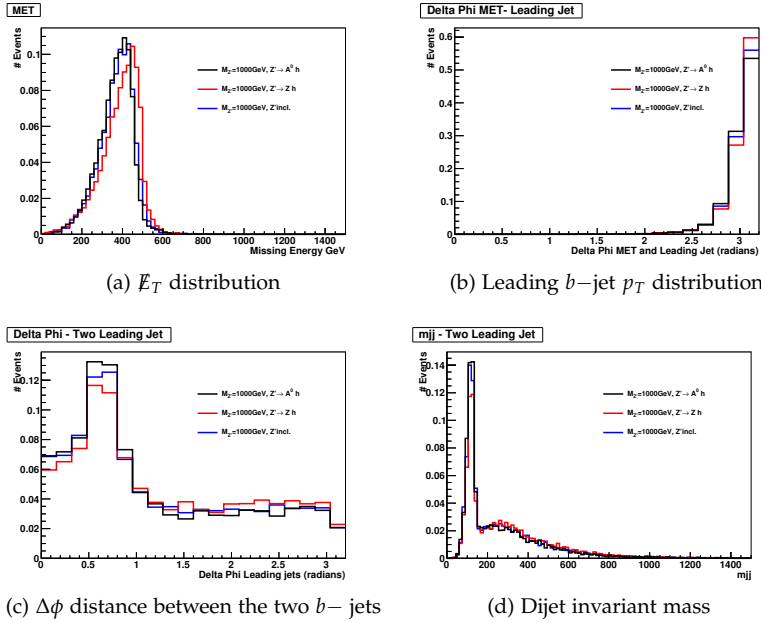
Figure 3.20: Kinematic distributions of $Z' \to A^0 h$ exclusive production, $Z' \to Zh$ exclusive production and Z' inclusive production for $M_{Z'} = 1000$ GeV and $M_{A^0} = 300$ GeV

IMPLEMENTATION DISCUSSED IN THE APPENDIX

3.2 EFT models with direct DM-boson couplings

The EFT operators considered in this section do not have a simplified model completion for Dirac fermion Dark Matter available to date. They provide kinematic distributions that are unique to mono-boson signatures, and that in most cases are not reproduced by an equivalent simplified model [1].

A complete list of effective operators with direct DM/boson couplings for Dirac DM, up to dimension 7, can be found in [CHLR13, CNS$^+$13, CHH15]. Higher dimensional operators, up to dimension 8, leading to Higgs+$\not{E}_T$ signatures, are mentioned in [CNS$^+$13, BLW14]. The first part of this Section outlines the main characteristics for a limited number of these models that could be considered in Run-2 searches. In the spirit of the Forum consensus to privilege simplified models, model-independent results as in Appendix C should be privileged over considering these operators as realistic benchmarks. We also recommend not to optimize searches based on those benchmark models.

However, another consideration that emerged from the Forum discussion was that the EFT approach allows more model-independence when reinterpreting results, making it worth still having results available in terms of these operators. Furthermore, once simplified models are available for those operators, EFT results can be used as a limiting case for consistency checks. We devote the end of this Section to provide a recommendation on how to present the results from this model, including an assessment of their validity using a conservative procedure that is only dependent on EFT parameters.

3.2.1 Dimension 5 operators

The lowest dimension benchmark operators we consider are effective dimension 5, such as the one depicted in Figure 3.21.

Following the notation of [CNS$^+$13], models from this category have a Lagrangian that includes terms such as:

$$\frac{m_W^2}{\Lambda_5^3}\, \bar{\chi}\chi\, W^{+\mu}W_\mu^- + \frac{m_Z^2}{2\Lambda_5^3}\, \bar{\chi}\chi\, Z^\mu Z_\mu \,, \qquad (3.13)$$

where m_Z and m_W are the masses of the Z and W boson, W^μ and Z^μ are the fields of the gauge bosons, χ denote the Dark Matter

[1] Wherever this is the case, we recommend only generation of simplified model result as that can be reinterpreted.
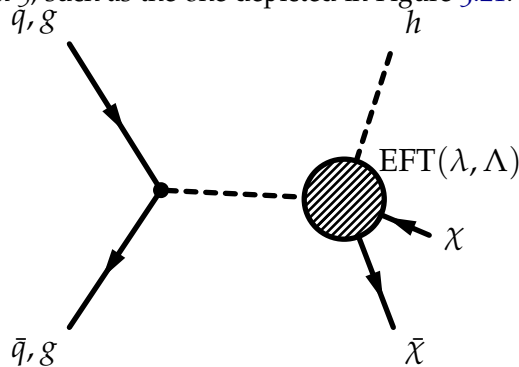
Figure 3.21: Diagram for EFT operators giving rise to a Higgs+$\not{E}_T$ signature.

fields and Λ_5 is the effective field theory scale . Note that these operators are of true dimension 7, but reduce to effective dimension 5 once the Higgs vacuum expectation values, contained in the W and Z mass terms, are inserted. As such, one expects these that operators would naturally arise in UV complete models where Dark Matter interacts via a Higgs portal where heavy mediators would couple to the Higgs or other fields in an extended Higgs sector. In such models the full theory may be expected to contain additional operators with Higgs-Dark Matter couplings [DFMQ13].

Concentrating for the moment on mono-gauge boson signals, the above operator induces signatures with $\not{E}_T$ in conjunction with Z and W bosons at tree level, while at loop level it induces couplings to photon pairs and $Z\gamma$ through W loops. In these models, a clear relation exists between final states with photons, EW bosons and Higgs boson.

As shown in Fig. 3.22 kinematics of this model can be approximated by that of a simplified model including a high-mass scalar mediator exchanged in the s-channel described in Section 2.2.2. For this reason, the list of benchmark models with direct boson-DM couplings for photon, Z and W only includes dimension 7 operators: the scalar model with initial state radiation of an EW boson is already recommended and its results can be rescaled.

The Higgs+$\not{E}_T$ analysis, however, will not consider the scalar simplified model as benchmark, due to the very low sensitivity in early LHC analyses, and will instead use this dimension 5 operator.
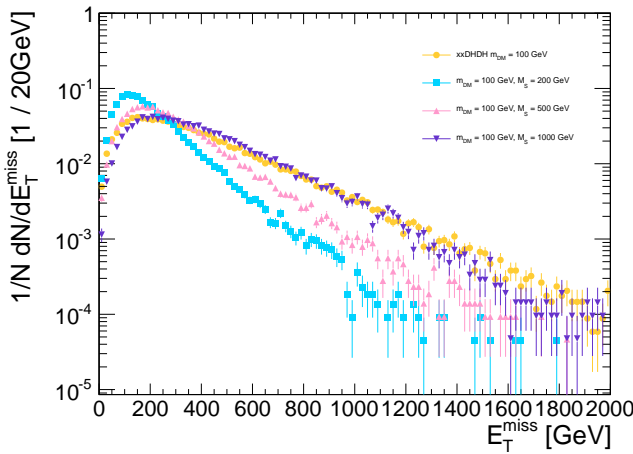
Figure 3.22: Comparison of the missing transverse momentum for the simplified model where a scalar mediator is exchanged in the s-channel and the model including a dimension-5 scalar contact operator, in the leptonic Z+$\not{E}_T$ final state

3.2.1.1 *Parameter scan*

The two parameters of this model are the scale of new physics λ and the DM particle mass. SM-DM coupling and new physics scale are related by $g_{DM} = (246 \text{ GeV})/\lambda$. .

The initial value of the new physics scale λ chosen for the sample generation is 3 TeV; this is a convention and does not affect the signal kinematics; the cross-section of the samples can be rescaled according to the λ^3 dependence when deriving the constraints on

1299   this scale. However, more care should be given when rescaling
1300   Higgs+$\not{E}_T$ operators of higher dimensions, as different diagrams
1301   have a different λ dependence.

     The DM mass values for the benchmark points to be simulated are chosen to span a sufficient Dark Matter range leading to different kinematics, that is within the LHC sensitivity for early searches and that is consistent across the various signatures and EFT operators. We therefore start the mass scan at m_{DM} =1 GeV, where collider experiments are complementary to direct and indirect detection and choose the last point corresponding to a DM mass of 1 TeV. We recommend a scan in seven mass points, namely:

$$m_{\mathrm{DM}} = 1, 10, 50, 100, 200, 400, 800, 1300\,\mathrm{GeV}.$$

1302   A set of kinematic distributions from the Higgs+$\not{E}_T$ signature
1303   where the Higgs decays into two $b-$quarks is shown in Fig. 3.23,
1304   for points similar to those of the grid scan proposed.
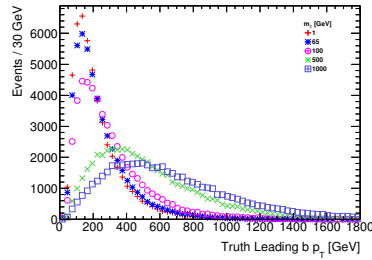
(a) Leading $b-$jet transverse momentum
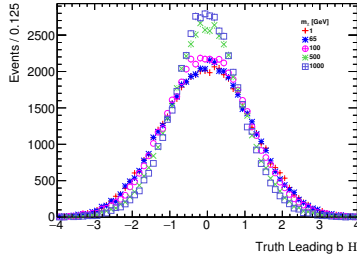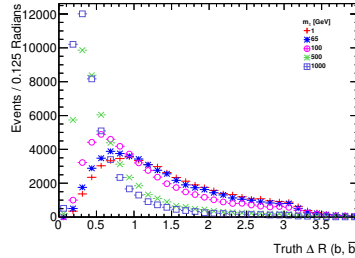
Figure 3.23: Comparison of the kinematic distributions for the two leading $b-$ jets (from the Higgs decay) in the model with direct interactions between the Higgs boson and the DM particle, when varying the DM mass.

(b) Leading $b-$jet pseudorapidity

(c) Angular distance between the two leading $b-$jets

1305   ### 3.2.2   *Dimension 7 operators*

The dimension-7 benchmark models contain the $SU(2)_L \times U(1)_Y$ gauge-invariant couplings between DM fields and the kinetic terms of the EW bosons. The CP-conserving scalar couplings of this type can be written as

$$\frac{c_1}{\Lambda_S^3}\,\bar{\chi}\chi\,B_{\mu\nu}B^{\mu\nu} + \frac{c_2}{\Lambda_S^3}\,\bar{\chi}\chi\,W^i_{\mu\nu}W^{i,\mu\nu}\,. \qquad (3.14)$$

Here $B_{\mu\nu} = \partial_\mu B_\nu - \partial_\nu B_\mu$ and $W^i_{\mu\nu} = \partial_\mu W^i_\nu - \partial_\nu W^i_\mu + g_2\epsilon^{ijk}W^j_\mu W^k_\mu$ are the $U(1)_Y$ and $SU(2)_L$ field strength tensor, respectively, and g_2 denotes the weak coupling constant. In the case of the pseudoscalar couplings, one has instead

$$\frac{c_1}{\Lambda_P^3}\,\bar{\chi}\gamma_5\chi\,B_{\mu\nu}\tilde{B}^{\mu\nu} + \frac{c_2}{\Lambda_P^3}\,\bar{\chi}\gamma_5\chi\,W^i_{\mu\nu}\tilde{W}^{i,\mu\nu}\,, \qquad (3.15)$$

where $\tilde{B}_{\mu\nu} = 1/2\, \epsilon_{\mu\nu\lambda\rho} B^{\lambda\rho}$ and $\tilde{W}^i_{\mu\nu} = 1/2\, \epsilon_{\mu\nu\lambda\rho} W^{i,\lambda\rho}$ are the dual field strength tensors. In addition to the CP-conserving interactions (3.14) and (3.15), there are also four CP-violating couplings that are obtained from the above operators by the replacement $\bar{\chi}\chi \leftrightarrow \bar{\chi}\gamma_5\chi$.

The effective interactions introduced in (3.14) and (3.15) appear in models of Rayleigh DM [WY12]. Ultraviolet completions where the operators are generated through loops of states charged under $U(1)_Y$ and/or $SU(2)_L$ have been proposed in [WY13] and their LHC signatures have been studied in [LSWY13]. If these new charged particles are light, the high-p_T gauge bosons that participate in the $\cancel{E}_T$ processes considered here are able to resolve the substructure of the loops. This generically suppresses the cross sections compared to the EFT predictions [HKU13], and thus will weaken the bounds on the interaction strengths of DM and the EW gauge bosons to some extent. Furthermore, the light charged mediators may be produced on-shell in pp collisions, rendering direct LHC searches potentially more restrictive than $\cancel{E}_T$ searches. Making the above statements precise would require further studies beyond the timescale of this forum.

Since for $\Lambda_S = \Lambda_P$ the effective interactions (3.14) and (3.15) predict essentially the same value of the mono-photon, mono-Z and mono-W cross section [CNS$^+$13, CHH15], we consider below only the former couplings. We emphasize however that measurements of the jet-jet azimuthal angle difference in $\cancel{E}_T + 2j$ events may be used to disentangle whether DM couples more strongly to the combination $B_{\mu\nu}B^{\mu\nu}$ ($W^i_{\mu\nu}W^{i,\mu\nu}$) or the product $B_{\mu\nu}\tilde{B}^{\mu\nu}$ ($W^i_{\mu\nu}\tilde{W}^{i,\mu\nu}$) of field strength tensors [CHLR13, CHH15].

After EW symmetry breaking the interactions (3.14) induce direct couplings between pairs of DM particles and gauge bosons. The corresponding Feynman rule reads:

$$\frac{4i}{\Lambda_S^3}\, g_{V_1 V_2} \left(p_1^{\mu_2} p_2^{\mu_1} - g^{\mu_1 \mu_2}\, p_1 \cdot p_2 \right), \qquad (3.16)$$

where p_i (μ_i) denotes the momentum (Lorentz index) of the vector field V_i and for simplicity the spinors associated with the DM fields have been dropped. The couplings $g_{V_i V_j}$ take the form:

$$
\begin{aligned}
g_{\gamma\gamma} &= c_w^2 c_1 + s_w^2 c_2\,, \\
g_{\gamma Z} &= -s_w c_w \left(c_1 - c_2 \right), \\
g_{ZZ} &= s_w^2 c_1 + c_w^2 c_2\,, \\
g_{WW} &= c_2\,,
\end{aligned}
\qquad (3.17)
$$

with s_w (c_w) the sine (cosine) of the weak mixing angle. Note that our coefficients c_1 and c_2 are identical to the coefficients C_B and C_W used in [CHH15], while they are related via $k_1 = c_w^2 c_1$ and $k_2 = s_w^2 c_2$ to the coefficients k_1 and k_2 introduced in [CNS$^+$13].

The coefficients c_1 and c_2 appearing in (3.17) determine the relative importance of each of the $\cancel{E}_T$ channels and their correlations. For example, one observes that:

- Only c_2 enters the coupling between DM and W bosons, meaning that only models with $c_2 \neq 0$ predict a mono-W signal;

- If $c_1 = c_2$ the mono-photon (mono-Z) signal does not receive contributions from diagrams involving Z (photon) exchange;

- Since numerically $c_w^2/s_w^2 \simeq 3.3$ the mono-photon channel is particularly sensitive to c_1.

3.2.2.1 Parameter scan

As stated above and shown in Ref. [NCC$^+$14], the kinematic distributions for dimension-7 scalar and pseudoscalar operators only shows small differences. This has been verified from a generator-level study: the signal acceptance after a simplified analysis selection ($\not{E}_T >$350 GeV, leading jet $p_T > 40$ GeV, minimum azimuthal difference between either of the two jets and the $\not{E}_T$ direction > 0.4) is roughly 70% for both. We therefore only suggest to generate one of the two models.

The differences in kinematics for the various signatures are negligible when changing the coefficients c_1 and c_2, since these coefficient factorize in the matrix element. Only the case $c_1 = c_2 = 1$ is generated as benchmark; other cases are left for reinterpretation as they will only need a rescaling of the cross-sections.

3.2.3 Higher dimensional operators

Many higher dimensional operators can induce signals of photons or $W/Z/H$ bosons in the final state. A complete list can be found in Refs. [CDM$^+$14, BLW14, PS14] and references therein.

Although with lower priority with respect to the operators above, a representative dimension-8 operators can be chosen as benchmark, with the form:

$$\frac{1}{\Lambda^4}\bar{\chi}\gamma^\mu\chi B_{\mu\nu}H^\dagger D^\nu H$$

In this case, the new physics scale is Λ is connected with the coupling of the DM as $y_\chi = \frac{1}{\Lambda^4}$.TodoIs more detail needed here? An advantage of this operator is that it includes all signatures with EW bosons, allowing to assess the relative sensitivity of the various channels with the same model. The kinematics for this operator is different with respect to other operators, leading to a harder $\not{E}_T$ spectrum, as illustrated by comparing the leading $b-$jet distribution for the dimension 5 operator to the dimension 8 operator.

3.2.4 Validity of EW contact operators and possible completions

It is important to remember that the operators described in this section may present problems in terms of the validity of the contact interaction approach for the energy scales reached at the LHC.

As outlined in [BLW14], designing very high $\not{E}_T$ search signal regions that are exclusively motivated by the hard $\not{E}_T$ spectra of
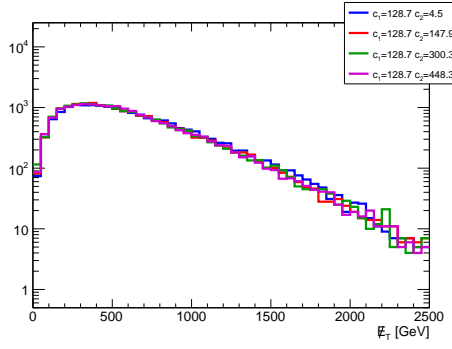
(a) Missing transverse momentum distribution.

(b) Acceptance.

Figure 3.24: $\not{E}_T$ distribution and acceptance for the dimension-7 model with a hadronically decaying Z in the final state, for the scalar and pseudoscalar operators representing direct interactions between DM and bosons. The y axis units are multiplied by 100.
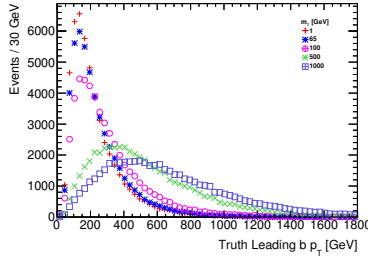
(a) Dimension 5 operator
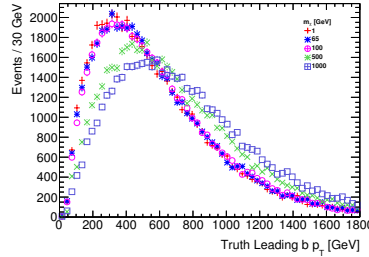
(b) Dimension 7 operator

Figure 3.25: Comparison of the transverse momentum for the leading $b-$ jet from the Higgs decay for a dimension 5 and dimension 7 operator with direct boson-DM couplings.

the dimension 7 and 8 operators will mean that the momentum transfer in the selected events is larger. This in turn means that processes at that energy scale (mediators, particles exchanged in loops) are accessible, and a simple contact interaction will not be able to correctly describe the kinematics of these signals.

Contact interaction operators like the ones in this section remain useful tools for comparison of the sensitivity of different search channels, and for reinterpretation of other models under the correct assumptions. To date, there are no UV-complete models available for most of those operators: dimension-7 operators are particularly

challenging since their completion involves loops [2].

However, this may be the focus of future theoretical exploration, as discussed in Ref. [CHH15]. An example of a complete model for scalar DM corresponding to the dimension-5 operator is provided in the Appendix B. Providing results for the pure EFT limit of these models will prove useful to cross-check the implementation of future.

Given these considerations, the recommendations on the presentation of the results for these models are:

- Deliver fiducial limits on the cross section of any new physics events, without any model assumption, according to the guidelines in Appendix C.

- Assess the percentage of events that pass the EFT validity condition, and present results using a truncation of the invalid events using the procedure in Section 4 alongside pure EFT results;

MODEL IMPLEMENTATION DISCUSSED IN APPENDIX **??**

[2] An example case for the need of loop completions is a simplified model with an additional scalar exchanged at tree level. The scalar couples to WW and ZZ in a gauge-invariant way, Integrating out the mediator does not lead to the Lorentz structure of a dimension-7 operator, so it is not possible to generate dimension-7 operators that satisfy gauge and Lorentz invariance at the same time. A model with a spin-1 mediator cannot be considered as a candidate for completion either, since dimension-7 operators only have scalar or pseudoscalar couplings.

4
Validity of EFT approach

Most of this report has focused on simplified models as an alternative to EFTs. Here, we wish to emphasize that Effective Field Theories (EFTs) can remain a useful tool in the interpretation of DM searches at the LHC. Given our current lack of knowledge about the nature of a DM particle and its interactions, a model independent interpretation of the collider bounds appears mandatory. This approach should be complemented with an interpretation within a choice of simplified models, which cannot exhaust the set of possible completions of an effective Lagrangian. Even when the application of EFT is not appropriate for the prediction of kinematics or cross sections, it does predict specific final states and can motivate experimental searches.

As we have learned, EFTs do not truly represent a model-independent representation of the data for the current collider sensitivity. Ideally, experimental results would be cast into bounds of allowed signal events in different kinematic regions. Until this is done systematically by the analyses, we present several prescriptions in the literature that can be used to quote bounds on EFT operators.

For the uninitiated, we illustrate the problem with EFTs by considering an effective interaction

$$(\bar{\psi}\psi)(\bar{\chi}\chi)\frac{g}{\Lambda^2}$$

that couples SM and DM fields. The strength of this interaction can be parametrized by $f = \frac{g}{\Lambda^2}$. A monojet signature can be generated by applying perturbation theory in the QCD coupling (assuming ψ is a quark, for example). An experimental search will place a limit on f. For a fixed f, a small value of g will correspond to a small value of Λ. The EFT approximation breaks down if $Q > \Lambda$, where Q is a typical hard scale of the process. One reasonable choice is $Q_{\mathrm{tr}}^2 = p(\bar{\chi}\chi)^2$, i.e. the momentum flow through the s-channel. Thus the limit on small g can only be reliable if the kinematic region $Q > \Lambda$ is removed from the prediction. On the other hand, if, for the same value of f, a large Λ is assumed so that the full kinematic region can be used, a large value of g is required, raising the question if perturbation theory is even applicable.

Here we summarize some methods that can be used to improve the reliability of the EFT approximation. These methods are described in detail in Refs. [BDSMR14, BDSG$^+$14, BDSJ$^+$14, A$^+$15,

RWZ15]. We then propose a recommendation for the presentation of EFT results for Run-2 LHC benchmarks.

4.1 Outline of the procedure described in Refs. [BDSG$^+$14, A$^+$15]

A standard approach has been to consider a simplified model and work backwards to determine the validity of the EFT approximation. For a tree-level interaction between DM and the Standard Model (SM) via some mediator with mass M_{med}, the EFT approximation corresponds to expanding the propagator for the mediator in powers of $Q_{\text{tr}}^2 / M_{\text{med}}^2$, truncating at lowest order, and combining the remaining parameters into a single parameter M_* (also called Λ in the literature). For an example scenario with a Z'-type mediator (leading to some combination of operators D5 to D8 in the EFT limit) this corresponds to setting

$$\frac{g_{\text{DM}}g_{\text{q}}}{Q_{\text{tr}}^2 - M^2} = -\frac{g_{\text{DM}}g_{\text{q}}}{M^2}\left(1 + \frac{Q_{\text{tr}}^2}{M^2} + \mathcal{O}\left(\frac{Q_{\text{tr}}^4}{M^4}\right)\right) \simeq -\frac{1}{M_*^2}, \quad (4.1)$$

where Q_{tr} is the momentum carried by the mediator, and g_{DM}, g_{q} are the DM-mediator and quark-mediator couplings respectively. Similar expressions exist for other operators. Clearly the condition that must be satisfied for this approximation to be valid is that $Q_{\text{tr}}^2 < M^2 = g_{\text{DM}}g_{\text{q}}M_*^2$. In this framework, there are clearly three regions to consider:

- $Q_{\text{tr}}^2 \sim M^2$, in which case the EFT misses a resonant enhancement, and it is conservative to ignore this enhancement;

- $Q_{\text{tr}}^2 \ll M^2$, in which case the EFT is valid; and

- $Q_{\text{tr}}^2 \gg M^2$, in which case the signal cross section should fall according to a power of Q_{tr}^{-1} instead of M^{-1}. This is the problematic kinematic region.

We can use the condition $Q_{\text{tr}}^2 < M^2 = g_{\text{DM}}g_{\text{q}}M_*^2$ to restrict the kinematics of the signal and enforce the validity of the EFT approximation (after the imposition of the event selection of the analysis). This truncated signal can then be used to derive the new, truncated limit on M_* as a function of $(m_{\text{DM}}, g_{\text{DM}}g_{\text{q}})$.

For the example D5-like operator, $\sigma \propto M_*^{-4}$, and so there is a simple rule for converting a rescaled cross section into a rescaled constraint on M_* if the original limit is based on a simple cut-and-count procedure. Defining $\sigma_{\text{EFT}}^{\text{cut}}$ as the cross section truncated such that all events pass the condition $\sqrt{g_{\text{DM}}g_{\text{q}}}M_*^{\text{rescaled}} > Q_{\text{tr}}$, we have

$$M_*^{\text{rescaled}} = \left(\frac{\sigma_{\text{EFT}}}{\sigma_{\text{EFT}}^{\text{cut}}}\right)^{1/4} M_*^{\text{original}}, \quad (4.2)$$

which can be solved for M_*^{rescaled} via either iteration or a scan (note that M_*^{rescaled} appears on both the LHS and RHS of the equation). Similar relations exist for a given UV completion of each operator.

The details and application of this procedure to ATLAS results can be found in Ref. [A+15] for a range of operators. Since this method uses the physical couplings and energy scale Q_{tr}, it gives the strongest possible constraints in the EFT limit while remaining robust by ensuring the validity of the EFT approximation.

If a search is not simply a counting experiment and exploits the shapes of kinematic distributions, the condition on the momentum transfer should be applied on the benchmarks using generator level information, by discarding events that are invalid. This provides the necessary rescaling of the cross section while keeping the information on the change in the kinematic distributions due to the removal of the invalid events.

4.2   Outline of the procedure described in Ref. [RWZ15]

In [RWZ15] a procedure to extract model independent and consistent bounds within the EFT is described. This procedure can be applied to any effective Lagrangian describing the interactions between the DM and the SM, and provides limits that can be directly reinterpreted in any completion of the EFT.

The range of applicability of the EFT is defined by a mass scale M_{cut}, a parameter which marks the upper limit of the range of energy scales at which the EFT can be used reliably, independently of the particular completion of the model. Regardless of the details of the full theory, the energy scale probing the validity of the EFT is less than or equal to the center-of-mass energy E_{cm}, the total invariant mass of the hard final states of the reaction. To be specific, consider the basic mono-jet process with kinematics $p_1 + p_2 \rightarrow k + p_{\bar{\chi}\chi}$: k is the momentum of the outgoing jet, whereas $p_{\bar{\chi}\chi}$ is the momentum of the $\bar{\chi}\chi$ pair and $p_{\bar{\chi}\chi} = Q_{tr}$. $E_{cm}^2 = (p_1 + p_2)^2 > Q_{tr}^2$. The condition ensuring the validity of the EFT is, by definition of M_{cut},

$$E_{cm} < M_{cut} \,. \tag{4.3}$$

For example, in the specific case of a tree level mediation with a single mediator, M_{cut} can be interpreted as the mass of that mediator.

There are then at least three free parameters describing an EFT: the DM mass m_{DM}, the scale M_* of the interaction, and the cutoff scale M_{cut}.

We can use the same technique as above to restrict the signal to the events for which $E_{cm} < M_{cut}$, using only these events to derive the exclusion limits on M_* as a function of (m_{DM}, M_{cut}). We can also define an *effective coupling strength* $M_{cut} = g_* M_*$, where g_* is a free parameter that substitutes the parameter M_{cut}, and therefore derive exclusions on M_* as a function of (m_{DM}, g_*). This allows us to see how much of the theoretically allowed parameter space has been actually tested and how much is still unexplored; For example, in the Z'-type model considered above, g_* is equal to $\sqrt{g_{DM} g_q}$. The resulting plots are shown in [RWZ15] for a particular effective operator.

The advantage of this procedure is that the obtained bounds can be directly and easily recast in any completion of the EFT, by computing the parameters M_*, M_{cut} in the full model as functions of the parameters of the complete theory. On the other hand, the resulting limits will be weaker than those obtained using Q_{tr} and a specific UV completion.

1540   ## 4.3   *Comments on Unitarity Considerations*

1541   ## 4.4   *Recommendation for presentation of EFT results*

1542   A full discussion of the presentation of collider results is left to
1543   work beyond this Forum, where ATLAS, CMS, the theory com-
1544   munity and the Direct and Indirect Detection communities are in-
1545   volved. In this report we recommend two strategies for the presen-
1546   tation of results in terms of Effective Field Theories. We divide the
1547   EFT operators in two categories: those which can be mapped to one
1548   or more UV-complete simplified models, such as those commonly
1549   used in LHC searches so far and detailed in [GIR$^+$10], and those for
1550   which no UV completion is available, such as those outlined in Sec-
1551   tion 3.2. Results for the first class of operators can be recast using
1552   simplified models with high mediator masses, therefore removing
1553   the need to explicitly simulate EFT events and provide experimen-
1554   tal limits for those operators. For the second class of models, a
1555   truncation procedure should be applied and the truncated results
1556   should be presented alongside the naive EFT results.

1557   Three proposals for the treatment of EFT have been stated so far:
1558   (1) truncate using Q_{tr}, (2) truncate and iterate using Q_{tr}, and (3)
1559   truncate using E_{cm}. Another possibility is to present the raw EFT
1560   results, but qualify that they might not be valid. Finally, one can
1561   quantify the validity of the EFT result by presenting the sensitivity
1562   to R, the fraction of events that satisfy $\hat{s} > M_{cut}^2$, for example.

1563   ## 4.5   *Recommendation for contact interaction theories with sim-*
1564   *plified models available*
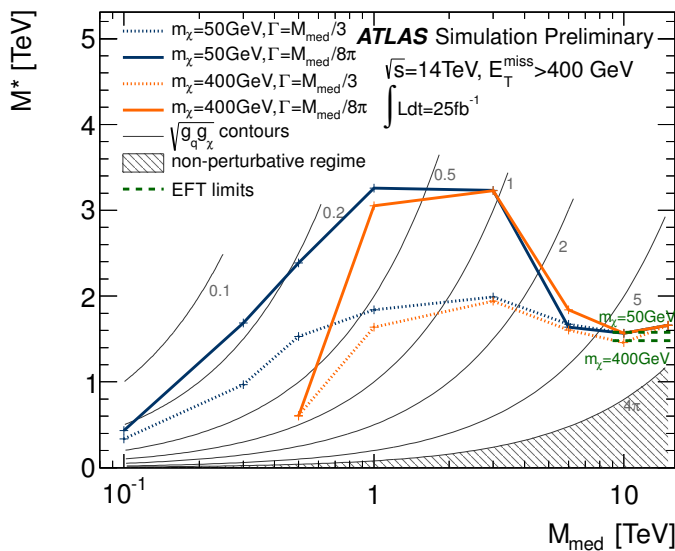
Figure 4.1: Comparison of the 95% CL lower limits on the scale of the interaction of a Z'-like simplified model at 14 TeV, in terms of the mediator mass. Corresponding limits from EFT models are shown on the same plot as green dashed lines to show equivalence between the two models for high mediator masses. Taken from Ref. [ATL14].

1565   If a simplified model can be mapped to a given EFT, then the
1566   model's high-mediator-mass limit will converge to the EFT. This

can be seen in Fig. 4.1, where the limits on the scale of the interaction of a Z'-like simplified model are presented in terms of the mediator mass [1]. The limits at high mediator mass for this model are equivalent to those of the corresponding EFT benchmark. For this reason, experimental collaboration should deliver results for high-mass mediators instead of pure EFT results, and leave further reinterpretation to theorists.

We therefore recommend the addition of one point at very high mediator mass (5 TeV) to the scan, for each of the DM masses for the simplified models described in Section 2. The truncation procedure in Section 4.2 can be used to fine-tune the mediator mass to be simulated for this purpose. Studies are ongoing for $s-$channel vector mediators.

4.6 Recommendation for truncation of theories with no simplified models available

Whenever a UV completion is not available, EFT results can still be a source of useful information as described in Section 3.2.4. However, we can only naively control the validity of the EFT operator. Despite the fact that a propagator was introduced to motivate the truncation procedure for s-channel models, the prescription is only dependent upon the simplified model to derive the energy scaling. The simple fact remains that the effective coupling of the operator – g/Λ^n – should not allow momentum flow $Q > \Lambda$ or $g > 4\pi$. Given our ignorance of the actual kinematics, the truncation procedure suggested for this purpose is the one described in Section 4.2, as it is independent from any UV completion details.

Because there is no UV completion, the parameter M_{cut} can be treated more freely than an explicit function of g and Λ. It makes sense to choose M_{cut} such that we identify the transition region where the EFT stops being a good description of UV complete theories. This can be done using the ratio R, which is defined as the fraction of events for which $s_{hat} > M_{\text{cut}}^2$. For large values of M_{cut}, no events are thrown away in the truncation procedure, and R=1. As M_{cut} becomes smaller, eventually all events are thrown away in the truncation procedure, i.e. $R = 0$, and the EFT gives no exclusion limits for the chosen acceptance.

We propose a rough scan over M_{cut}, such that we find the values of M_{cut} for which R ranges from 0.1 to 1. The analysis can then perform a scan over several values of M_{cut} , and show the truncated limit for each one of them alongside the naive limit corresponding to $R = 1$.

[1] This plot only serves as exemplification of the convergence of the simplified model to a contact interaction operator: before this Report, ATLAS and CMS searches presented search results up to very high couplings and therefore high widths, potentially probing unphysical corners of phase space

To do **The extrapolation to other couplings and mediator masses can be done using the Q_{tr} prescription for that model. (??)**

To do **agree on how many? (??)**

5

Recommendations for evaluation of signal theoretical uncertainties

[Comment on proper PDF sets to use, concerns about sea quark PDF in b-initiated diagrams (perhaps the latter belongs in the b-flavored DM section]

5.1 POWHEG

A comprehensive and careful assessment of theoretical uncertainties plays a much more important role for the background estimations (especially when their evaluation is non-entirely data-driven) than it does for signal simulations. Nevertheless, when using POWHEG it is possible to study scale and PDF errors for the dark matter signals. A fast reweighting machinery is available in POWHEG-BOX that allows one to add, after each event, new weights according to different scale or PDF choices, without the need to regenerate all the events from scratch.

To enable this possibility, the variable `storeinfo_rwgt` should be set to 1 in the POWHEG input file when the events are generated for the first time[1]. After each event, a line starting with

```
#rwgt
```

is appended, containing the necessary information to generate extra weights. In order to obtain new weights, corresponding to different PDFs or scale choice, after an event file has been generated, a line

```
compute_rwgt 1
```

should be added in the input file along with the change in parameters that is desired. For instance, `renscfact` and `facscfact` allow one to study scale variations on the renormalization and factorization scales around a central value. By running the program again, a new event file will be generated, named `<OriginalName>-rwgt.lhe`, with one more line at the end of each event of the form

```
#new weight,renfact,facfact,pdf1,pdf2
```

[1] Notice that even if the variable is not present, by default it is set to 1.

followed by five numbers and a character string. The first of these numbers is the weight of that event with the new parameters chosen. By running in sequence the program in the reweighting mode, several weights can be added on the same file. Two remarks are in order.

- The file with new weights is always named

  ```
  <OriginalName>-rwgt.lhe
  ```

  hence care has to be taken to save it as

  ```
  <OriginalName>.lhe
  ```

  before each iteration of the reweighting procedure.

- Due to the complexity of the environment where the program is likely to be run, it is strongly suggested as a self-consistency check that the first reweighting is done keeping the initial parameters. If the new weights are not exactly the same as the original ones, then some inconsistency must have happened, or some file was probably corrupted.

It is possible to also have weights written in the version 3 Les Houches format. To do so, in the original run, at least the token

```
lhrwgt_id 'ID'
```

must be present. The reweighting procedure is the same as described above, but now each new run can be tagged by using a different value for the `lhrwgt_id` keyword. After each event, the following lines will appear:

```
<rwgt>
<wgt id='ID'>
<wgt id='ID1'>
</rwgt>
```

A more detailed explanation of what went into the computation of every single weight can be included in the <header> section of the event file by adding/changing the line

```
lhrwgt_descr 'some info'
```

in the input card, before each "reweighting" run is performed. Other useful keywords to group together different weights are `lhrwgt_group_name` and `lhrwgt_group_combine`.

More detailed information can be obtained by inspecting the document in /Docs/V2-paper.pdf under the common POWHEG-BOX-V2 directory.

5.2 MadGraph5_aMC@NLO

6
Conclusions

Points to be made in a conclusion:

- In the case of s-channel simplified models, in particular, there is complementarity between searches for dark matter and visible particles. Thus, limits on invisible decays must be consistent with dijet and dilepton searches. In the case of the mono-top simplified model, limits on visible single-top final states must be considered.

- There are many implicit assumptions that have not been laid out entirely in our presentation. As stated earlier, the term "dark matter' in this report refers to a putative dark matter candidate. The details of a particular mono-X analysis rely on the fact that a WIMP exists, and that it is collider-stable. The observation of a signal consistent with WIMP production does can only provide indirect or confirming evidence of a dark matter particle.

- The presentation of results comparing different experimental frontiers has to be done carefully and clearly. We see the need for broader discussions on this topic.

- The experiments should aim to present limits on production cross sections corrected for acceptance when this is viable.

- The Appendix contains a presentation of some models that came out in our discussions that were not deemed a priority for early Run2 analyses. However, these should be considered in the future.

A

Appendix: Implementation of Models

A.1 *Implementation of s-channel and t-channel models for $\not{E}_T$ +X analyses*

There are several matrix element implementations of the DM production through spin-0 and spin-1 mediators. This Appendix collects the generator recommendations and available implementations of these models for different final states, together with studies of the matching between the matrix element and the parton shower.

A.1.1 *Implementation of models for mono-jet signature*

For a spin-1 mediator, the implementation in POWHEG generates DM pair production with 1 parton at next-to-leading order (NLO), whilst MadGraph5_aMC@NLO and mcfm are at leading order (LO) [1]. As shown in POWHEG Ref. [HKR13], including NLO corrections result in an enhancement in the cross section as compared to LO and though this is not significant, it does lead to a substantial reduction in the dependence on the choice of the renormalization and factorization scale and hence the theoretical uncertainty on the signal prediction. Since NLO calculations are available for the process in POWHEG, we recommend to proceed with POWHEG as the generator of choice.

For a spin-0 mediator in the mono-jet final state, the top-quark loop is the most important consideration. The matrix element implementation of the *s*-channel spin-0 mediated DM production is available in mcfm [FW13, HKSW15] and POWHEG [HR15] with the full top-loop calculation at LO. The POWHEG and mcfm implementations include the finite top quark mass dependence for DM pair production with 1 parton at LO. For consistency with the spin-1 generation, we recommend using POWHEG for this case as well.

Here, we document some specific settings needed to run the POWHEG generation for the Dark Matter models. POWHEG parameter cards for all models can be found on the Forum SVN repository [For15h, For15j, For15k, For15i].

- POWHEG can handle the generation of events (be it at LO or NLO) in two different modes explained in the following. The second one is the recommended one. The relevant keywords in the input

[1] Spin-0 and spin-1 mediator models will also be provided in the near future to the same precision in MadGraph5_aMC@NLO [A⁺14b].

card are `bornsuppfact` and `bornktmin`.

1. unweighted events:

   `bornsuppfact`: negative or absent

   `bornktmin <PT>`

   This runs the program in the most straightforward way, but most likely it is not the more convenient choice, as will be explained below. POWHEG will generate unweighted events using a sharp lower cut (with value `PT`) on the leading-jet p_{T}. Since this is a generation cut, the user should make sure that the value used for `bornktmin` is lower than the actual analysis cut to be eventually used. It is good practice to use as a value in the input card a transverse momentum 10-20% smaller than the final analysis cut, and check that the final result is independent, by exploring an even smaller value of `bornktmin`. The drawback of this running mode is that it's difficult to populate well and in a single run both the low-p_{T} region as well as the high-pT tail.

2. weighted events:

   `bornsuppfact <PTS>`

   `bornktmin <PT>`

   POWHEG will now produce weighted events, thereby allowing to generate a single sample that provides sufficient statistics in all signal regions. Events are still generated with a sharp lower cut set by `bornktmin`, but the `bornsuppfact` parameter is used to set the event suppression factor according to

$$F(k_{\mathrm{T}}) = \frac{k_{\mathrm{T}}^2}{k_{\mathrm{T}}^2 + \texttt{bornsuppfact}^2} \ . \tag{A.1}$$

   In this way, the events at, for instance, low $\not{E}_T$, are suppressed but receive an higher weight, which ensures at the same time higher statistics at high $\not{E}_T$. We recommend to set `bornsuppfact` to 1000.

   The `bornktmin` parameter allows to suppress the low $\not{E}_T$ region even further by starting the generation at a certain value of k_{T} also in this running mode. It is recommended to set this parameter to half the lower analysis $\not{E}_T$ cut. For instance for the event selection used in the CMS/ATLAS monojet analyses, assuming the lowest $\not{E}_T$ region being defined above 300 GeV, the proposed value for `bornktmin` is 150. However, this parameter should be set keeping in mind the event selection of all the analyses that will use these signal samples and hence a threshold lower than 150 may be required.

- Remove the `runningwidth` keyword, or set it to 0, which is the default value. Running with fixed widths is the recommended option. Although there are limitations, this is the more straightforward, simple and transparent option, and it was used for Forum studies.

To do **Emanuele:"On the usage of fixed or running width. It is my opinion that one should use fixed widths. Although clearly there are limitations, I think this goes into the direction of making all as simple and transparent as possible. Moreover, all the discussions in the last months as well as the large majority of runs were done with fixed widths. Since there was some interest over the last couple of weeks, here is my suggestion for the POWHEG section."** (??)

While not recommended, the alternative, a running width for the propagator of the s-channel mediator, can be selected by setting runningwidth to 1. In this case the denominator of the mediator's propagator

$$Q^2 - M^2 + i\,M\,\Gamma$$

is replaced by

$$Q^2 - M^2 + i\,Q^2\,\frac{\Gamma}{M}$$

where Q is the virtuality of the mediator, and M and Γ are its mass and width respectively.

- Set the parameters defining the bounds on the invariant mass of the Dark Matter pair, `mass_low` and `mass_high`, to -1. In this way, POWHEG will assign values internally.

- The minimal values for `ncall1`, `itmx1`, `ncall2`, `itmx2` are 250000, 5, 1000000, 5 for the `DMV` model, respectively.

- The minimal values for `ncall1`, `itmx1`, `ncall2`, `itmx2` are 100000, 5, 100000, 5 for the `DMS_tloop` model, respectively.

- When NLO corrections are included (as for instance in the `DMV` model), negative-weighted events could happen and should be kept in the event sample, hence `withnegweights` should be set to 1. If needed, their fraction can be decreased by setting `foldsci` and `foldy` to bigger value (2 for instance). `foldphi` can be kept to 1.

- Since the `DMS_tloop` model is a leading order process, set `LOevents` and `bornonly` are set to 1 internally.

- One can benefit from the automatic calculation of systematic uncertainties associated with the choice of hard scale and PDFs as described in Section 5.

A.1.2   Parton matching studies

Whenever models for mono-jet final states are generated in MAD-GRAPH5_AMC@NLO, it is necessary to avoid double counting the partons from matrix elements and parton showering in PYTHIA 8 using a parton matching technique. Based on the comparative study in Ref. [A+08], we recommend using the CKKW-L matching scheme.

A.1.2.1   Implementation of the CKKW-L matching

To illustrate the settings related to parton matching, the EFT D5 samples are generated with MADGRAPH5_AMC@NLO version 2.2.2 and showered in PYTHIA 8.201. The technical implementation of the CKKW-L k_t-merging scheme is shown below.

- On the generator side:
  ```
  ickkw = 0
  ktdurham = matching scale
  dparameter = 0.4
  dokt = T
  ptj=20
  drjj=0
  mmjj=0
  ptj1min=0
  ```

- On the parton showering side in PYTHIA 8.2: `Merging:ktType = 1`
  ```
  Merging:TMS = matching scale
  1000022:all = chi chi˜ 2 0 0 30.0 0.0 0.0 0.0 0.0, where 2
  ```
  stands for the DM particle spin and 30 stands for its mass in GeV
  ```
  1000022:isVisible = false
  Merging:doKTMerging = on
  Merging:Process = pp>{chi,1000022}{chi˜,-1000022}
  Merging:nJetMax = 2
  ```

The matching scales should be the same for the generation and parton showering. In MADGRAPH5_AMC@NLO, the particle data group ID `1000022` is used for weakly interacting dark matter candidates. The dark matter particle is defined in PYTHIA 8 accordingly using the commands above that specify an invisible spin ½ particle of 30 GeV mass. The `Mergin:Process` command specifies the lowest parton emission process generated in MADGRAPH5_AMC@NLO and `Merging:nJetMax = 2` gives the maximum number of additional parton emissions with respect to the lowest parton emission process. Therefore, the following three processes need to be generated in this case:
```
p p > chi chi˜
p p > chi chi˜ j
p p > chi chi˜ j j
```
Note that the MADGRAPH5_AMC@NLO cards and PYTHIA 8 commands are identical for all three samples.

A.1.2.2 *Matching scale*

In general, it is desired to take the hard parton emissions from the matrix element generation in MADGRAPH5_AMC@NLO and allow PYTHIA 8 to take care of soft emissions only. The transition between these two regimes is defined by the matching scale and its optimal value can be determined by studying the cross-section as a function of the number of jets (differential jet rates). The differential rates $\frac{dN_{i \to j}}{d \log_{10}(k_{\text{cut}})}$ give the number of events which pass from i jets to j jets as the k_t value increases beyond k_{cut}. An optimal matching scale should lead to smooth differential jet rates.

Two examples of differential jet rates, using matching scale 30 GeV and 80 GeV, from the EFT D5 sample generated as described in the previous section are given in Fig. A.1 and A.2, respectively. Although a kink is visible around the matching scale value

in both cases, the 80 GeV scale leads to smoother distributions. In order to find the optimal matching scale, additional samples with matching scale 50, 70, and 90 GeV are generated as well and a detailed comparison of the differential jet rates close to the transition region is shown in Fig. A.3. The largest differences among the samples are visible for the $1 \to 2$ jets transition where the 30 GeV and 50 GeV scale lead to a drop of the rates around the matching scale values. On the contrary, there is a hint of an increased rate around the matching scale value in the sample generated with the 90 GeV scale. Therefore, we recommend to use 80 GeV as the baseline matching scale.

(a) $1 \to 2$ jets

(b) $2 \to 3$ jets

(c) $3 \to 4$ jets

(d) $4 \to 5$ jets
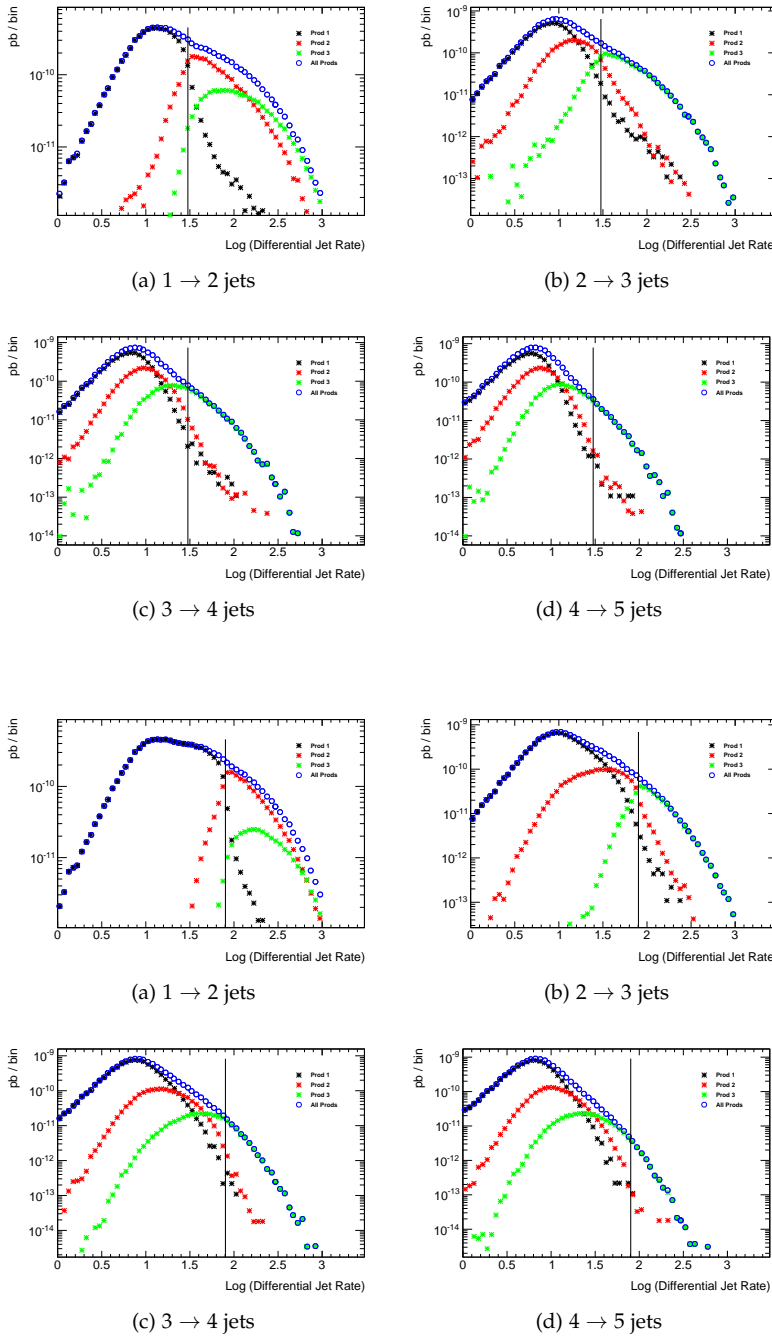
Figure A.1: Distributions of differential jet rates $\frac{dN_{i \to j}}{d\log_{10}(k_{\mathrm{cut}})}$ for EFT D5 sample with CKKW-L matching scale at 30 GeV. The 0-, 1- and 2-parton emission samples are generated separately and indicated in the plots as Prod 1, Prod 2 and Prod 3, respectively. A vertical line is drawn at the matching scale.

(a) $1 \to 2$ jets

(b) $2 \to 3$ jets

(c) $3 \to 4$ jets

(d) $4 \to 5$ jets
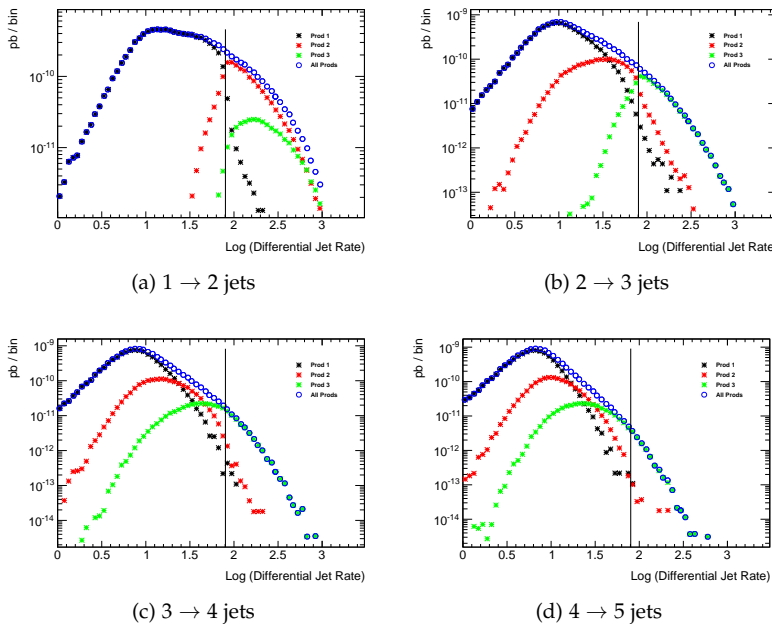
Figure A.2: Distributions of differential jet rates $\frac{dN_{i \to j}}{d\log_{10}(k_{\mathrm{cut}})}$ for EFT D5 sample with CKKW-L matching scale at 80 GeV. The 0-, 1- and 2-parton emission samples are generated separately and indicated in the plots as Prod 1, Prod 2 and Prod 3, respectively. A vertical line is drawn at the matching scale.
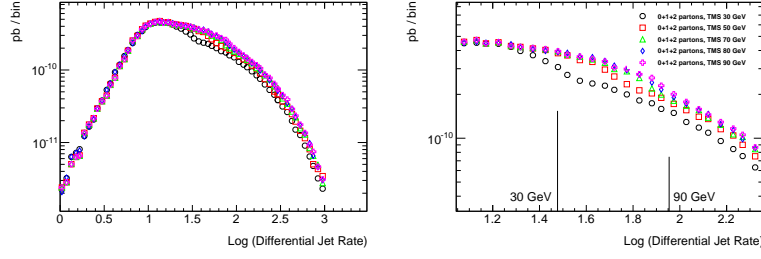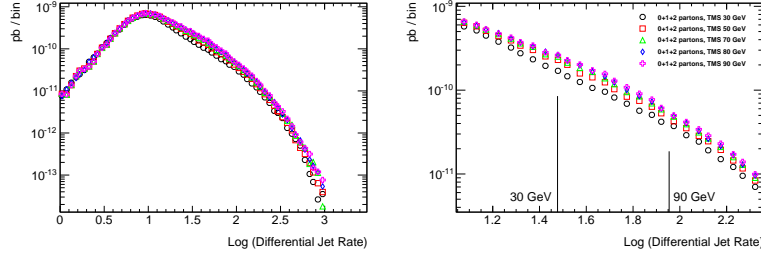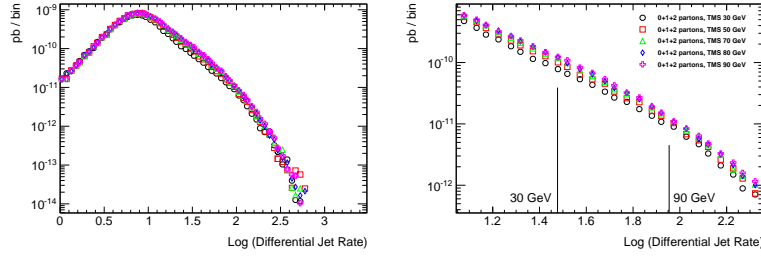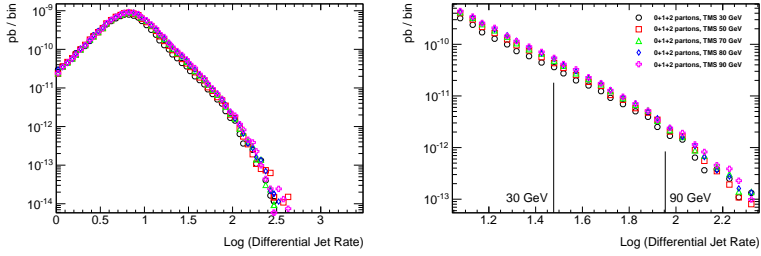
Figure A.3: Distributions of differential jet rates $\frac{dN_{i \to j}}{d \log_{10}(k_{\text{cut}})}$ for EFT D5 sample with CKKW-L matching scale at 30, 50, 70, 80 and 90 GeV. A zoom of the region around the matching scale values is shown on right.

(a) $1 \to 2$ jets

(b) $2 \to 3$ jets

(c) $3 \to 4$ jets

(d) $4 \to 5$ jets

A.1.2.3   *Parton emission multiplicity*

The prescription for the event generation given in Section A.1.2.1 starts with the emission of 0 partons and ends with maxim 2 partons in addition. Producing the samples separately allows to investigate the relative composition of the individual samples in various parts of the phase space. Figure A.4 shows the $\not{E}_T$ distribution of the EFT D5 sample with the matching scale at 80 GeV. The plot reveals that the 0-parton sample gives the dominant contribution in the region below the matching scale value that rapidly decreases at higher $\not{E}_T$. Assuming the lowest analysis $\not{E}_T$ cut in Run-2 mono-jet analyses at 300 GeV, the generation of the 0-parton emission sample can be safely omitted as it only gives < 1% contribution at $\not{E}_T$ > 300 GeV. For the 1- and 2-parton emission samples, one can

use a generator cut on the leading parton p_T, `ptj1min`, in order to avoid generating low $\not{E}_T$ events that are irrelevant for the analysis.
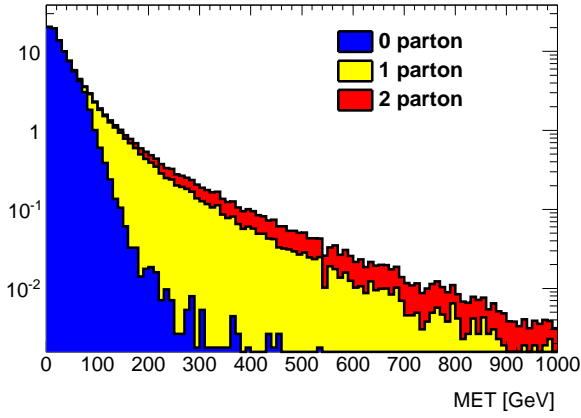
Figure A.4: Missing transverse momentum distributions for EFT D5 sample with CKKW-L matching scale at 80 GeV. Individual contributions from the 0-, 1- and 2-parton emission samples are shown.

In order to describe the signal kinematics correctly and save time during MC production, the parton emissions will only be generated up to a certain multiplicity. The higher multiplicity samples usually have small enough cross sections and the corresponding parts of the phase space can be sufficiently approximated by parton showering in PYTHIA 8. A dedicated study comparing samples generated with up to 1-, 2-, or 3-parton multiplicities was performed, using again the settings for the CKKW-L k_t-merging with the 80 GeV matching scale and the `Merging:nJetMax` parameter adjusted accordingly. Figure A.5 shows the $\not{E}_T$ distribution of the samples at $\not{E}_T > 250$ GeV.

With an event selection requiring $\not{E}_T$ and the leading jet p_T being larger than 250 GeV and allowing for up to 4 jets with $p_T > 30$ GeV, the sample generated with up to 1 parton has 17.4% smaller yield compared to the sample with up to 3 partons, while the yield of the sample with up to 2 partons is only 2.2% smaller. This justifies it is sufficient to produce samples with up to 2 parton emissions only at the generator level and ignore generating higher parton emissions.

(a) No jet multiplicity cut

(b) $N_{\text{jet}} \leqslant 3$
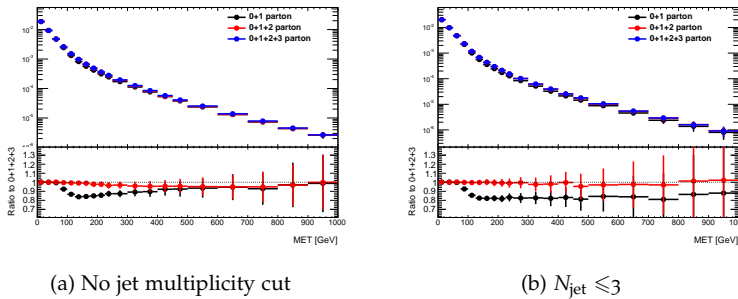
Figure A.5: Missing transverse momentum distributions for EFT D5 sample with CKKW-L matching scale at 80 GeV produced with maximum 1 (black), 2 (red) and 3 (blue) partons emitted at the generator level. The ratios are shown with respect to the latter sample.

A.1.3   *Implementation of models for EW final states*

These models are generated at leading order with MADGRAPH5_AMC@NLO 2.2.2, using Pythia8 for the parton shower. Parameter cards can be
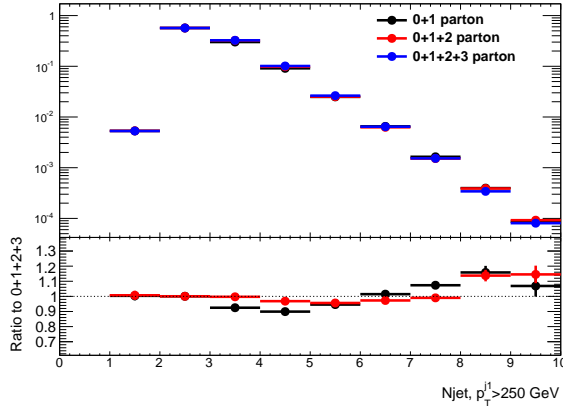
Figure A.6: Multiplicity of jets with $p_T > 30$ GeV and $|\eta| < 2.8$ for EFT D5 sample with CKKW-L matching scale at 80 GeV produced with maximum 1 (black), 2 (red) and 3 (blue) partons emitted at the generator level. The ratios are shown with respect to the latter sample. The leading jet p_T is required to be larger than 250 GeV.

found on the Forum SVN repository [For15a]. No parton matching is required.

A.1.4 Implementation of models with heavy flavor quark signatures

The models for the $t\bar{t}$ and $b\bar{b}$ signatures are generated at leading order with MADGRAPH5_AMC@NLO 2.2.2, using Pythia8 for the parton shower. No matching is needed. Parameter cards can be found on the Forum SVN repository [For15d]. No parton matching is required.

We simulate the bFDM model using the MG5_aMC v2.2.3, using Pythia8 for the parton shower. No matching is needed. The corresponding card files can be found on the Forum SVN repository [For15f].

A.1.4.1 Quark flavor scheme and masses

In this particular model we recommend an additional care when choosing the flavor scheme generation and whether quarks should be treated as massive or massless.

The production of DM+$b\bar{b}$, Dark Matter in association with b jets via a decay of a (pseudo) scalar boson, is dominated in simplified mediator models by the gluon-gluon initiated production, similar to the production of Z+$b\bar{b}$ at the LHC. The Z+$b\bar{b}$ process has been studied in detail in the Z(ll)+b-jets final state, which can be used to validate both the modeling of DM+bb and, its main background, Z(vv)+$b\bar{b}$. In this context, the p_T of the Z boson is related to the observed MET, whereas the b-jet kinematics determines the ratio of mono-b/di-b signatures in the detector.

For basic kinematic criteria applied to Z+$b\bar{b}$ production, this process leads in $\sim$ 90% of the events to a signature with only 1 b-jet in the acceptance ('Z+1b-jet production') and only in $\sim$ 10% of the events to a signature with 2 b-jets in the detector ('Z+2b-jets production). The production cross section of the Z+$b\bar{b}$ process are calculated in the 'five-flavor scheme', where b quarks are assumed massless, and the 'four-flavor scheme', where massive b quarks

are used [CEMW04, MMW05, CEMW06], and data favor the cross-section predictions in the five-flavor scheme [C$^+$14]. We therefore recommend to calculate the cross sections of these models in the 5-flavor scheme, as in the repository. The PDF used to calculate these cross section is NNPDF3.0 (lhaid 263000).

It is found that the best modeling of two *b*-quarks final states is achieved using a 4-flavor scheme and a massive treatment of the *b*-quarks [**?** Col15]. We recommend to use in the generation NNPDF3.0 set (lhaid 263400). Since figure A.7 shows that there is no significant difference in the kinematics between either flavor scheme used for DM+$b\bar{b}$ production, we recommend the 4-flavor scheme to follow the observation in the Z+$b\bar{b}$ measurements.
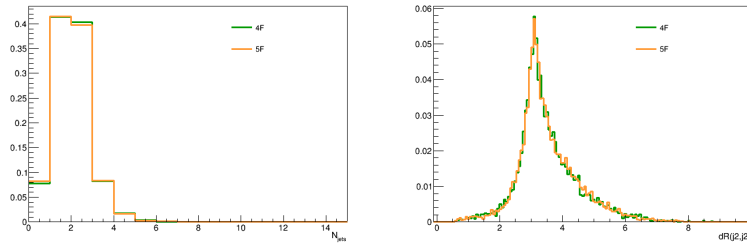
Figure A.7: Comparison of the jet multiplicity (left) and angular correction $\Delta R(j_1, j_2)$ (right) for the DM+$b\bar{b}$ scalar model generated in the 4-flavor and 5-scheme. The samples are generated for $m_\chi = 1$ GeV and $m_\phi = 10$ GeV.

A.2 Implementation of specific models for $V + \not{E}_T$ analyses

A.2.1 Model implementation for mono-Higgs models

All three Higgs+$\not{E}_T$ models are generated at leading order with MadGraph5_aMC@NLO 2.2.2, using pythia 8 for the parton shower. No matching is needed. The MadGraph5_aMC@NLO implementations of the scalar and vector models can be found on the Forum SVN repository [For15g], while the 2HDM model can be found at this link [For15b].

In all cases, it is recommended not to handle the *h* decay through MadGraph5_aMC@NLO as it does not include the proper *h* branching ratios, or, if using MadGraph5_aMC@NLO, then the resulting cross section should be rescaled to match onto the correct branching ratio.

MadGraph5_aMC@NLO details for scalar mediator Higgs+MET model

In this model, the contribution from the *gghS* box is included through an effective Lagrangian evaluated in the large m_t limit. This may overestimate the rates of the $h + \not{E}_T$ signal [HKU13], but a full evaluation is left to future studies.

MadGraph5_aMC@NLO details for 2HDM Higgs+MET model

The two couplings that can be changed in the implemented model follow the nomenclature below:

• Tb - tan β

• gz - g_z, gauge coupling of Z' to quarks

The other couplings are not changed, including gx (the $A\bar{\chi}\chi$ coupling) which has little impact on the signal. $\sin\alpha$ is fixed internally such that $\cos(\beta - \alpha) = 0$. The width of the Z' and A can be computed automatically within MADGRAPH5_AMC@NLO. The couplings here don't affect the signal kinematics, so they can be fixed to default values and then the signal rates can be scaled appropriately.

The nomenclature for the masses in the implemented model is:

• MZp - PDG ID 32 - Z'

• MA0 - PDG ID 28 - A

• MX - PDG ID 1000022 - dark matter particle

The other masses are unchanged and do not affect the result. Both $Z' \to hZ(\bar{\nu}\nu)$ and $Z' \to hA(\bar{\chi}\chi)$ contribute to the final state, scaling different with model parameters. We recommend to generate them separately, and then add the two signal processes together weighted by cross sections.

A.2.2 *Implementation of EFT models*

A.3 *Heavy Flavor Models*

In this particular model we recommend an additional care when choosing the flavor scheme generation. It is found that the best modeling of two b-quarks final states is achieved using a 4-flavor scheme and a massive treatment of the b-quarks . In addition, we recommend to calculate the cross sections of these models in the 5-flavor scheme, and as in the *tbart* case we provide values for the suggested coupling scan in the appendix. The PDF used to calculate these cross section is NNPDF3.0 (lhaid 263000).

To do [TODO: Add reference] (??)

To do [TODO: The following figures are placeholders for now and will be added later] (??)
Figure A.8: Comparison of the subleading jet p_T and b-jet multiplicity for bb+DM scalar model generated in the 4-flavor (left) and 5-flavor (right) schemes, respectively

A.4 *Single Top Models*

Card files for MADGRAPH5_AMC@NLO are provided on the Forum SVN repository [For15e], corresponding to the Lagrangian from [AFM11]. Each coupling constant of this model can be set via the parameter card and the blocks which are relevant for the two models used for the experimental searches are described below. The relevant parameters in the MADGRAPH5_AMC@NLO parameter cards, also expressed in the notation introduced in the previous Section, are as follows for the two models considered.

1. Resonant scalar model described by the Lagrangian (B.1)

- **AQS** and **BQS**: 3×3 matrices (flavor space) fixing the coupling of the scalar ϕ (S stands for scalar) and *down*-type quarks (Q stands for quarks), previously called a^q/b^q_{SR}.

- **A12S** and **B12S**: 3×1 matrices (flavor space) fixing the coupling of the new fermion χ (where 12 stands for spin-$1/2$ fermion) and *up*-type quarks, previously called $a^{1/2}_{VR}$.

2. Non-resonant vectorial model described by the Lagrangian (B.3)

- **A1FC** and **B1FC**: 3×3 matrices (flavor space) fixing the coupling of the vector V (1 stands for vector) and *up*-type quarks, previously called a^1_{FC}.

- particle name: the dark matter candidate χ is not implemented

The width of the scalar resonance and of the new vector are set to all allowed decays in the ATLAS implementation, while the only allowed decay in the CMS implementation to the new fermion and a top quark for the resonant model.

To do **Continue discussion between ATLAS and CMS to reach an agreement, or include instructions to compare results. (??)**

A.5 EFT Mono-Higgs implementation

These models are generated at leading order with MADGRAPH5_AMC@NLO 2.2.2, using PYTHIA 8 for the parton shower. No matching is performed. Parameter cards can be found on the Forum SVN repository: [For15g] for operators with Higgs+MET final states and [For15c] for $W/Z/\gamma$ final states.

B

Appendix: Additional models for Dark Matter searches

B.1 Models with a single top−quark + MET

Many different theories predict final states with a single top and associated missing transverse momentum (monotop), some of them including dark matter candidates. A simplified model encompassing the processes leading to this phenomenology is described in Refs. [AFM11, AAB$^+$14, BCDF15], and is adopted as one of the benchmarks for Run 2 LHC searches.

The simplified model is constructed by imposing that the model Lagrangian respects the electroweak $SU(2)_L \times U(1)_Y$ gauge symmetry and by requiring minimality in terms of new states to supplement to the Standard Model fields. As a result, two monotop production mechanisms are possible. In the first case, the monotop system is constituted by an invisible (or long-lived with respect to detector distances) fermion χ and a top quark. It is produced, as shown in the diagram of B.1 (a) where a colored resonance φ lying in the triplet representation of $SU(3)_C$ decays into a top quark and a χ particle. In the second production mode, the monotop state is made of a top quark and a vector state V connected to a hidden sector so that it could decay invisibly into, e.g., a pair of dark matter particles as studied in [BCDF15]. The production proceeds via flavor-changing neutral interactions of the top quark with a quark of the first or second generation and the invisible V boson (see the diagrams of B.1 (b) and (c)).

Resonant production

In this case, a colored 2/3-charged scalar (φ) is produced and decays into a top quark and a spin-1/2 invisible particle, χ. The dynamics of the new sector is described by the following Lagrangian:

$$\mathcal{L} = \left[\varphi \bar{d}^c \left[a^q_{SR} + b^q_{SR} \gamma_5 \right] d + \varphi \bar{u} \left[a^{1/2}_{SR} + b^{1/2}_{SR} \gamma_5 \right] \chi + \text{h.c.} \right] \qquad \text{(B.1)}$$

where u (d) stands for any up-type (down-type) quark, the notation SR refers to the monotop production mechanism via a scalar resonance and all flavor and color indices are understood for clarity.

In the notation of [AAB$^+$14], the couplings of the new colored fields to down-type quarks are embedded into the 3×3 antisym-
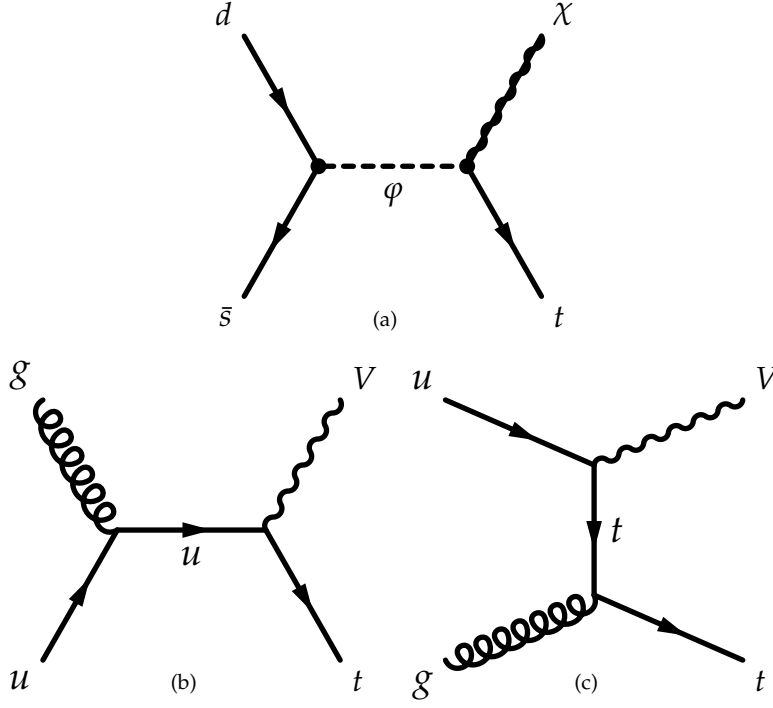
Figure B.1: Feynman diagram of leading order processes leading to monotop events: production of a coloured scalar resonance φ decaying into a top quark and a spin-1/2 fermion χ (a), $s-$ (b) and t-channel (c) non resonant production of a top quark in association with a spin-1 boson V decaying invisibly.

metric matrices a^q_{SR} (scalar couplings) and b^q_{SR} (pseudoscalar couplings) while those to the new fermion χ and one single up-type quark are given by the three-component vectors $a^{1/2}_{\{S\}R}$ and $b^{1/2}_{\{S\}R}$ in flavor space.

Under the form of Eq. (B.1), the Lagrangian corresponds to the one introduced in the original monotop search proposal [AFM11] and has been used by the CMS for Run I analyses after neglecting the pseudoscalar component of the coupling and adding the vector resonance case for which minimality requirements are difficult to accomodate [CMS14]. In contrast, the study of Ref. [BCDF15] has imposed electroweak gauge invariance and requires minimality, which enforces all new couplings to be right-handed,

Under the form of Eq. (B.1), the Lagrangian is the one introduced in the original monotop search proposal [AFM11]. It has been used by the CMS collaboration for Run I analyses after neglecting all pseudoscalar components of the couplings and adding the vector resonance case for which minimality requirements are difficult to accommodate [CMS14]. In contrast, the study of Ref. [BCDF15] has imposed electroweak gauge invariance and required minimality. This enforces all new couplings to be right-handed so that

$$a^{1/2}_{SR} = b^{1/2}_{SR} = \frac{1}{2}y^*_s \qquad \text{and} \qquad a^q_{SR} = b^q_{SR} = \frac{1}{2}\lambda_s \, , \qquad \text{(B.2)}$$

where the objects λ_s and y_s are a tridimensional vector and a 3×3 matrix in flavor space respectively. This class of scenarios is the one that has been adopted by the ATLAS collaboration for its Run I monotop searches [ATL15] and will be considered by both collaborations for Run II analyses.

The resulting model can be likened to the MSSM with an R-parity violating of a top squark to the Standard Model down-type

2090 quarks and an *R*-parity conserving interaction of a top quark and a
2091 top-squark to a neutralino.

Non-Resonant production

For non-resonant monotop production, the monotop state is
produced via flavor-changing neutral interactions of the top quark,
a lighter up-type quark and a new invisible vector particle *V*. This
is the only case considered, as having a new scalar would involve
a mixing with the SM Higgs boson and therefore a larger number
of free parameters. The Lagrangian describing the dynamics of this
non-resonant monotop production case is:

$$\mathcal{L} = \left[V_\mu \bar{u} \gamma^\mu \left[a^1_{FC} + b^1_{FC} \gamma_5 \right] u + \text{h.c.} \right] \tag{B.3}$$

2093 where the flavor and color indices are again understood for clarity.
2094 The strength of the interactions among these two states and a
2095 pair of up-type quarks is modeled via two 3×3 matrices in flavor
2096 space $a^{\{1\}}_{FC}$ for the vector couplings and $b^{\{1\}}_{FC}$ for the axial vector
2097 couplings.

As for the resonant case, the Lagrangian of Eq. (B.3) is the one
that has been used by CMS after reintroducing the scalar option
for the invisible state and neglecting all pseudoscalar interac-
tions [CMS14]. as already mentioned, a simplified setup motivated
by gauge invariance and minimality has been preferred so that, as
shown in Ref. [BCDF15], we impose all interactions to involve right-
handed quarks only in order to simplify the model phenomenology,

$$a^1_{FC} = b^1_{FC} = \frac{1}{2} a_R \tag{B.4}$$

2098 where a_R denotes a 3×3 matrix in flavor space.

Model parameters and assumptions

2100 The models considered as benchmarks for the first LHC searches
2101 contain further assumptions in terms of the flavor and chiral struc-
2102 ture of the model with respect to the full Lagrangians of equa-
2103 tions (B.1) and (B.3).
2104 This implies the vector to be an SU(2)L singlet, hence in turn
2105 setting the vector and axial vector matrices to have elements of
2106 equal values.

In order to have an observable monotop signature at the LHC,
the Lagrangians introduced above must include not too small cou-
plings of the new particles to first and second generation quarks.
For simplicity, we assumed that only channels enhanced by parton
density effects will be considered, so that we fix

$$
\begin{aligned}
(a_R)_{13} = (a_R)_{31} &= a \,, \\
(\lambda_s)_{12} = -(\lambda_s)_{21} = \lambda \quad \text{and} \quad (y_s)_3 &= y \,,
\end{aligned}
\tag{B.5}
$$

2107 all other elements of the matrices and vectors above being set to
2108 zero.   To do (**??**)

IMPLEMENTATION The Monte Carlo simulation relevant for this

case is discussed in Appendix A.

B.1.1   Parameter scan

The relevant parameters for the resonant model are:

• The mass of the new scalar ϕ;

• The mass of the new fermion χ;

• The coupling of the new scalar to the new fermion and top quark
a, related to the width of the scalar in the minimal width as-
sumption;

The relevant parameters for the non-resonant model are:

• The mass of the new vector V;

• The coupling of the new vector to the up and top quark a, re-
lated to the width of the scalar in the minimal width assumption;

• The coupling of the new vector to the new fermion χ, related
to the branching fraction of the vector into invisible and visible
particle, and as a consequence to the width of the vector.

In the case of the non-resonant model, the invisible vector is
connected to a hidden sector that could be, in its simplest form,
parameterized by a new fermion. This has effects on the width of
the invisible V state.

It has been checked for the non-resonant model that the relevant
kinematics does not change when changing the width of the res-
onance, for widths up to 10% of the V mass. Figures B.2 and B.3
show the V mass distribution, the transverse momentum for V in
the case of the $V \to t\bar{u}$ decay, for different V masses and widths.
Since they only show kinematic quantities related to V, these fig-
ures are relevant independently of the V decay mode (be it visible
or invisible).
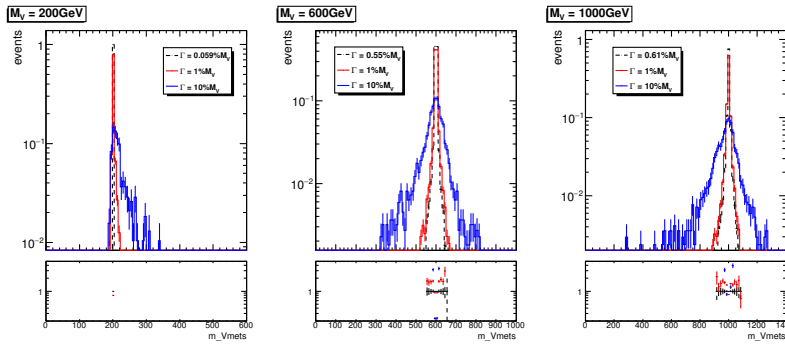
To do **Pictures will be improved in the next drafts. (??)**

Figure B.2: Distribution of V invariant mass for the $gu \to tV(\to t\bar{u})$ (on-shell V) for m_V = 200, 600, 1000 GeV (from left to right) and for three different visible decay width (computed from MADGRAPH5_AMC@NLO directly according to the allowed decays and their couplings, 1% and 10%).

The limited timescale allowed to reach a consensus for the rec-
ommendations contained in this document has not allowed further
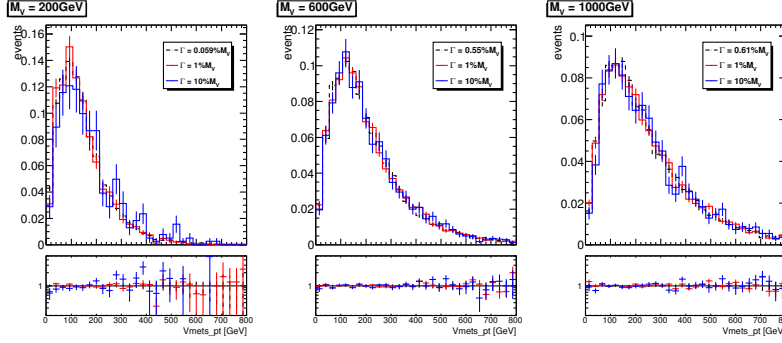
Figure B.3: Distribution of the V p_T for the $gu \to tV(\to t\bar{u})$ (on-shell V) for m_V = 200, 600, 1000 GeV (from left to right) and for three different visible decay width (computed from MadGraph5_aMC@NLO directly, 1% and 10%).

studies on the parameter scan of these models. The two Collaborations have however agreed to continue studying these models and agree on a common parameter scan, following the same path as for other models described in this document.

B.1.2 *Single Top Models*

Card files for MadGraph5_aMC@NLO are provided on the Forum SVN repository [For15e], corresponding to the Lagrangian from [AFM11]. Each coupling constant of this model can be set via the parameter card and the blocks which are relevant for the two models used for the experimental searches are described below. The relevant parameters in the MadGraph5_aMC@NLO parameter cards, also expressed in the notation introduced in the previous Section, are as follows for the two models considered.

To do **This section is being reworked by B. Fuks (??)**

1. Resonant scalar model described by the Lagrangian (B.1)

   - AQS and BQS: 3×3 matrices (flavour space) fixing the coupling of the scalar ϕ (S stands for scalar) and *down*-type quarks (Q stands for quarks), previously called a^q/b^q_{SR}.

   - A12S and B12S: 3×1 matrices (flavor space) fixing the coupling of the new fermion χ (where 12 stands for spin-1/2 fermion) and *up*-type quarks, previously called $a^{1/2}_{VR}$.

2. Non-resonant vectorial model described by the Lagrangian (B.3)

   - A1FC and B1FC: 3×3 matrices (flavor space) fixing the coupling of the vector V (1 stands for vector) and *up*-type quarks, previously called a^1_{FC}.

   - particle name: the dark matter candidate χ is not implemented

The width of the scalar resonance and of the new vector are set to all allowed decays in the ATLAS implementation, while the only allowed decay in the CMS implementation to the new fermion and a top quark for the resonant model.

To do **Continue discussion between ATLAS and CMS to reach an agreement, or include instructions to compare results. (??)**

B.2 *Further W+MET models with possible cross-section enhance-*
ments

As pointed out in Ref. [BCD⁺15], the mono-*W* signature can probe the iso-spin violating interactions of dark matter with quarks. The relevant operators after the electroweak symmetry breaking is

$$\frac{1}{\Lambda^2}\overline{\chi}\gamma_\mu\chi\left(\overline{u}_L\gamma^\mu u_L + \xi\overline{d}_L\gamma^\mu d_L\right).\tag{B.6}$$

Here, we only keep the left-handed quarks because the right-handed quarks do not radiate a *W*-gauge boson from the weak interaction. As the LHC constraints the cutoff to higher values, it is also important to know the corresponding operators before the electroweak symmetry. At the dimension-six level, the following operator

$$\frac{c_6}{\Lambda^2}\overline{\chi}\gamma_\mu\chi\,\overline{Q}_L\gamma^\mu Q_L\tag{B.7}$$

conserves iso-spin and provides us $\xi = 1$ [BCD⁺15]. At the dimension-eight level, new operators appear to induce iso-spin violation and can be

$$\frac{c_8^d}{\Lambda^4}\overline{\chi}\gamma_\mu\chi\,(H\overline{Q}_L)\gamma^\mu(Q_L H^\dagger) + \frac{c_8^u}{\Lambda^4}\overline{\chi}\gamma_\mu\chi\,(\tilde{H}\overline{Q}_L)\gamma^\mu(Q_L \tilde{H}^\dagger).\tag{B.8}$$

After inputing the vacuum expectation value of the Higgs field, we have

$$\xi = \frac{c_6 + c_8^d\, v_{\text{EW}}^2/2\Lambda^2}{c_6 + c_8^u\, v_{\text{EW}}^2/2\Lambda^2}.\tag{B.9}$$

For a nonzero c_6 and $v_{\text{EW}} \ll \Lambda$, the iso-spin violation effects are suppressed. On the other hand, the values of c_6, c_8^d and c_8^u depend on the UV-models.

There is one possible UV-model to obtain a zero value for c_6 and non-zero values for c_8^d and c_8^u. One can have the dark matter and the SM Higgs field charged under a new $U(1)'$. There is a small mass mixing between SM *Z*-boson and the new *Z'* with a mixing angle of $\mathcal{O}(v_{\text{EW}}^2/M_{Z'}^2)$. After integrating out *Z'*, one has different effective dark matter couplings to u_L and d_L fields, which are proportional to their couplings to the *Z* boson. For this model, we have $c_6 = 0$ and

$$\xi = \frac{-\frac{1}{2} + \frac{1}{3}\sin^2\theta_W}{\frac{1}{2} - \frac{2}{3}\sin^2\theta_W} \approx -2.7\tag{B.10}$$

and order of unity.

B.3 *Simplified model corresponding to dimension-5 EFT oper-*
ator

As an example of a simplified model corresponding to the dimension-5 EFT operator described in Section 3.2, we consider a Higgs portal with a scalar mediator. Models of this kind are among the most concise versions of simplified models that produce couplings of

Dark Matter to pairs of gauge-bosons. Scalar fields may couple directly to pairs of electroweak gauge bosons, but must carry part of the electroweak vacuum expectation value. One may thus consider a simple model where Dark Matter couples to a a scalar singlet mediator, which mixes with the fields in the Higgs sector.

$$L \subset m_s S^2 + \lambda S^2 H^2 + \lambda' S H^2 + y S \chi \overline{\chi} \qquad \text{(B.11)}$$

Where H is a field in the Higgs sector that contains part of the electroweak vacuum expectation value, S is a heavy scalar singlet and χ is a Dark Matter field. There is then an S channel diagram where DM pairs couple to the singlet field S, which then mixes with a Higgs-sector field, and couples to W and Z bosons. This diagram contains 2 insertions of EW symmetry breaking fields, corresponding in form to the effective dimension-5 operator in Section 3.2.1.

B.4   Inert 2HDM Model

For most of the simplified models included in this report, the mass of the mediator and couplings/width are non-trivial parameters of the model. In these scenarios, we remain agnostic about the theory behind the dark matter sector and try to parameterize it in simple terms.

We have not addressed how to extend the simplified models to realistic and viable models which are consistent with the symmetries of the Standard Model. Simplified models often violate gauge invariance which is a crucial principle for building a consistent BSM model which incorporates SM together with new physics. For example, with a new heavy gauge vector boson mediating DM interactions, one needs not just the dark matter and its mediator, but also a mechanism which provides mass to this mediator in a gauge invariant way.

Considering both the simplified model and other elements necessary for a consistent theory is a next logical step. The authors of [BCI$^+$] term these Minimal Consistent Dark Matter (MCDM) models. MCDM models are at the same time still toy models that can be easily incorporated into a bigger BSM model and explored via complementary constraints from collider and direct/indirect DM search experiments as well as relic density constraints. We discuss this model here both on its own merits and as an example of the flexibility of the simplified model approach.

The idea of an inert Two-Higgs Doublet Model (i2HDM) was introduced more than 30 years ago in [DM78, LHNOT07, DS09, GHS13**?**]. It is an extension of the SM with a second scalar doublet ϕ_2 with no direct coupling to fermions. This doublet has a discrete Z_2 symmetry, under which ϕ_2 is odd and all the other fields are even. The Lagrangian of the odd sector is,

$$\mathcal{L} = \frac{1}{2}(D_\mu \phi_2)^2 - V(\phi_1, \phi_2) \qquad \text{(B.12)}$$

with the potential V containing mass terms and $\phi_1 - \phi_2$ interactions:

$$
\begin{aligned}
V &= -m_1^2(\phi_1^\dagger\phi_1) - m_2^2(\phi_2^\dagger\phi_2) + \lambda_1(\phi_1^\dagger\phi_1)^2 + \lambda_2(\phi_2^\dagger\phi_2)^2 \\
&+ \lambda_3(\phi_2^\dagger\phi_2)(\phi_1^\dagger\phi_1) + \lambda_4(\phi_2^\dagger\phi_1)(\phi_1^\dagger\phi_2) + \frac{\lambda_5}{2}\left[(\phi_1^\dagger\phi_2)^2 + (\phi_2^\dagger\phi_1)^2\right] \quad \text{(B.13)}
\end{aligned}
$$

where ϕ_1 and ϕ_2 are SM and inert Higgs doublets respectively carrying the same hypercharge. These doublets can be parameterized as

$$
\phi_1 = \frac{1}{\sqrt{2}}\begin{pmatrix} 0 \\ v + H \end{pmatrix} \qquad \phi_2 = \frac{1}{\sqrt{2}}\begin{pmatrix} \sqrt{2}h^+ \\ h_1 + ih_2 \end{pmatrix} \qquad \text{(B.14)}
$$

In addition to the SM, i2HDM brings four more degrees of freedom coming from the inert doublet in the form of Z_2-odd charged scalar $h^\pm$ and two neutral Z_2-odd scalars h_1 and h_2. The lightest neutral scalar, h_1 is identified as the dark matter candidate. The i2HDM model has been explored at the phenomenological level from the perspective of collider DM searches [BPtV01, AHT08, ATYY14, BCI$^+$]. This model could produce $\not{E}_T$ +jet, Z, and Higgs as well as $\not{E}_T$ +VBF signatures at the LHC (see Figs. **??**).
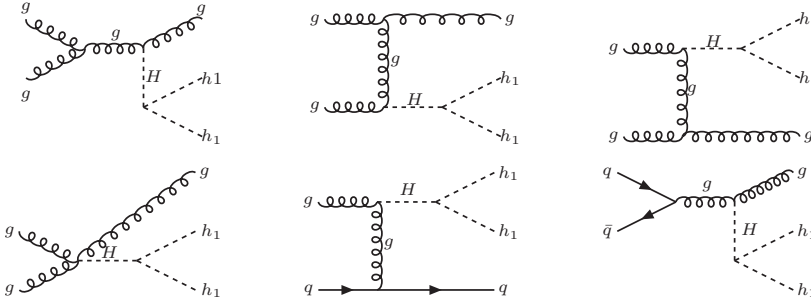
Figure B.4: Feynman diagrams for $gg \to h_1h_1 + g$ process contributing to mono-jet signature.
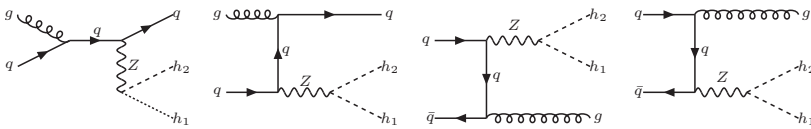
Figure B.5: Feynman diagrams for $q\bar{q} \to h_1h_2 + g$ ($gq \to h_1h_2 + q$) process contributing to mono-jet signature.
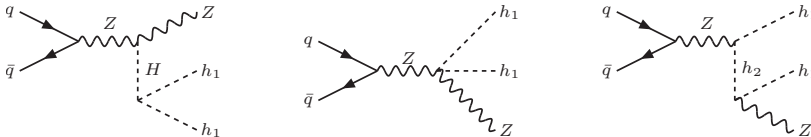
Figure B.6: Feynman diagrams for $q\bar{q} \to h_1h_1 + Z$ process contributing to mono-Z signature.

An experimental analysis of the parameter space has recently been performed in Ref. [BCI$^+$]. The authors of that study have implemented the model in CalcHEP and micrOMEGAs and propose a set of benchmark points (Table. B.1). Though the overall parameter space of i2HDM is 5-dimensional, the parameter space relevant to a specific LHC signature is only 1-2 dimensional. In the mono-jet
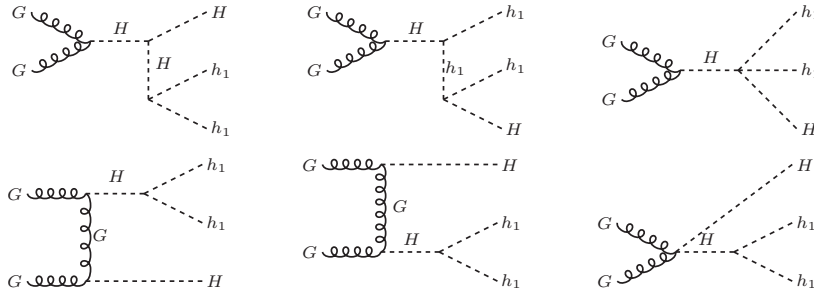
Figure B.7: Feynman diagrams for $gg \to h_1 h_1 + H$ process contributing to mono-Higgs signature.
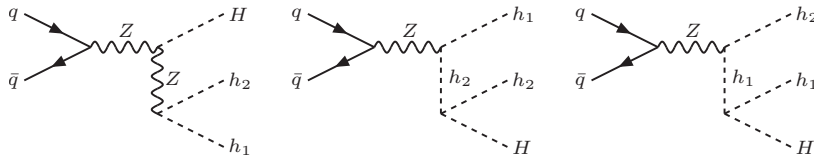
Figure B.8: Feynman diagrams for $q\bar{q} \to h_1 h_2 + H$ process contributing to mono-Higgs signature.

case, one can use two separate simplified models, a $gg \to h_1 h_1 + g$ process (via Higgs mediator) and a $q\bar{q} \to h_1 h_2 + g$ ($gq \to h_1 h_2 + q$) process (using Z-boson mediator) to capture the physics relevant to the search.
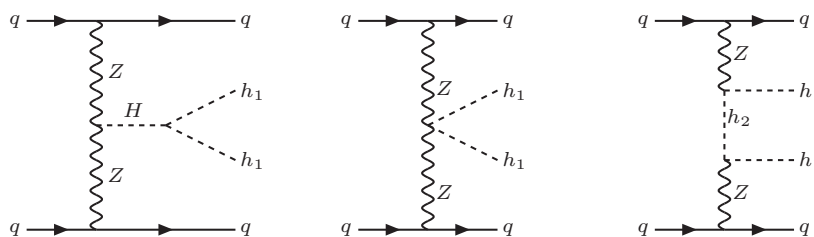
Figure B.9: Diagrams for $qq \to qqh_1h_1$ DM production in vector boson fusion process

BM	1	2	3	4	5
M_{h_1} (GeV)	45	53	66	82	120
M_{h_2} (GeV)	55	189	77	89	140
$M_{h_\pm}$ (GeV)	130	182	122	150	200
λ_2	0.8	1.0	1.1	0.9	1.0
λ_{345}	-0.010	-0.024	$+0.022$	-0.090	-0.100
Ω_h^2	1.1×10^{-1}	8.1×10^{-2}	9.9×10^{-2}	1.5×10^{-2}	2.1×10^{-3}
σ_{SI} (fb)	1.9×10^{-7}	7.9×10^{-7}	4.2×10^{-7}	4.5×10^{-7}	2.6×10^{-6}
σ_{LHC} (fb)	1.7×10^2	7.7×10^2	4.3×10^{-2}	1.2×10^{-1}	2.3×10^{-2}

Table B.1: Five benchmarks (BM) for i2HDM in $(M_{h_1}, M_{h_2}, M_{h_\pm}, \lambda_2, \lambda_{345})$ parameter space. We also present the corresponding relic density (Ω_{h^2}), the spin-independent cross section for DM scattering on the proton, and the LHC cross section at 13 TeV for mono-jet process $pp \to h_1, h_1 + jet$ for $p_T^{jet} > 100$ GeV cut.

C

Appendix: Presentation of experimental results for reinterpretation

We suggest the following to collider searches, when presenting results from the recommended benchmarks:

- Provide limits in collider language, on fundamental parameters of interaction: couplings and masses of particles in simplified model.

- Translate limits to non-collider language, for a range of assumptions in order to convey a rough idea of the range of possibilities. The details of this point are left for work beyond the scope of this Forum.

- Provide all necessary material for theorists to reinterpret simplified model results as building blocks for more complete models (e.g. signal cutflows, acceptances, etc). This point is detailed further in this appendix.

- As detailed in [KAM+12], model-independent results in terms of limits on cross-section times acceptance of new phenomena should be provided for all cases, but especially when EFTs are employed as benchmarks.

Along with the design of new searches to hunt for new physics at the LHC, it is important to consider information needed in order to reinterpret the searches outside of the collaborations. The following is a non-exhaustive list of recommendations in order to make reinterpretation easier and faster. This appendix details considerations for reimplementation of the analysis as well as for using the simplified model results directly given by the collaborations.
One of the important developments in recent years is an active development of the analyses recasting codes [DFK+15, CDFW14, KSTR15, CY11, KPSW]. The aim of these codes is to provide a public library of reimplemented and validated LHC analyses. Such libraries can then be used to analyze validity of a BSM scenario in a systematic and effective manner. The availability of public libraries further facilitates a unified framework and can lead to an organized and central structure to preserve LHC information in a long run.

In order to be able to develop such codes, it is important to get complete and systematic information from the collaborations.

- **Data digitization**: Availability of digitized data is one of the primary requirement. All information given by collaborations in the form of plots should be made available in a digitized format. Platforms such as HepData can be used in oder to maintain a centralized manner. In case when HepData can not be used, digitized data can be provided via analyses twiki pages. This information primarily includes expected and observed exclusion lines along with their $\pm 1\sigma$ uncertainty, expected and observed upper limits in case of simplified models, efficiency maps and all kinematic distributions as reported in the analysis. Units should be clearly specified. If the digitized figures are made available as a C macro or a ROOT file, the names of the objects should be clearly identifiable e.g. expected upper limits of a particular topology/model given as a ROOT file can be labeled as `KEY: TH2D ExpectedUpperLimit;1`. Furthermore, these digitized files can potentially contain more information (larger axes ranges) than displayed on the plot. This will help facilitate understand what happens beyond the limits displayed in the plot, e.g. a distribution for number of jets can be artificially limited to a point in the plot (for the purpose of clarity of figure) , however, this artificial limit leads to a sharp cutoff in the plot. While validating the analysis it is often necessary to compare the distributions beyond such artificial limits, having this information digitized will be of a great help in such cases.

C.1   Reimplementing analyses

This section lists information necessary in order to reimplement an analysis. Analysis reimplementation usually consists of several stages. Usually, one starts with reading the analysis note carefully, following which the preselection and event selection cuts are identified. These are then mimicked using a code typically written in C++. The detector simulation is carried out by using public detector simulation software e.g. Delphes [dF$^+$14]. The resulting ROOT file is then analyzed using the C++ code written in the previous step.

- **Analysis documentation**: The collaborations should provide a cutflow table with every analysis, such a cutflow table will naturally define the order of cuts implemented in an analysis. There are several preselection criteria which can not be easily simulated in phenomenology, e.g. MET cleaning. Numbers should be provided after such cuts so that theorists can rescale their number of events in order to account for such cuts. Efficiencies of several reconstructed objects are given as an input to detector simulation software like Delphes. It is thus very useful to get parametrized efficiencies for reconstructed objects (as a function of the rapidity η and/or transverse momentum p_T), along with the working

points at which they were evaluated (e.g. loose, tight selection). Object definitions should be clearly identifiable.

- **Validation**: Validation corresponds to re-deriving the results as given by collaborations in order to verify that the implementation of the analysis is correct. Usually most of the bug catching takes place in the phase of validation. The following items are necessary in order to recreate the results.

    - Monte Carlo generators: Monte Carlo generators along with the exact versions used to produce the event files should be listed.

    - Production cross sections: The order of production cross sections (e.g. LO,NLO,NLL) as well as the codes which were used to compute them should be provided. A table of reference cross sections for several values of particle masses such as ones provided by SUSY cross section working group will be highly appreciated.

    - Process Generation: Details of the generated process, detailing number of additional partons generated.

    - Availability of the LHE files: selected LHE files (detailing at least a few events if not the entire file) corresponding to the benchmarks listed in the analysis should be made available in order to cross check process generation. Experimental collaborations may generate events on-the-fly without saving the intermediate LHE file; we advocate that the cross-check of process generation is straight-forward if this information is present, so we encourage the generation of a few selected benchmark points allowing for a LHE file to be saved. For models concerning SUSY, corresponding SLHA files of benchmark files should also be details. Special attention should be paid to list the parameters which change the production cross section or kinematics of the process e.g. mixing angles.

    - Process cards: Process cards includes PDF choices, details of matching algorithms and scales and details of process generation. If process cards are not available, above items should be clearly identified.

    - model files: For models which are not already implemented in MadGraph5_aMC@NLO, availability of the corresponding model files in UFO format [DDF+12] is highly desired. It details the exact notation used in the model and hence sets up a complete framework. In case MadGraph5_aMC@NLO is not used, enough information should be provided in order to clearly identify the underlying model used for interpretations.

- **Limit setting**: Detailed description of the likelihood used in order to derive the limits should be given, this can contain statistical procedure within the analysis text itself, however direct availability of the limit setting code as a workspace in RooStats or HistFitter [BBC+15] is highly desirable.

- **Binned backgrounds**: For analyses using techniques such as sliding windows or an unbinned technique, the Standard Model backgrounds should be given in the form of bins. These backgrounds can then be interpolated.

- **Recast code**: Finally, the collaborations can provide an analysis code directly implemented in one of the public recasting codes detailed above. Such codes can be published via INSPIRE in order to track the versioning and citations.

C.2 *Simplified model interpretations*

The analyses almost always provide at least one simplified model interpretation along with the search results. These interpretations are simple and can be used in order to take a quick survey of viability of parameter space. Codes such as [KKL$^+$14b, KKL$^+$14a, PSWZ14] can make use of the simplified model results given in the form of 95% Confidence Level (CLs) upper limit or efficiency maps in order to test Beyond the Standard Model parameter space. It will thus be extremely useful if the results are given in a form as easily usable by the theory community.

- **Direct usability of the results**: The results given should be as useful as possible. For example, for a simplified model containing dark matter mass $m_{\rm DM}$, mediator mass $M_{\rm med}$ and couplings $g_{\rm DM}$, $g_{\rm q}$ it will be extremely useful to have 95% CLs upper limits on the product of couplings $\sqrt{g_{\rm DM}g_{\rm q}}$ or cross section times branching ratio as a function of $m_{\rm DM}$, $M_{\rm med}$. Limits on visible cross sections of the simplified models considered for interpretations should be made available.

- **Smooth grids**: The usage of simplified model results relies on interpolating between upper limit values. In order to facilitate the interpolation, regions where large variation of upper limits is observed should contain denser grid, if a uniform grid over the entire plane is not possible. For simplified model involving more than three parameters (two masses and product of couplings), slices of upper limits in the additional dimensions will be very useful e.g. for a simplified model involving one step cascade decay, upper limits can be provided for several values of intermediate mass in the plane of mother - daughter masses. Results with only one slice often render invalid to be used in a general model testing.

- **Availability of acceptance and efficiency maps**: Finally, acceptance and efficiency maps for all the signal regions involved in the analysis should be made available. These results are not only useful for model testing using simplified models but also to validate implementation of the analysis. Information about the most sensitive signal region as a function of masses is also very useful in order to determine the validity of approximate limit setting

2402   procedures being used by theorists (in the absence of any other

2403   sophisticated limit setting technique).

Bibliography

[A⁺08] J. Alwall et al. Comparative study of various algorithms for the merging of parton showers and matrix elements in hadronic collisions. *Eur.Phys.J.*, C53(2):473–500, 2008.

[A⁺12] Daniele Alves et al. Simplified Models for LHC New Physics Searches. *J.Phys.*, G39:105005, 2012.

[A⁺14a] Jalal Abdallah et al. Simplified Models for Dark Matter and Missing Energy Searches at the LHC. *arXiv:1409.2893*, 2014.

[A⁺14b] J. Alwall et al. The automated computation of tree-level and next-to-leading order differential cross sections, and their matching to parton shower simulations. *JHEP*, 07(2):079, 2014.

[A⁺15] Georges Aad et al. Search for new phenomena in final states with an energetic jet and large missing transverse momentum in pp collisions at $\sqrt{s} = 8$ TeV with the ATLAS detector. 2015.

[AAB⁺14] Jean-Laurent Agram, Jeremy Andrea, Michael Buttignol, Eric Conte, and Benjamin Fuks. Monotop phenomenology at the Large Hadron Collider. *Phys.Rev.*, D89(1):014028, 2014.

[Aad15] Search for new phenomena in events with a photon and missing transverse momentum in pp collisions at $\sqrt{s} = 8$ TeV with the ATLAS detector. *Phys.Rev.*, D91(1):012008, 2015.

[ABG14] Prateek Agrawal, Monika Blanke, and Katrin Gemmler. Flavored dark matter beyond Minimal Flavor Violation. *JHEP*, 1410:72, 2014.

[ABHL14] Prateek Agrawal, Brian Batell, Dan Hooper, and Tongyan Lin. Flavored Dark Matter and the Galactic Center Gamma-Ray Excess. *Phys.Rev.*, D90(6):063512, 2014.

[ADNP15] Chiara Arina, Eugenio Del Nobile, and Paolo Panci. Dark Matter with Pseudoscalar-Mediated Interactions

2439 Explains the DAMA Signal and the Galactic Center
2440 Excess. *Phys.Rev.Lett.*, 114:011301, 2015.

2441 [AFM11] J. Andrea, B. Fuks, and F. Maltoni. Monotops at the
2442 LHC. *Phys.Rev.*, D84:074025, 2011.

2443 [AHT08] Sarah Andreas, Thomas Hambye, and Michel H.G. Tyt-
2444 gat. WIMP dark matter, Higgs exchange and DAMA.
2445 *JCAP*, 0810:034, 2008.

2446 [AHW13] Haipeng An, Ran Huo, and Lian-Tao Wang. Searching
2447 for Low Mass Dark Portal at the LHC. *Phys.Dark Univ.*,
2448 2:50–57, 2013.

2449 [AJW12] Haipeng An, Xiangdong Ji, and Lian-Tao Wang. Light
2450 Dark Matter and Z' Dark Force at Colliders. *JHEP*,
2451 1207:182, 2012.

2452 [AST09] Johan Alwall, Philip Schuster, and Natalia Toro. Sim-
2453 plified Models for a First Characterization of New
2454 Physics at the LHC. *Phys.Rev.*, D79:075020, 2009.

2455 [ATL14] Sensitivity to WIMP Dark Matter in the Final States
2456 Containing Jets and Missing Transverse Momentum
2457 with the ATLAS Detector at 14 TeV LHC. Technical
2458 Report ATL-PHYS-PUB-2014-007, CERN, Geneva, Jun
2459 2014.

2460 [ATL15] Search for a single-top quark produced in association
2461 with missing energy in proton-proton collisions at
2462 $\sqrt{s} = 8$ TeV with the ATLAS detector. *Eur. Phys. J. C*,
2463 75:79, 2015.

2464 [ATYY14] Abdesslam Arhrib, Yue-Lin Sming Tsai, Qiang Yuan,
2465 and Tzu-Chiang Yuan. An Updated Analysis of In-
2466 ert Higgs Doublet Model in light of the Recent Re-
2467 sults from LUX, PLANCK, AMS-02 and LHC. *JCAP*,
2468 1406:030, 2014.

2469 [AWZ14a] Haipeng An, Lian-Tao Wang, and Hao Zhang. Dark
2470 matter with t-channel mediator: a simple step beyond
2471 contact interaction. *Phys. Rev. D*, 89:115014, 2014.

2472 [AWZ14b] Haipeng An, Lian-Tao Wang, and Hao Zhang. Dark
2473 matter with t-channel mediator: a simple step beyond
2474 contact interaction. *Phys.Rev.*, D89(11):115014, 2014.

2475 [BB13a] Yang Bai and Joshua Berger. Fermion Portal Dark
2476 Matter. *JHEP*, 1311:171, 2013.

2477 [BB13b] Yang Bai and Joshua Berger. Fermion Portal Dark
2478 Matter. *JHEP*, 11:171, 2013.

2479 [BB14] Yang Bai and Joshua Berger. Lepton Portal Dark
2480 Matter. *JHEP*, 1408:153, 2014.

[BBC+15]   M. Baak, G.J. Besjes, D. CÃŧte, A. Koutsman, J. Lorenz, et al. HistFitter software framework for statistical data analysis. *Eur.Phys.J.*, C75(4):153, 2015.

[BCD+15]   Nicole F. Bell, Yi Cai, James B. Dent, Rebecca K. Leane, and Thomas J. Weiler. Dark matter at the LHC: EFTs and gauge invariance. 2015.

[BCDF15]   Idir Boucheneb, Giacomo Cacciapaglia, Aldo Deandrea, and Benjamin Fuks. Revisiting monotop production at the LHC. *JHEP*, 1501:017, 2015.

[BCI+]   A. Belyaev, G. Cacciapaglia, I. Ivanov, F. Rojas, and M. Thomas. page to appear.

[BDG+12]   Nicole F. Bell, James B. Dent, Ahmad J. Galea, Thomas D. Jacques, Lawrence M. Krauss, et al. Searching for Dark Matter at the LHC with a Mono-Z. *Phys.Rev.*, D86:096011, 2012.

[BDM14]   O. Buchmueller, Matthew J. Dolan, and Christopher McCabe. Beyond Effective Field Theory for Dark Matter Searches at the LHC. *JHEP*, 1401:025, 2014.

[BDMM15]   Oliver Buchmueller, Matthew J. Dolan, Sarah A. Malik, and Christopher McCabe. Characterising dark matter searches at colliders and direct detection experiments: Vector mediators. *JHEP*, 1501:037, 2015.

[BDSG+14]   Giorgio Busoni, Andrea De Simone, Johanna Gramling, Enrico Morgante, and Antonio Riotto. On the Validity of the Effective Field Theory for Dark Matter Searches at the LHC, Part II: Complete Analysis for the s-channel. *JCAP*, 1406:060, 2014.

[BDSJ+14]   Giorgio Busoni, Andrea De Simone, Thomas Jacques, Enrico Morgante, and Antonio Riotto. On the Validity of the Effective Field Theory for Dark Matter Searches at the LHC Part III: Analysis for the t-channel. *JCAP*, 1409:022, 2014.

[BDSMR14]   Giorgio Busoni, Andrea De Simone, Enrico Morgante, and Antonio Riotto. On the Validity of the Effective Field Theory for Dark Matter Searches at the LHC. *Phys.Lett.*, B728:412–421, 2014.

[BFG15]   Matthew R. Buckley, David Feld, and Dorival Goncalves. Scalar Simplified Models for Dark Matter. *Phys.Rev.*, D91(1):015017, 2015.

[BFH10]   Yang Bai, Patrick J. Fox, and Roni Harnik. The Tevatron at the Frontier of Dark Matter Direct Detection. *JHEP*, 1012:048, 2010.

[BGG⁺01] A.J. Buras, P. Gambino, M. Gorbahn, S. Jager, and L. Silvestrini. Universal unitarity triangle and physics beyond the standard model. *Phys.Lett.*, B500:161–167, 2001.

[BLW14] Asher Berlin, Tongyan Lin, and Lian-Tao Wang. Mono-Higgs Detection of Dark Matter at the LHC. *JHEP*, 1406:078, 2014.

[BPtV01] C.P. Burgess, Maxim Pospelov, and Tonnis ter Veldhuis. The Minimal model of nonbaryonic dark matter: A Singlet scalar. *Nucl.Phys.*, B619:709–728, 2001.

[BT13] Yang Bai and Tim M.P. Tait. Searches with Mono-Leptons. *Phys.Lett.*, B723:384–387, 2013.

[C⁺14] Serguei Chatrchyan et al. Measurement of the production cross sections for a Z boson and one or more b jets in pp collisions at sqrt(s) = 7 TeV. *JHEP*, 1406:120, 2014.

[CDFW14] Eric Conte, BÃľranger Dumont, Benjamin Fuks, and Chris Wymant. Designing and recasting LHC analyses with MadAnalysis 5. *Eur.Phys.J.*, C74(10):3103, 2014.

[CDM⁺14] Linda Carpenter, Anthony DiFranzo, Michael Mulhearn, Chase Shimmin, Sean Tulin, et al. Mono-Higgs-boson: A new collider probe of dark matter. *Phys.Rev.*, D89(7):075017, 2014.

[CEHL14] Spencer Chang, Ralph Edezhath, Jeffrey Hutchinson, and Markus Luty. Effective WIMPs. *Phys. Rev. D*, 89:015011, 2014.

[CEMW04] John M. Campbell, R. Keith Ellis, F. Maltoni, and S. Willenbrock. Associated production of a Z Boson and a single heavy quark jet. *Phys.Rev.*, D69:074021, 2004.

[CEMW06] John M. Campbell, R. Keith Ellis, F. Maltoni, and S. Willenbrock. Production of a Z boson and two jets with one heavy-quark tag. *Phys.Rev.*, D73:054007, 2006.

[CG87] R. Sekhar Chivukula and Howard Georgi. Composite Technicolor Standard Model. *Phys.Lett.*, B188:99, 1987.

[CGT13] Nathaniel Craig, Jamison Galloway, and Scott Thomas. Searching for Signs of the Second Higgs Doublet. 2013.

[CHH15] Andreas Crivellin, Ulrich Haisch, and Anthony Hibbs. LHC constraints on gauge boson couplings to dark matter. 2015.

[CHLR13] R.C. Cotta, J.L. Hewett, M.P. Le, and T.G. Rizzo. Bounds on Dark Matter Interactions with Electroweak Gauge Bosons. *Phys.Rev.*, D88:116009, 2013.

[CMS14] Search for new physics with monotop final states in pp collisions at $\sqrt{s} = 8$ TeV. 2014.

[CNS$^+$13] Linda M. Carpenter, Andrew Nelson, Chase Shimmin, Tim M.P. Tait, and Daniel Whiteson. Collider searches for dark matter in events with a Z boson and missing energy. *Phys.Rev.*, D87(7):074005, 2013.

[Col15] CMS Collaboration. Search for H/A decaying into Z+A/H, with Z to ll and A/H to fermion pair. 2015.

[CY11] Kyle Cranmer and Itay Yavin. RECAST: Extending the Impact of Existing Analyses. *JHEP*, 1104:038, 2011.

[DDF$^+$12] Celine Degrande, Claude Duhr, Benjamin Fuks, David Grellscheid, Olivier Mattelaer, et al. UFO - The Universal FeynRules Output. *Comput.Phys.Commun.*, 183:1201–1214, 2012.

[dF$^+$14] J. de Favereau et al. DELPHES 3, A modular framework for fast simulation of a generic collider experiment. *JHEP*, 1402:057, 2014.

[DFH$^+$14] Tansu Daylan, Douglas P. Finkbeiner, Dan Hooper, Tim Linden, Stephen K. N. Portillo, et al. The Characterization of the Gamma-Ray Signal from the Central Milky Way: A Compelling Case for Annihilating Dark Matter. 2014.

[DFK$^+$15] B. Dumont, B. Fuks, S. Kraml, S. Bein, G. Chalons, et al. Toward a public analysis database for LHC new physics searches using MADANALYSIS 5. *Eur.Phys.J.*, C75(2):56, 2015.

[DFMQ13] Abdelhak Djouadi, Adam Falkowski, Yann Mambrini, and Jeremie Quevillon. Direct Detection of Higgs-Portal Dark Matter at the LHC. *Eur.Phys.J.*, C73(6):2455, 2013.

[DGIS02] G. D'Ambrosio, G.F. Giudice, G. Isidori, and A. Strumia. Minimal flavor violation: An Effective field theory approach. *Nucl.Phys.*, B645:155–187, 2002.

[DM78] Nilendra G. Deshpande and Ernest Ma. Pattern of Symmetry Breaking with Two Higgs Doublets. *Phys.Rev.*, D18:2574, 1978.

[DNRT13] Anthony DiFranzo, Keiko I. Nagao, Arvind Rajaraman, and Tim M. P. Tait. Simplified Models for Dark Matter Interacting With Quarks. *JHEP*, 1311, 2013.

[DS09] Ethan M. Dolle and Shufang Su. The Inert Dark Matter. *Phys.Rev.*, D80:055012, 2009.

[FHKT11] Patrick J. Fox, Roni Harnik, Joachim Kopp, and Yuhsin Tsai. LEP Shines Light on Dark Matter. *Phys.Rev.*, D84:014028, 2011.

[FHKT12] Patrick J. Fox, Roni Harnik, Joachim Kopp, and Yuhsin Tsai. Missing Energy Signatures of Dark Matter at the LHC. *Phys.Rev.*, D85:056011, 2012.

[For15a] SVN repository for Madgraph input cards for model with s-channel exchange of vector mediator, for electroweak boson final states. `https://svnweb.cern.ch/cern/wsvn/LHCDMF/trunk/models/EW_DMV/`, 2015. [Online; accessed 15-May-2015].

[For15b] SVN repository for Madgraph inputs for 2HDM model leading to a mono-Higgs signature. `https://svnweb.cern.ch/cern/wsvn/LHCDMF/trunk/models/EW_Higgs_2HDM/`, 2015. [Online; accessed 12-May-2015].

[For15c] SVN repository for Madgraph inputs for dimension-7 EFT models with direct DM-EW boson couplings. `https://svnweb.cern.ch/cern/wsvn/LHCDMF/trunk/models/EW_Fermion_D7/contributed_by_Renjie_Wang/`, 2015. [Online; accessed 24-April-2015].

[For15d] SVN repository for Madgraph inputs for model with s-channel exchange of pseudo-scalar mediator, produced in association with top quarks. `https://svnweb.cern.ch/cern/wsvn/LHCDMF/trunk/models/HF_S%2BPS/`, 2015. [Online; accessed 24-April-2015].

[For15e] SVN repository for Madgraph inputs for mono-top models. `https://svnweb.cern.ch/cern/wsvn/LHCDMF/trunk/models/HF_SingleTop/`, 2015. [Online; accessed 27-April-2015].

[For15f] SVN repository for Madgraph inputs for simplified model with a colored scalar mediator coupling to DM and b-quarks. `https://svnweb.cern.ch/cern/wsvn/LHCDMF/trunk/models/HF_S%2BPS/`, 2015. [Online; accessed 24-April-2015].

[For15g] SVN repository for Madgraph inputs for vector and scalar mediator models leading to a mono-Higgs signature. `https://svnweb.cern.ch/cern/wsvn/LHCDMF/trunk/models/EW_Higgs_all/`, 2015. [Online; accessed 24-April-2015].

[For15h] SVN repository for POWHEG input card for model with s-channel exchange of axial vector mediator. `https://svnweb.cern.ch/cern/wsvn/LHCDMF/trunk/models/Monojet_DMA/`, 2015. [Online; accessed 24-April-2015].

[For15i] SVN repository for POWHEG input card for model with s-channel exchange of pseudo-scalar mediator, production through top loop from gluon-gluon initial state. `https://svnweb.cern.ch/cern/wsvn/LHCDMF/trunk/models/Monojet_DMGG/`, 2015. [Online; accessed 24-April-2015].

[For15j] SVN repository for POWHEG input card for model with s-channel exchange of scalar mediator. `https://svnweb.cern.ch/cern/wsvn/LHCDMF/trunk/models/Monojet_DMS/`, 2015. [Online; accessed 24-April-2015].

[For15k] SVN repository for POWHEG input card for model with s-channel exchange of scalar mediator, with gluon loop. `https://svnweb.cern.ch/cern/wsvn/LHCDMF/trunk/models/Monojet_DMGG/`, 2015. [Online; accessed 24-April-2015].

[FW13] Patrick J. Fox and Ciaran Williams. Next-to-Leading Order Predictions for Dark Matter Production at Hadron Colliders. *Phys.Rev.*, D87(5):054030, 2013.

[GHS13] A. Goudelis, B. Herrmann, and O. Stål. Dark matter in the Inert Doublet Model after the discovery of a Higgs-like boson at the LHC. *JHEP*, 1309:106, 2013.

[GIR$^+$10] Jessica Goodman, Masahiro Ibe, Arvind Rajaraman, William Shepherd, Tim M.P. Tait, et al. Constraints on Dark Matter from Colliders. *Phys.Rev.*, D82:116010, 2010.

[HHR14] Ulrich Haisch, Anthony Hibbs, and Emanuele Re. Determining the structure of dark-matter couplings at the LHC. *Phys.Rev.*, D89(3):034009, 2014.

[HKR13] Ulrich Haisch, Felix Kahlhoefer, and Emanuele Re. QCD effects in mono-jet searches for dark matter. *JHEP*, 1312:007, 2013.

[HKSW15] Philip Harris, Valentin V. Khoze, Michael Spannowsky, and Ciaran Williams. Constraining Dark Sectors at Colliders: Beyond the Effective Theory Approach. *Phys.Rev.*, D91(5):055009, 2015.

[HKU13] Ulrich Haisch, Felix Kahlhoefer, and James Unwin. The impact of heavy-quark loops on LHC dark matter searches. *JHEP*, 1307:125, 2013.

[HR90] L.J. Hall and Lisa Randall. Weak scale effective supersymmetry. *Phys.Rev.Lett.*, 65:2939–2942, 1990.

[HR15] Ulrich Haisch and Emanuele Re. Simplified dark matter top-quark interactions at the LHC. 2015.

[KAM+12] S. Kraml, B.C. Allanach, M. Mangano, H.B. Prosper, S. Sekmen, et al. Searches for New Physics: Les Houches Recommendations for the Presentation of LHC Results. *Eur.Phys.J.*, C72:1976, 2012.

[KKL+14a] Sabine Kraml, Suchita Kulkarni, Ursula Laa, Andre Lessa, Veronika Magerl, et al. SModelS v1.0: a short user guide. 2014.

[KKL+14b] Sabine Kraml, Suchita Kulkarni, Ursula Laa, Andre Lessa, Wolfgang Magerl, Doris Proschofsky, and Wolfgang Waltenberger. SModelS: a tool for interpreting simplified-model results from the LHC and its application to supersymmetry. *Eur.Phys.J.*, C74:2868, 2014.

[Kop11] Joachim Kopp. Collider Limits on Dark Matter. 2011.

[KPSW] I.-W. Kim, M. Papucci, K. Sakurai, and A. Weiler. ATOM: Automated Testing Of Models. *to appear*.

[KSTR15] Jong Soo Kim, Daniel Schmeier, Jamie Tattersall, and Krzysztof Rolbiecki. A framework to create customised LHC analyses within CheckMATE. 2015.

[LHNOT07] Laura Lopez Honorez, Emmanuel Nezri, Josep F. Oliver, and Michel H.G. Tytgat. The Inert Doublet Model: An Archetype for Dark Matter. *JCAP*, 0702:028, 2007.

[LKW13] Tongyan Lin, Edward W. Kolb, and Lian-Tao Wang. Probing dark matter couplings to top and bottom quarks at the LHC. *Phys.Rev.*, D88(6):063510, 2013.

[LPS14] Hyun Min Lee, Myeonghun Park, and Veronica Sanz. Gravity-mediated (or Composite) Dark Matter. *Eur.Phys.J.*, C74:2715, 2014.

[LSWY13] Jia Liu, Brian Shuve, Neal Weiner, and Itay Yavin. Looking for new charged states at the LHC: Signatures of Magnetic and Rayleigh Dark Matter. *JHEP*, 1307:144, 2013.

[MMA+14] Sarah Malik, Christopher McCabe, Henrique Araujo, A. Belyaev, Celine Boehm, et al. Interplay and Characterization of Dark Matter Searches at Colliders and in Direct Detection Experiments. 2014.

[MMW05] Fabio Maltoni, Thomas McElmurry, and Scott Willenbrock. Inclusive production of a Higgs or Z boson in association with heavy quarks. *Phys.Rev.*, D72:074024, 2005.

[NCC+14] Andy Nelson, Linda M. Carpenter, Randel Cotta, Adam Johnstone, and Daniel Whiteson. Confronting

2735   the Fermi Line with LHC data: an Effective Theory
2736   of Dark Matter Interaction with Photons. *Phys.Rev.*,
2737   D89(5):056011, 2014.

2738 [PS14] Alexey A. Petrov and William Shepherd. Searching
2739   for dark matter at LHC with Mono-Higgs production.
2740   *Phys.Lett.*, B730:178–183, 2014.

2741 [PSWZ14] Michele Papucci, Kazuki Sakurai, Andreas Weiler,
2742   and Lisa Zeune. Fastlim: a fast LHC limit calculator.
2743   *Eur.Phys.J.*, C74(11):3163, 2014.

2744 [PVZ14] Michele Papucci, Alessandro Vichi, and Kathryn M.
2745   Zurek. Monojet versus the rest of the world I: t-
2746   channel models. *JHEP*, 1411:024, 2014.

2747 [RWZ15] Davide Racco, Andrea Wulzer, and Fabio Zwirner.
2748   Robust collider limits on heavy-mediator Dark Matter.
2749   2015.

2750 [WY12] Neal Weiner and Itay Yavin. How Dark Are Majo-
2751   rana WIMPs? Signals from MiDM and Rayleigh Dark
2752   Matter. *Phys.Rev.*, D86:075021, 2012.

2753 [WY13] Neal Weiner and Itay Yavin. UV completions of mag-
2754   netic inelastic and Rayleigh dark matter for the Fermi
2755   Line(s). *Phys.Rev.*, D87(2):023523, 2013.

2756 [ZBW13] Ning Zhou, David Berge, and Daniel Whiteson. Mono-
2757   everything: combined limits on dark matter produc-
2758   tion at colliders from multiple final states. *Phys.Rev.*,
2759   D87(9):095013, 2013.